The Synthesis and Study of Inorganic Cu(I) Donor-Acceptor Dyads for Dye-sensitized Photocathodes

Linyi Wei

A Thesis in the Department of Chemistry & Biochemistry

Presented in Partial Fulfillment of the Requirements
For the Degree of Master of Science (Chemistry)
At Concordia University
Montreal, Quebec, Canada

August 2023

CONCORDIA UNIVERSITY
School of Graduate Studies

This is to certify that the thesis prepared

By: Linyi Wei

Entitled: The Synthesis and Study of Inorganic Cu(I) Donor-Acceptor Dyads for Dye-sensitized Photocathodes

and submitted in partial fulfillment of the requirements for the degree of

Master of Science (Chemistry)

complies with the regulations of the University and meets the accepted standards with respect to originality and quality.

Signed by the final Examining Committee:

_____ Chair

Dr. Cameron Skinner

_____ Examiner

Dr. Louis Cuccia

_____ Examiner

Dr. John Oh

_____ Supervisor

Dr. Marek B. Majewski

Approved by _____

Dr. Louis Cuccia, Graduate Program Director

August 25th, 2023 _____

Dr. Pascale Sicotte, Dean of Faculty

Abstract

The Synthesis and Study of Inorganic Cu(I) Donor-Acceptor Dyads for Dye-sensitized Photocathodes

Linyi Wei

The dye-sensitized solar cell was first proposed by Grätzel and O'Regan in 1991. The idea behind this architecture was to use a dye to absorb visible light and then inject electrons into a wide bandgap semiconductor electrode, generating an electric current. The key component of the dye-sensitized solar cell was the dye molecule, inspired by the reaction center from natural photosynthesis in plants, which absorbs light and converts it into chemical energy. In recent years, this architecture has been adapted for synthesis where rather than generating a current, light-induced charge separation is used to transfer redox equivalents to a substrate initiating a chemical transformation. Devices driving these processes are known as dye-sensitized photoelectrochemical cells.

Previously, our group has shown that a copper(I)-based donor-chromophore-acceptor molecular system immobilized on a zinc oxide photoanode together with a copper(II)-based water oxidation catalyst can act as a light-harvesting photocatalytic assembly to split water. To enable the complementary reaction to reduce the protons formed from water splitting, we have designed a photocathode comprised of a copper(I)-based chromophore-acceptor dyad complex to drive a well-studied cobaloxime hydrogen evolving electrocatalyst with visible light. The molecular structures, optical properties and electrochemistry properties of the synthesized materials were characterized using techniques such as nuclear magnetic resonance spectroscopy, UV-Visible spectroscopy and cyclic voltammetry. In this thesis, the dye molecule dyad was installed on fluorine doped-tin oxide glass with a nickel oxide film and will work in concert with the previously studied photoanode to give a tandem cell where hydrogen gas as a solar fuel is expected to be produced effectively.

Acknowledgments

When I finish this thesis, I am filled with gratitude and joy, and I would like to express my most affectionate and sincere acknowledgments to everyone.

First of all, I would like to thank my dearest family. It is your selfless love and support that make me never feel lonely in my studies and life since arriving in another country at the age of 18. You are my solid backing, giving me endless courage and confidence when I meet setbacks and difficulties. Thank you for your meticulous care for me. It is your encouragement that keeps me moving forward.

Next, I would like to thank my supervisor Dr. Marek Majewski from the bottom of my heart. You are the guide on my academic road, pointing out the direction for me and carefully teaching me so that I will not be lost in the ocean of academic research. I would like to thank my committee members Dr. Louis Cuccia and Dr. John Oh for the instructions and the questions those worth thinking about during the committee meetings. Also, thank to Dr. Ashlee Howarth for every unforgettable group meeting and party we had together, which made me feel research was not a boring stuff at all.

At the same time, I would like to thank all the colleagues and friends I have met in my study and research: Zujhar Singh's valuable instructions of the experiments for the whole two years; Joey Ricardo for teaching me to master the electrochemistry and nice suggestions for this thesis, Kwan Ming Tam for all the computational analysis and you brought me to another chemistry field which has so much fun. Joseph Daniel Chiong and Camilo Perdomo for providing GC instrument and their time to spend with the great hydrogen evolution experiment; Caroline Bergeron, Victoria Lapointe, Rehmat Brar, Ximena Canales, Samantha Prelaz, Amna Muhammad, Laure-Anne Kanary, Cristina Pomilio, Susanna Vu and Lavina Trifoi, you are such nice girls to make me

happy when I feel pressure, I am really appreciated the time we spent together; I did not forget you guys: Chris Copeman, Victor Quezada-Novoa, William Leal, Jacob Hui, Lars Miller, and Rafeal Donnarumma, every time we met and say hello, I feel refreshed for a either energetic or tired day. Through the cooperation with everyone, I have broadened my horizon and learned a lot of valuable knowledge and experience. Through the hard times and the laughter, we have endured together, you have been an integral part of my life.

A special thank to Yuanfeng Wang, you have been a constant source of strength, love, and understanding throughout this journey. Your presence in my life has made every day brighter, and I am grateful for the unwavering love and encouragement you have bestowed upon me. There is a long way to go, let us spend the rest of our lives together.

I am grateful for all the encounters in the six years in Concordia University. Finally, I would like to thank myself. The completion of the thesis is a process full of sweat and tears, but also a moment full of achievement, and I am glad I did. The road of life is long and full of hardships, but I will continue to explore and pursue my own ideals and goals.

Contribution of Authors

In all Chapters, Linyi Wei carried out all core experimental work. Mass spectrometry was carried out by Dr. Heng Jiang (Centre for Biological Applications of Mass Spectrometry). Gas chromatography analysis was carried out by Camilo Perdomo and Joseph Daniel Chiong. Computational analysis was carried out by Kwan Ming Tam from McGill University. Dr. Marek B. Majewski acted in a supervisory role across all Chapters.

Table of Contents

List of Tables

List of Figures

List of Symbols and Abbreviations

*	Excited State
A	Electron Transfer Acceptor
ATR	Attenuated Total Reflectance
BODIPY	*meso*-Pyridyl Boron Dipyrromethene
C	Chromophore
CA	Chronoamperometry
C-A	Chromophore-Acceptor
CB	Conduction Band
CE	Counter Electrode
conc.	Concentrated
COSY	Correlation Spectroscopy
$[Cu(I)(ACN)_4]PF_6$	Tetrakis(acetonitrile)copper(I) Hexafluorophosphate
CSS	Charge-Separated State
D	Electron Transfer Donor
D-C-A	Donor-Chromophore-Acceptor
DCM	Dichloromethane
DMF	Dimethylformamide
dmg	Dimethylglyoxime
dmp	2,9-Dimethyl-1,10-Phenathroline
DRIFTS	Diffuse Reflectance Infrared Fourier-Transform Spectroscopy
DS-PEC	Dye-sensitized Photoelectrochemical Cell
DSSC	Dye-sensitized Solar Cell

e^-	Electron
E_{00}	Zero-Zero Energy of the Triplet MLCT.
EDS	Energy-Dispersive X-ray Spectroscopy
E_{ox}	Oxidation Potential
E_{pa}	Potential at the Peak Anodic Current
E_{pc}	Potential at the Peak Cathodic Current
E_{red}	Reduction Potential
ES	Excited State
ESI-MS	Electrospray Ionization-Mass Spectrometry
EtOH	Ethanol
FTIR	Fourier-Transform Infrared
FTO	Fluorine-Doped Tin Oxide
ΔG^o	Gibbs Free Energy
ΔG_{ET}^o	Gibbs Free Energy Between Photoinduced Electron Transfer
GC	Gas Chromatography
GS	Ground State
^1H	Proton
H^+	Proton
HEC	Hydrogen Evolving Catalyst
HETPHEN	Heteroleptic Phenanthroline
HOMO	Highest Occupied Molecular Orbital
$h\nu$	Energy of Photon
IL	Intraligand

IR	Infrared
ISC	Intersystem Crossing
LUMO	Lowest Unoccupied Molecular Orbital
MeOH	Methanol
Mes	Mesityl Group
^{1}MLCT	Singlet Metal-to-Ligand Charge Transfer
^{3}MLCT	Triplet Metal-to-Ligand Charge Transfer
MLCT	Metal-to-Ligand Charge Transfer
n-[Bu_4N]PF_6	Tetrabutylammonium Hexafluorophosphate
NHE	Normal Hydrogen Electrode
NIR	Near-Infrared
NMR	Nuclear Magnetic Resonance
P/PS	Photosensitizer
PEM	Proton Exchange Membrane
PJT	Pseudo-Jahn-Teller
RE	Reference Electrode
Ref.	Reference
SED	Sacrificial Electron Donor
SEM	Scanning Electron Microscope
TA	Transient Absorption
TEA	Triethylamine
THF	Tetrahydrofuran
TLC	Thin-Layer Chromatography

VB	Valence Band
Vis	Visible
UV	Ultraviolet
WE	Working Electrode
WOC	Water Oxidation Catalyst

List of Charts

List of Equations

List of Schemes

Chapter 1 Introduction

1.1 Overview

In this day and age, the use of energy is everywhere in terms of basic necessities of life. Although we have found many alternative green energy sources such as wind energy and solar energy, fossil fuel consumption is still the major source of producing energy currently. In 2021, fossil fuels accounted for 66% of the total demand of energy, and this situation will continue until 2030.[1] Climate change considerations notwithstanding, it is also relevant to note that the amount of fossil fuels is finite. According to statistics from Our World in Data in 2020, the reserves of coal, oil, and gas on the earth will be emptied in 139, 54 and 49 years, respectively.[2] Not only due to the shortage of fossil fuel, the greenhouse gasses and harmful substances that come from burning fossil fuels also lead to irreversible damages to the environment. Under the circumstances, for the development of humankind, green alternative energy sources must be used as much as possible.

Solar energy is one of the most universally available green energy sources. Main routes of using solar energy include converting it into electricity, heat, or to use it to drive chemical reactions to produce "solar fuel."[3] The total estimated use of energy for human beings is 4.6×10^{20} J; this amount of energy can be supplied by the sun in only 1 hour.[3] Unlike other energy sources, solar energy is ubiquitous in most areas of the earth and can be accessed locally. Moreover, the development and use of solar energy causes no carbon emission and very little other pollution. With their high efficiency and environmentally friendly properties, researchers are making significant progress in developing artificial photosynthesis technologies, which could have a profound impact on our ability to produce renewable energy and reduce our dependence on fossil fuels.

The dye-sensitized solar cell (DSSC) was first proposed by Gratzel and O'Regan in 1991.[4] The idea behind this architecture was to use a molecular dye to absorb visible light and then inject electrons from the excited state of the dye into a wide bandgap semiconductor electrode, generating an electric current. This finding was built on earlier findings from Fujishima and Honda who demonstrated firstly that the electrical potential generated by a semiconductor material could be used to drive the electrolysis of water to produce hydrogen and oxygen in 1972.[27] This same light-induced charge separation has recently been used to transfer redox equivalents to a substrate mimicking a chemical transformation in dye-sensitized photoelectrochemical cell (DS-PEC) instead of generating the current in traditional DSSC. In this thesis, the focus is the study of several known and new dye molecules that are immobilized within a DS-PEC device with an emphasis on hydrogen production at the photocathode.

1.2 Artificial photosynthesis

The aim of artificial photosynthesis is to develop technologies such as DSSC and DS-PEC that can mimic the natural process of photosynthesis, converting sunlight, water, and feedstock chemicals (carbon dioxide in nature) into storable and usable forms of energy, such as hydrogen, oxygen, and carbon-based fuels. The ultimate goal is to create a sustainable, carbon-neutral energy system that can provide energy security while reducing greenhouse gas emissions and mitigating climate change.[6, 7]

The light reaction stage of natural photosynthesis process happens between Photosystems I and II in the chloroplast of the plant cells, where ultimately the electron donor nicotinamide adenine dinucleotide phosphate (NADPH) drives the reaction of reducing carbon dioxide (CO_2) into carbohydrates ($C_6H_{12}O_6$, Equation **1-1**).[7-9] This process is the inspiration for the principle of artificial photosynthesis. However, the desired product is not carbohydrates but high-energy

chemicals such as the products of photoinduced water splitting (Equation **1-2**) and CO_2 reduction (Equation **1-3**).[7, 8]

$$6H_2O + 6CO_2 + hv \rightarrow C_6H_{12}O_6 + 6O_2 \quad (\mathbf{1\text{-}1})$$

$$2H_2O + hv \rightarrow 2H_2 + O_2 \quad (\mathbf{1\text{-}2})$$

$$2H_2O + 2CO_2 + hv \rightarrow 2HCOOH + O_2 \quad (\mathbf{1\text{-}3})$$

1.2.1 Artificial photosynthesis in water splitting

The reaction in equation 1-2 illustrates the overall process of photochemical water splitting. This reaction can be divided into two separate reactions which can (photo)electrochemically happen in cathode and anode compartments (**Scheme 1-1**).[7]

Scheme 1-1. Photochemical Water Splitting Coupled to Hydrogen/Oxygen Fuel Cell

Photochemical (Overall): $2H_2O + hv \rightarrow 2H_2 + O_2$

Fuel Cell-Anode: $2H_2 \rightarrow 4H^+ + 4e^-$

Fuel Cell-Cathode: $O_2 + 4H^+ + 4e^- \rightarrow 2H_2O$

Overall: $2H_2+O_2 \rightarrow 2H_2O$: ΔG^o=-4.92 eV (-113 kcal/mol)

Natural photosynthesis is initiated by the light absorption of light-harvesting complexes (LHCs) built of discrete molecular chromophores. LHCs have a light-harvesting antenna structure and move from ground state (GS) to the excited state (ES) after the light absorption process to ultimately form a charge-separated state (CSS) at the P680 reaction center in Photosystem II.[7, 10] For example, in plant cells, chlorophyll plays the role of chromophore with the structure of a central magnesium surrounded by a porphyrin (**1** in **Chart 1-1**) different long carbon-hydrogen side chain which are shown in **Chart 1-1**.[5, 10, 11] Structure **2** in **Chart 1-1** represents chlorophyll a.

Chart 1-1. Ref [5]

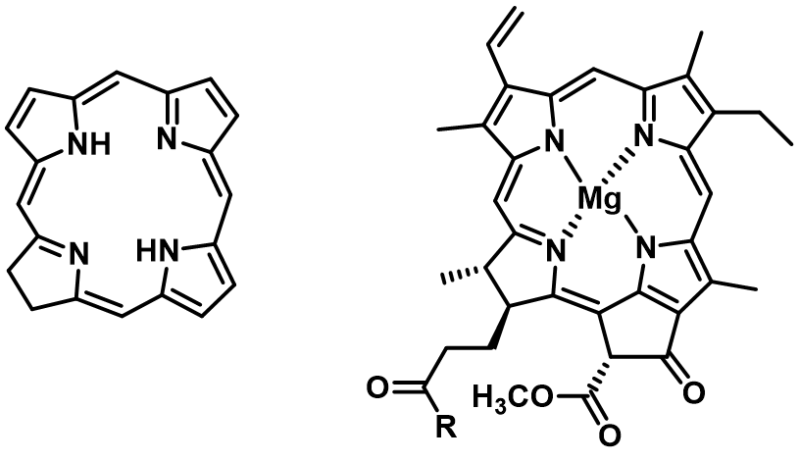

1 **2**

Inspired by this, Meyer *et al.* proposed an idea of a "modular" molecular approach to understand each subtle chemical reaction individually. As in the natural process, the different half-reactions are addressed individually and combined into one device finally. From these studies, an important contributing family of compounds are metal polypyridyl complexes that can undergo metal-to-ligand charge transfer (MLCT) transitions and can act as the central light absorbing chromophore. The "modules" are linked together into an assembly (known as a donor-chromophore-acceptor D-C-A) in **Figure 1-1** where all functional elements and processes required for water splitting are included.[7]

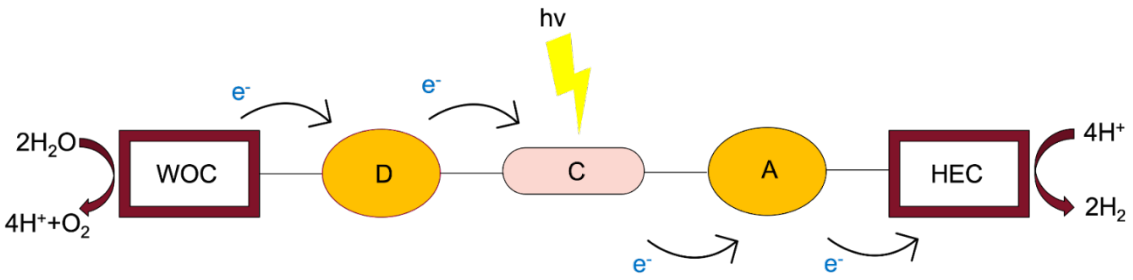

Figure 1-1. Schematic representation of reactions and electron transfer processes of water splitting into O_2 and H_2 via artificial photosynthesis in a donor-chromophore-acceptor (D-C-A) triad. The electron transfer direction forms a cycle (D → C → A → D) among each component. The abbreviations used in this figure (from left to right): WOC = water oxidation catalyst, D = electron donor, C = chromophore, A = electron acceptor, and HEC = hydrogen evolving catalyst. Adapted from reference [7].

A molecular donor-chromophore-acceptor (D-C-A) triad has three subunits: electron donor (D), chromophore (C), and electron acceptor (A). The reaction center C is excited by light absorption and enters the ES (C*). Then, the D-C-A triad may form the CSS via oxidative (D-C*-A → $D^{\bullet+}$-C-$A^{\bullet-}$) or reductive (D-C*-A → $D^{\bullet+}$-$C^{\bullet-}$-A) electron transfer quenching. After that, charge shift leads to the formation of $D^{\bullet+}$-C-$A^{\bullet-}$. The driving force must be favorable ($\Delta G^o < 0$), and this is influenced by judicious choice of accepting/donating fragments. Next, the charge shift among the triad activates the terminal catalysts. Hydrogen evolving catalyst (HEC) is activated by the electron from $A^{\bullet-}$, while the hole from $D^{\bullet+}$ can activate a water oxidation catalyst (WOC). Therefore, in order to initiate the catalytic reactions, the overall free-energy change ΔG^o cannot be higher than the free-energy change from GS to ES ($\Delta G^o \leq \Delta G_{ET}^o$).[7] Finally, the light absorption-electron transfer cycle repeats multiple times and gives the corresponding numbers of redox equivalents at

WOC and HEC. At the end of this cycle, O_2 and H_2 are generated to give the final energy conversion products in the hydrogen-oxygen fuel cell.

1. 3 Dye-sensitized photoelectrochemical cell (DS-PEC)

Dye-sensitized photoelectrochemical cells (DS-PEC) extend the field of dye-sensitized solar cells (DSSCs). DSSC is a type of photovoltaic developed by imitating the principle of photosynthesis and where a low-cost semiconductor (SC, typically titanium dioxide TiO_2) and photosensitizer act as the main materials, simulating photosynthesis but converting solar energy into electricity rather than storing it in chemical bonds.[13, 14] The architecture and working scheme of a DSSC device is represented in **Figure 1-2**. The blue arrows show the general electron flow among all the elements involved. The yellow arrows show the energy change between the dye molecule in the GS and ES. Recombination of injected electrons in the SC with either oxidized dyes or acceptors in the electrolyte is shown in the green arrows. The potentials for a DSSC were based on the N3 dye, TiO_2, and the I^-/I^3 redox couple in the figure.

Conversely in DS-PECs, the main function is to drive two half-reactions photoelectrochemically using a similar architecture as a DSSC, with a metal oxide SC and photosensitizer.[15] While water splitting is a common target for these devices, DS-PECs may also produce ammonia (NH_3) from the reaction of nitrogen and water or other value-added products from CO_2 reduction.[15, 16]

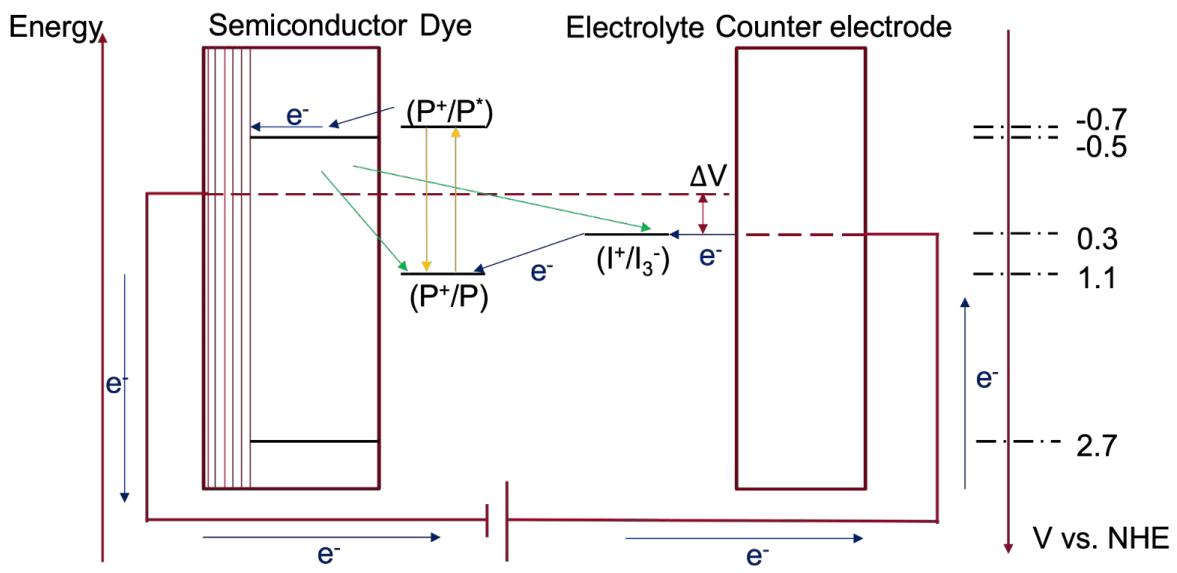

Figure 1-2. Schematic representation of the performance of a DSSC. The abbreviations used in this figure (from left to right): e^- = electron, P = photosensitizer, NHE = normal hydrogen electrode. Adapted from reference [23].

1.3.1 Architecture and working scheme of a DS-PEC

In a DS-PEC tandem cell, there are four major components divided between photocathode and photoanode compartments, respectively: a photosensitizer, a semiconductor layer, electrolyte solution with redox mediator, and the desired catalyst. Generally, the photoelectrodes (photocathode and photoanode) in DS-PECs are composed of a layer of dye-sensitized SC material on a transparent conducting oxide substrate like fluorine-doped tin oxide (FTO) glass. The details of the electron movement are explained in **Figure 1-3**.[17]

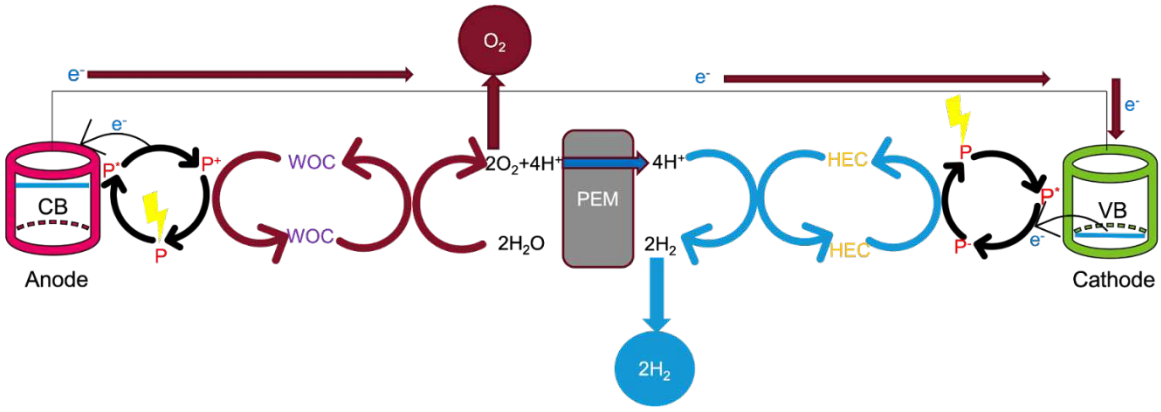

Figure 1-3. Schematic representation of the performance of a DS-PEC. The abbreviations used in this figure (from left to right): CB = conduction band, e^- = electron, P = photosensitizer, WOC = water oxidation catalyst, PEM = proton exchange membrane, HEC = hydrogen evolving catalyst, and VB = valence band. Adapted from reference [17].

In **Figure 1-3**, the overall photoinduced water splitting process can be divided into two compartments in the tandem DS-PEC system: photoanode compartment and photocathode compartment. The two compartments are connected through an external circuit. The initiation of the whole process starts by light absorption at the photosensitizer (P). In the anodic half-cell, the P molecule goes to the ES and will inject an electron into the conduction band (CB) of the SC. Subsequently, with the assistance of a WOC, one water molecule is split into one equivalent of O_2 and two protons (H^+). The O_2 is released from the DS-PEC. The protons go through a proton exchange membrane (PEM) from anode to cathode. Perfluorosulfonic acid (PFSA) is a suitable material that can be used as a PEM in the cell.[18] At the cathode, the P molecule absorbs light and goes to the ES. The valence band (VB) of the SC on the cathode receives an electron from the anode, and the electron then reductively quenches the P* molecule back to the ground state. HEC works to reduce two H^+ into H_2, generating hydrogen as a solar fuel.[17]

1.3.2 Photoelectrodes in a DS-PEC

In DS-PECs, the photoanode and photocathode are collectively known as photoelectrodes. Fluorine-doped tin oxide (FTO) on glass is transparent and is used as a substrate for fabricating the photoelectrodes. FTO allows the device to both absorb light and collect/inject the charges from/to the electrolyte within the device.[19] For the purposes of this thesis, there are three main types of photoelectrodes according to the connection of photosensitizer and catalyst: (1) the semiconductor (SC) film connects only to the photosensitizer and neither component has a direct chemical bond to the photocatalyst (i.e. the photocatalyst is free in the electrolyte); (2) photocatalyst and photosensitizer attach to the SC film independently and (3) photocatalyst and photosensitizer are bonded together as a single unit and this unit is attached to the SC film surface.[14]

To optimize charge movement in the cell, the SC materials on the photoelectrode are important to examine. At extremely low temperatures, the valence band (VB) of the SC is full. After thermal or light excitation, a portion of the population of the electrons in the VB will populate the conduction band (CB). The absence of an electron in the VB forms a positively charged vacancy, referred to as a hole. In this way, electricity can be thought of as charge carriers (electrons and holes) moving in opposite directions to an external circuit. They generate directional motion under the action of an external electric field and form a current.[20] **Figure 1-4** illustrates band theory used to describe the electronic structure of intrinsic SCs (those that are undoped and have no lattice defects).

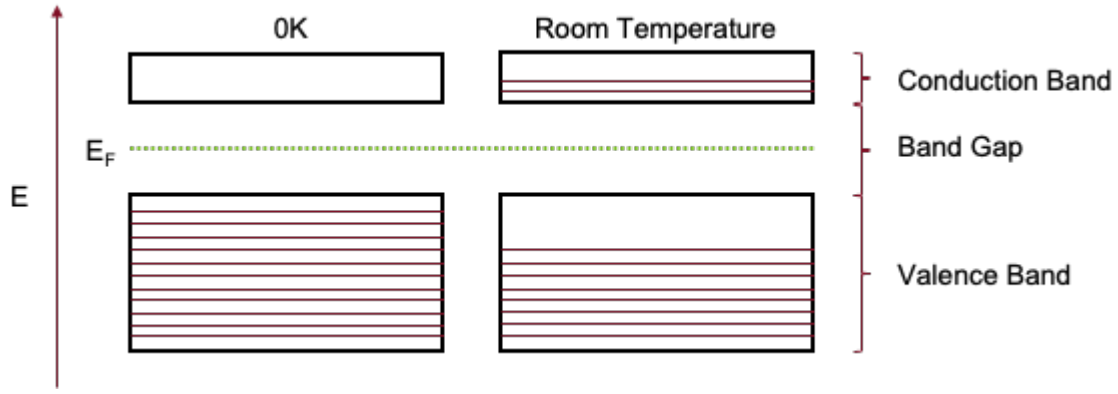

Figure 1-4. Intrinsic semiconductor bands representation at 0 K and room temperature. The red lines represent the potential energy levels of electrons in the bands. Abbreviations used here: E = energy and E_F = Fermi level. Adapted from reference [20].

However, it is hard to guarantee that all lattice structures are pure in SCs. This material may be modified by adding a small amount of other elements which have similar energy levels as the host becomes extrinsic. For example, monoatomic silicon (Si) is a kind of intrinsic SC, and nickel oxide (NiO) is an extrinsic SC. If the added element brings more electrons in the valence shell, the resulting SC is an n-type SC (n stands for negative, due to the addition of the electron). On the other hand, the added element on the host with fewer valence electrons leads to a p-type SC (p stands for positive, due to the loss of the electron).[20] In the photocathode case, it requires a p-type SC attached to the electrode since the cathode is receiving the electrons from the anode and needs a hole to receive. NiO and copper oxide CuO are two known examples of p-type SC that are used in a tandem DS-PEC for H_2 production.[21] In contrast, the material of SC applied on photoanode belongs to the n-type.

1.4 Molecular photosensitizers

In the context of DS-PEC systems, a molecular photosensitizer is a compound that can absorb light and then inject an electron into a band of the SC material from its excited state.[22] Broadly speaking there are three main families of photosensitizers: coordination compounds containing metal centers, synthetic organic dyes, and naturally occurring compounds. Arguably the most common structure for wide study is a coordination complex of a metal ion with a bidentate or tridentate ligand. The metal ion is typically a transition metal such as ruthenium, osmium, or cobalt, and the ligand is often a polypyridyl species like 2,2'-bipyridine, 2,2';6',2''-terpyridine, or 1,10-phenanthroline derivatives. The ligand is chosen based on its ability to strongly bind to the metal ion and to facilitate efficient electron transfer between the dye and the semiconductor material.[23, 24] For example, the widely used N-719 photosensitizer which has a central ruthenium ion coordinated to two bidentate 4,4'-dicarboxy-2,2'-bipyridine (dcbpy, where the carboxylates are used to bind to the SC surface) and contains tetrabutylammonium salts on the carboxylates and two thiocyanate (NCS^-) ligands. There are also some other examples of photosensitizers in **Chart 1-2** which are known.[24] Moreover, Hagfeldt *et al*. have outlined that there are some necessary properties for photosensitizers but five of them are crucial: (1) A photosensitizer should absorb light in part of near-infrared (NIR) and/or the whole visible region. (2) There should be an anchoring group on the photosensitizer molecule to attach itself to the SC surface. (3) The highest occupied molecular orbital (HOMO) level for the photosensitizer should be at an energy level that is more positive than the VB level of a p-type SC (in the case of photocathode design). (4) In the regeneration process the oxidized state level of the photosensitizer should be more positive than the redox potential of the electrolyte. (5) The photosensitizer molecule needs to be thermally, electrochemically, and photostable.[23]

In **Chart 1-2**, the geometries of the transition metal photosensitizers are octahedral (d^6) or tetrahedral (d^{10}) around the metal. The most common studied photosensitizers are ruthenium Ru complexes and complex **3** is the prototypical dye known as N3 (used extensively in early DSSC development owing to its broad absorbance across the visible spectrum).[24, 25] To-date, the highest photon-to-electrical efficiency for the ruthenium(II) complexes has reached around 12% in DSSC. [26] However, ruthenium is toxic for biological aspects, and this is a metal both rare and expensive. [43, 44] From the perspective of costs and sustainable development, researchers started to develop the use of metal-free organic dyes, such as D35 (complex **7**) and Mishara *et al.* have also listed a bunch of metal-free organic dyes for DSSC, which can be synthesized from abundant and inexpensive starting materials.[42, 25] On the other hand, other research has focused on the development of new metal-based photosensitizers, such as copper Cu(I)-based dyes, which offer similar optical spectra (both Ru(II) and Cu(I) photosensitizers have MLCT transitions centered around 400-500 nm) and energy levels to Ru(II)-based dyes but with improved stability and cost-effectiveness.[26, 29, 45] In the scope of this thesis, Cu(I)-based dyes will be synthesized and studied.

Chart 1-2. Ref. [24, 25]

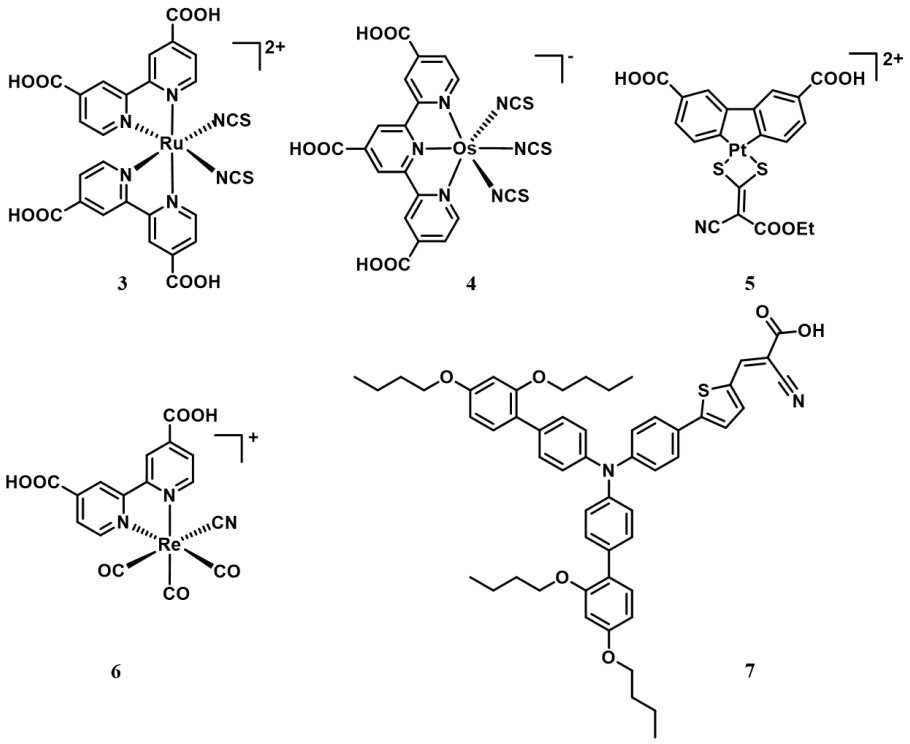

In **Figure 1-5**, a simple example of an energy level diagram of Cu(I)-based molecular photosensitizers. The geometry of Cu(I) complexes is tetrahedral which has a d^{10} electron configuration around Cu(I) center. However, pseudo-Jahn-Teller (PJT) distortions occur after the transformation of GS to ES of a molecule after light excitation, the electron configuration becomes d^9 in the lowest-lying ES.[46] After PJT, the intersystem crossing in between the ligands occurs and the molecule is resulted in the CSS. The whole process stores the energy in the CSS molecule even with some energy consumption in the conversion from ES to CSS.[46]

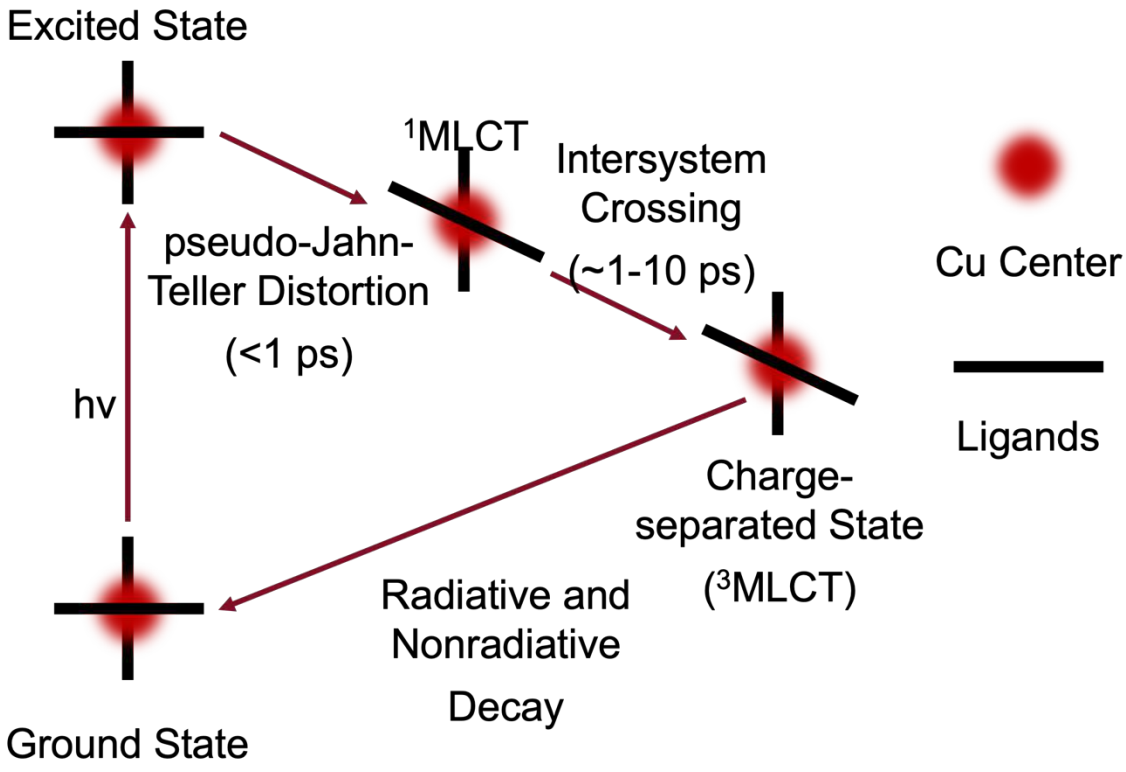

Figure 1-5. Energy level diagram for a Cu(I) based molecular photosensitizer from ground state to excited state including the PJT distortion and ISC decays.. Adapted from reference [46].

While Cu(I)-based molecular photosensitizers have similar properties as Ru(II)-based dyes, it is worth mentioning that Ru complexes tend to degrade over time in photocatalytic experiments due to the thermal population of metal centered d-d transitions. Based on the work of Nguyen *et al.,* the quantum efficiencies of degraded products from the Ru(II) complex were not high enough compared to the Ru(II) complex itself.[48] However, Cu(I) complexes tend to be more robust and resistant to degradation compared to Ru complexes. Based on the previous work of Khnayzer *et al.* generation of H_2 has remains constant for 20 hours for a Cu(I) complex and Co-based HEC.[49]

There are some interesting Cu(I)-based polypyridyl photosensitizer molecules in **Chart 1-2**. Complex **8** has the carboxylic acid on the ligands to anchor itself on SC as the photoelectrode.

Chart 1-3. Ref [24, 46, 47]

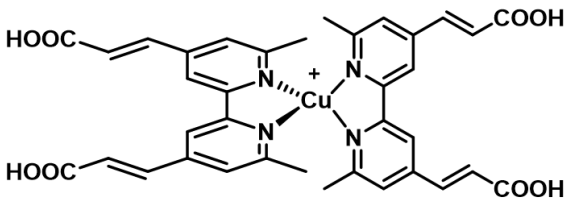

8

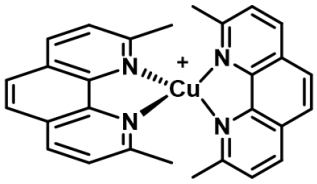

9

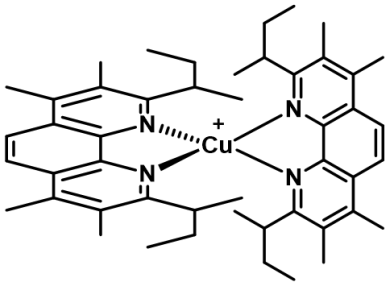

10

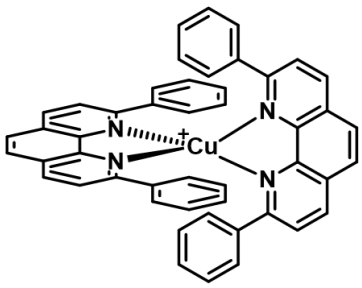

11

1.5 Solar fuels photocatalysis

1.5.1 Photocatalysis process and photocatalysts

Photocatalysis is a process in which a catalyst absorbs light and converts that energy to accelerate a chemical reaction. In photocatalysis, the catalyst is not consumed in the reaction, but rather acts as a mediator to facilitate the conversion of reactants into products. As mentioned earlier, Fujishima and Honda reported on the photocatalytic properties of titanium dioxide (TiO_2) and demonstrated that it could be used to split water into H_2 and O_2 under UV irradiation.[27] They proposed that the process involved the absorption of light by TiO_2, which created electron-hole pairs that could react with water molecules to process photoinduced water splitting.[27]

1.5.2 Mechanism and species of hydrogen evolution

A schematic representation of the proton reduction reaction on the photocathode compartment of a DS-PEC is shown on **Figure 1-4** with a starting catalyst M^{n+}. There are three different ways

for reducing the intermediate molecule H-M^{n+} after the protonation of the starting M^{n+}. The first way just shows a simple heterolytic reaction by regenerating the M^{n+} (heterolytic). In the second pathway, the $M^{(n-1)}$ forms by the reaction of two H-M^{n+} molecules (homolytic). The H_2 is released and the second hydride molecule ($M^{(n-1)+}$) forms at the same time. In the last processing ways, the $M^{(n-1)+}$ is generated again by the reduction of an e^- and furtherly process either heterolytic or homolytic reaction.[17]

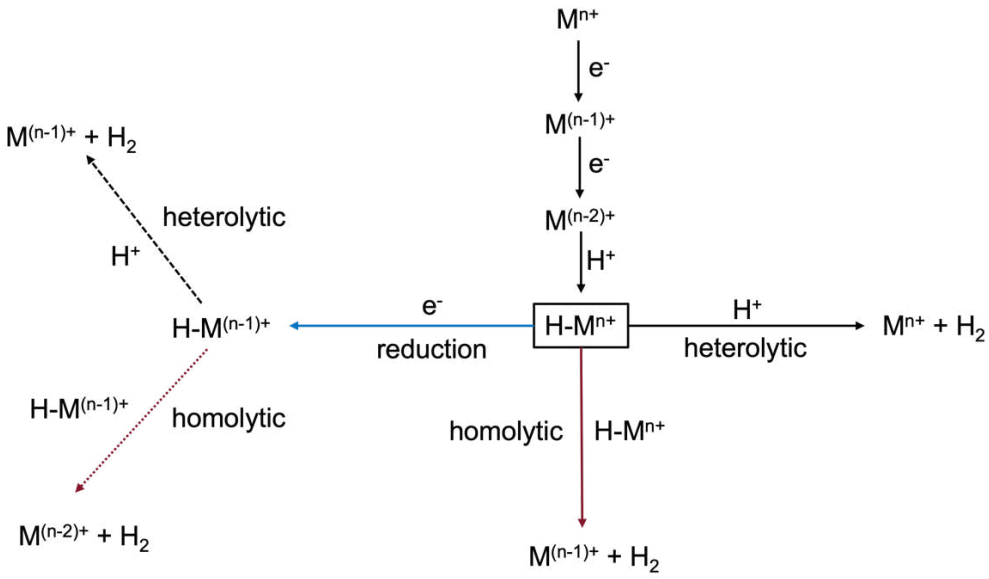

Figure 1-6. General catalytic scheme with a HEC at a metallic center M^{n+} for proton reduction. Adapted from reference [17].

Recently, the HEC with both rare and abundant metallic centers such as Pt, Co, and Ni have been widely studied. In rare metal-based HECs, the proton reaction efficiency may reach up to 34% in Rh complexes one example is shown as complex **10** which was coupled with the photosensitizer **11** in **Chart 1-3**.[17] To solve the problem with the lack of rare metals, HECs with transition metals such as Fe, Co, Ni and Mo have been investigated in the past 20 years, and **Chart 1-3** provides the

structures and efficiencies of a selection HECs containing the metal centers mentioned above (complex **12**-**15**) and the photosensitizers (PSs) those were working with (complex **16**-**18**). Table 1-1 lists the corresponding PSs with the HECs and their turnover numbers (TONs).[17, 28] TONs are referred to as moles of H_2 per mole of catalyst, unless otherwise indicated. Photosensitizers and sacrificial electron donors (SED) are added for comparison.

Chart 1-4. Ref[17, 28]

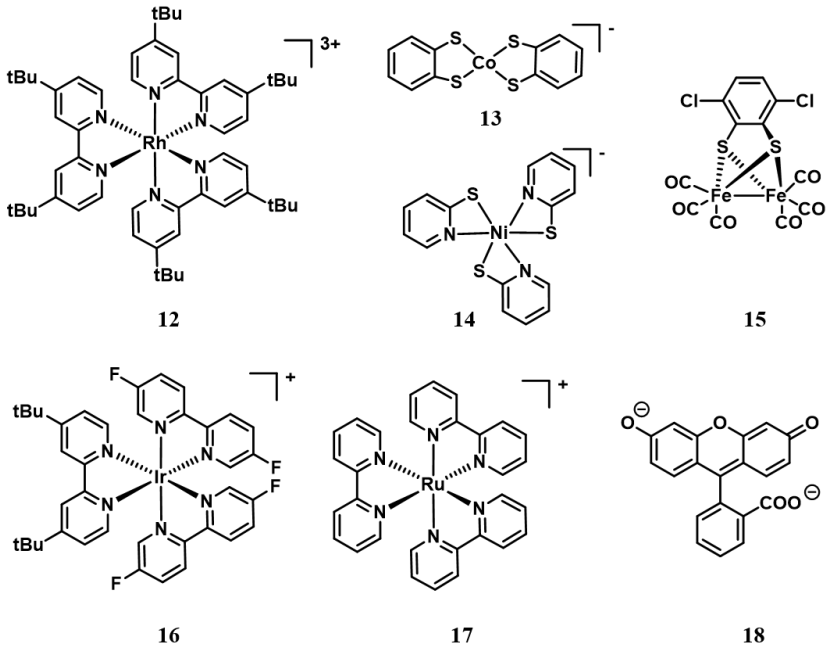

Table 1-1. Catalyst and photosensitizer pairings for proton reduction[17, 28]

Catalyst	PS	SED	TON
12	**16**	TEA	5000
13	**17**	Ascorbic acid	2700
14	**18**	TEA	5500
15	**17**	Ascorbic acid	200

1.5.3 Photocatalytic systems incorporating cobaloximes

Cobaloximes are a family of cobalt-based compounds that are commonly used as catalysts in photocatalysis reactions. The basic structure of a cobaloxime consists of a cobalt ion coordinated with two bidentate oxime ligands. In general, cobaloxime catalysis involves the transfer of electrons between the cobalt ion and the substrate or a reactant, which is facilitated by the coordination of the ligands. [28] In the previous section, photocatalytic ensembles were assembled from separated PSs and HECs. More recently, studies from Bartelmess *et al.*, created covalently and coordinatively linked molecular assemblies by sensitizing cobaloximes by different meso-pyridyl boron dipyrromethene (BODIPY) chromophores with either Br or I on R_2 position as the substituents on the BODIPYs themselves. [36]

Scheme 1-2. BODIPY and the synthesis of BODIPY-cobaloxime [36]

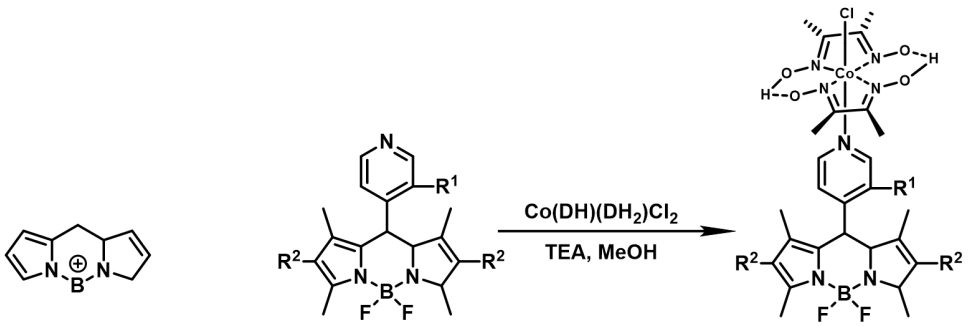

19 20 21

Complex **19** in **Scheme 1-2** represents the mentioned BODIPY molecule and each of the carbon site of it can be connected with substituents. Complex **20** is the PS precursor of BODIPY-cobaloxime with one organic ligand (H or Me) on R^1 position and one halogen atom (Br or I) on R^2 position. After anchoring the cobaloxime with **20**, the complex contains both PS and cobaloxime will drive the photocatalysis reaction for reducing the protons. When R^1 = Me and R^2

= I, this complex system performs best with TON of 30.9. After 17 hours, this complex produced 60 μmmol of H_2 under the irradiation 525±10 nm LED operating at 10 mW, which shows the chromophore is important in this BODIPY-cobaloxime system.[36]

1.6 Electrochemistry

Electrochemistry provides fundamental insights and tools for optimizing the performance, efficiency, and stability of dye photosensitizers in DSSCs and DS-PECs. It allows us to understand the electrochemical processes involved in energy conversion, leading to advancements in the field of photovoltaics and renewable energy. In the context of this work, we are observing the chemical change of oxidation or reduction of a metal complex, and the redox behaviors of the ligands surrounding the metal centre.[40] In this thesis, cyclic voltammetry (CV) and chronoamperometry (CA) methods were used to probe the electrochemical properties of the molecular photosensitizers and corresponding photoelectrodes.

Cyclic voltammetry (CV) is an electrochemical technique used to study the redox behavior of a chemical species or system by measuring its electrical response to different applied potentials. The potential applied to the working electrode repeats a linear scan at a specific scanning rate between two predetermined limits which are called the upper and lower potential limits. In CV, three electrodes are typically used (**Figure 1-7**): the working electrode, the reference electrode, and the counter electrode. Each electrode serves a specific role in the electrochemical cell and contributes to the measurement of the current response during the CV experiments. The working electrode (WE) is usually a conductive material, here was the 2 mm Pt button. The reference electrode (RE) provides a stable and known potential against which the potential of the working electrode is measured, and an Ag wire coated with a layer of AgCl was used in this project. For the further

calculation, the potential of Ag/AgCl electrode E(Ag/AgCl) can be converted into the potential of the normal hydrogen electrode (NHE) with the Equation **1-4**.[51]

$$E(NHE) = E(Ag/AgCl) + E^0(Ag/AgCl) + 0.059\ pH,\ E^0(Ag/AgCl) = 0.197V \qquad (\mathbf{1\text{-}4})$$

The Pt wire counter electrode (CE) completes the circuit and balances the current flowing through the working electrode. It ensures that the current passing through the working electrode is not limited by the availability of electrons.[40] All the three electrodes are immersed in an electrolyte solution containing the substance of interest with an electrolyte.

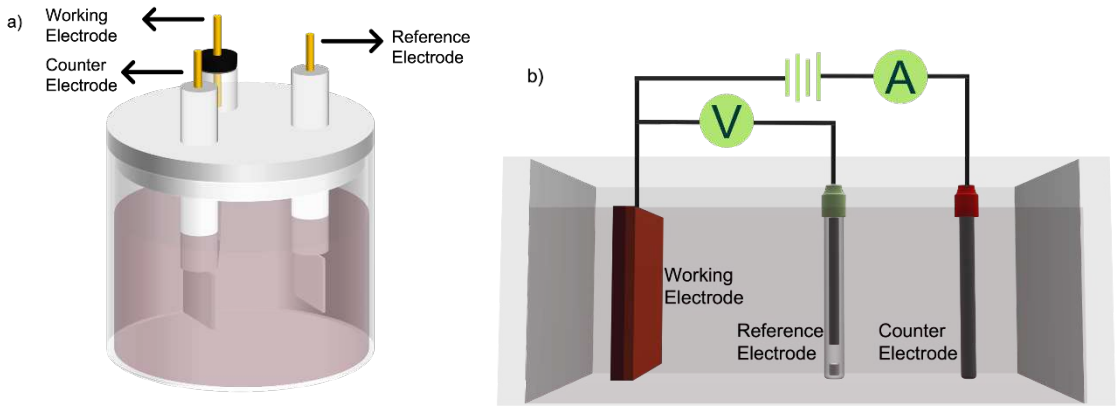

Figure 1-7. Schematic representation of a) an electrochemical cell with three electrodes for the CV experiments (adapted from reference [40]), and b) its internal illustration.

1.7 Gas chromatography

Gas chromatography (GC) is an analytical technique used to separate and analyze volatile compounds in a mixture. It is based on the principle of partitioning between a stationary phase and a mobile phase. To detect gas evolution from photocatalytic measurements reported in this these GC experiments were carried out. In a typical experiment, an aliquot of the reaction vessel headspace is T injected into the GC instrument and is carried with a carrier gas such as nitrogen

through a column packed with the stationary phase. An oven is used to keep the column at constant temperature. The detector is the component that detects and quantifies the separated compounds as they elute from the column.[41] For this work, both flame ionization (FID) and thermal conductivity (TCD) detectors were used. With the elution time, the peaks in the chromatography display the gas components of the mixture. The gas for calibration was injected and detected first and then the peaks on the chromatography were compared to the experimental chromatography.

1.8 Goals and Scope

The major purpose of this thesis is to design and synthesize a molecular photosensitizer C-A (chromophore-acceptor) dyad working on a nickel oxide (NiO) film surface and a HEC in order to produce H_2 as desired solar fuel from protons. It is expected that this dyad will act as an effective photosensitizer for driving a proton reduction catalyst both homogenously and heterogeneously as a photocathode. This work is subdivided into the following four objectives:

1. Synthesize ligands for a molecular photosensitizer individually. Then, selectively use the heteroleptic phenanthroline (HETPHEN) approach with tetrakis(acetonitrile)copper(I) hexafluorophosphate $[Cu(I)(ACN)_4]PF_6$ to form a small library of integrated heteroleptic molecular photosensitizers.
2. Fabricate the target photoelectrode architecture by first depositing NiO on FTO as a substrate. Then, link photosensitizer molecules from *Objective 1* on the NiO surface through an anchoring group.
3. Use established procedures to synthesize a molecular cobaloxime hydrogen evolving catalyst (HEC) for proton reduction experiments.
4. Measure hydrogen evolution by gas chromatography.

Chapter 2 describes the experimental methods for the synthesis and characterization of all of the molecules and materials evaluated in this work. Chapter 3 quantifies the results of the work and includes a discussion on the significance of the findings. Chapter 4 is a concluding chapter that outlines the next steps of this work.

Chapter 2 Experimental Details

2.1 Materials and methods

2.1.1 Materials

All chemicals were used as received from commercial sources. 2,9-dimethyl-1,10-phenanthroline and tetrakis(triphenylphosphine)palladium(0) (99%) were purchased from Thermo Scientific. H_2SO_4 (98%), activated 10% Pd/C, $K_2Cr_2O_7$, $POCl_3$, LiOH, bathocuproinedisulfonic acid, $NiCl_2$, poly(ethylene glycol)-block-poly(propylene glycol)-block-poly(ethylene glycol) (PEG-PPG-PEG), and DMSO-d_6 were purchased from Sigma-Aldrich. Hydrazine monohydrate, 1,8-naphthalic anhydride, tetrakis(acetonitrile)copper(I) hexafluorophosphate, dimethylglyoxime (98%), and TEA were purchased from TCI. Glacial acetic acid, DCM, H_2O_2 (30%), THF, K_2CO_3, toluene, HCl, cobalt(II) $CoCl_2$, and DMF were purchased from Fisher. 4,4'-dimethyl-2,2'-bipyridine, 2,4,6-trimethylphenylboronic acid, and n-butylammonium hexafluorophosphate were purchased from Acros Organics.

2.1.2 General methods

2.1.2.1 Structural characterization

All moisture sensitive reactions were carried out under nitrogen atmosphere with standard Schlenk techniques. The structures of synthesized molecules were confirmed by ^{1}H NMR, ^{13}C NMR and 2D NMR using 300 MHz Bruker and 500 MHz Varian spectrometers. Chemical shifts are referenced to the residual solvent peaks. The NMR characterization results were analyzed via MNova software. The solution for ^{1}H NMR was prepared with 3 mg of each sample and 0.5 mL of deuterated solvent. The deuterated solvents were used as $CDCl_3$ or DMSO-d_6 depending on the solubilities of the samples. The ^{1}H NMR spectra were recorded using a 300 MHz Varian spectrometer including 16 scans. The solution for ^{13}C and 2D NMR was using more than 5 mg of

the sample in 0.5 mL of deuterated solvent, and the spectra were recorded using a 500 MHz Varian spectrometer running overnight. The residual $CDCl_3$ singlet at 7.26 ppm and DMSO-d_6 singlet at 2.50 ppm were selected as the reference standards.

Vibrational spectroscopy for structural characterization was carried out by Attenuated total reflectance Fourier-transform infrared- (ATR-FTIR) spectroscopy using a Thermo Scientific Nicolet iS5 equipped with an iD5 ATR accessory. The Omic 9 software was used to process the raw data for ATR-FTIR. Diffuse reflectance infrared Fourier-transform spectroscopy (DRIFTS) spectrum was collected using Thermo Scientific Nicolet 6700 FT-IR equipped with a MCT detector. For the powder-like samples, they were analyzed by an attenuated total reflectance (ATR) instrument with a resolution of 0.4 cm^{-1}, a gain of 1, and an optical velocity of 0.4747 cm/s. About 0.1-0.2 g of each sample was placed on the crystal in a room environment and measured under 64 scans in the spectral range of 500-4500 cm^{-1}. To check the bond connections on the photoelectrode, DRIFTS with a resolution of 1 cm^{-1} was used and the samples were analyzed under N_2 atmosphere.

Chemical formulas of the synthesized molecules were confirmed with electrospray ionization-mass spectrometry (ESI-MS) using a Waters Model QTOF Ultima instrument.

The morphology of the films on fluorine-doped tin oxide (FTO) glass was examined by a Phenom ProX desktop scanning electron microscope (SEM) with an accelerating voltage of 10kV. A Rigaku XRD model was used to collect Powder X-ray diffraction (PXRD) patterns of the samples in the range of $3° < 2\Theta < 40°$ in 0.02° step with a 0.200 s scanning speed.

2.1.2.2 Ground state characterization

In the scope of the studies, UV-Visible absorption spectra were obtained from 200-800 nm for the study of photoluminescence characterizations. UV-Vis absorption spectroscopy was carried out with a Cary 6000 Series UV-Vis-NIR spectrophotometer (Agilent Technologies) and a 1 cm pathlength quartz cuvette. The wavelength changeover was at 350 nm and a 5.0 nm bandwidth was set with a scan speed of 10nm/s and the resolution was 1 nm on the instrument. The solutions for measuring were premade as 0.1 mM and were injected into the cuvette with a pipette.

2.1.2.3 Electrochemistry

Electrochemical measurements including cyclic voltammetry on the photosensitizers and chronoamperometry (CA) on **NiO|C-A1** were performed using a WaveDriver 20 Integrated Bipotentiostat/Galvanostat workstation (Pine Research Instrumentation, Inc.), and the raw data were interpreted with AfterMath software. All the experiments were carried out under argon atmosphere. The detailed electrochemical experiments procedures are explained in the following sections.

2.1.2.3.1 Cyclic voltammetry

The three electrode-system including a 2 mm Pt button as WE, Ag/AgCl wire as RE and Pt wire as CE were immersed in an electrolyte solution containing the substance of Cu(I) complexes with an electrolyte. Herein, the solution composition contains the Cu(I) complexes, the electrolyte tetrabutylammonium hexafluorophosphate (n-$[Bu_4N]PF_6$) were prepared in DCM with the concentration of 0.1 mM and 1 mL, respectively. The CV measurements were carried out in the prepared solution with the electrodes under an Ar atmosphere at the scan rate of 0.1 V/s and the potential range between -2.0 V and 1.5 V.

2.1.2.3.2 Chronoamperometry

Chopped-light chronoamperometry (CA) is an electrochemical technique used to study the behavior of an electroactive species over time by measuring the current response at a constant applied potential. The experimental set up of CA was similar to CV which was the three-electrode system. The working electrode was used as the fabricated photoelectrode **NiO|CA1**, Ag/AgCl wire was used as the reference electrode and Pt wire was as the counter electrode. All the electrodes were immersed in a 1 mM n-$[Bu_4N]PF_6$ in dimethylformamide (DMF) as the electrolyte solution. The working electrode was illuminated with the white light (a four Cree XP-G3 warm white LED array) under Ar atmosphere. The time duration was 180 s involving 20 s of light on and 20 s of light off. The photocurrent was observed with the light shining on the photoelectrode. In the analysis of the CA result, we can observe there is no photocurrent when the photoelectrode was placed in the dark environment and a negative photocurrent formed after receiving the light source. The amplitude stands for the maximum photocurrent for the photoelectrode generated.

2.1.2.4 Hydrogen evolution

The measurement of hydrogen evolution from the catalytic photoinduced water splitting was measured by a PerkinElmer Model Arnel 4003-P gas chromatography (GC) instrument. The column for purifying were (R4, R10) NR021591 HAYESEP N for separating the polar/nonpolar species and (R5, R11) NR022501 MOLE SIEVE 13 X for identifying the gas species. The formed gas was injected to the machine and the compositions were detected with FID and TCD, then the data were analyzed through TotalChrom Navigator software. In the scope of the study, only the gas species (H_2) generated from the dye photosensitizers themselves was detected. In a typical photocatalysis experiment, 2 mL of 10% v/v of triethylamine (TEA) in dimethylformamide (DMF) as the sacrificial electron donor solution for generating H_2 was prepared. In a vial covered with a membrane cap loaded with 3mL of photosensitizer (0.200 mM), 2 mL of cobaloxime HEC (0.100

mM) and 1.5 mL deionized water, was irradiated with white light (a four Cree XP-G3 warm white LED array) in total for 3 hours. All the solutions were prepared with DMF. After each hour, the 1.5 mL of headspace samples were taken and injected into the GC via syringe for analysis.

2.2 Synthetic methods

2.2.1 Synthesis of the acceptor ligand

Scheme 2-1 General scheme for the synthesis of the acceptor ligand (**A**)

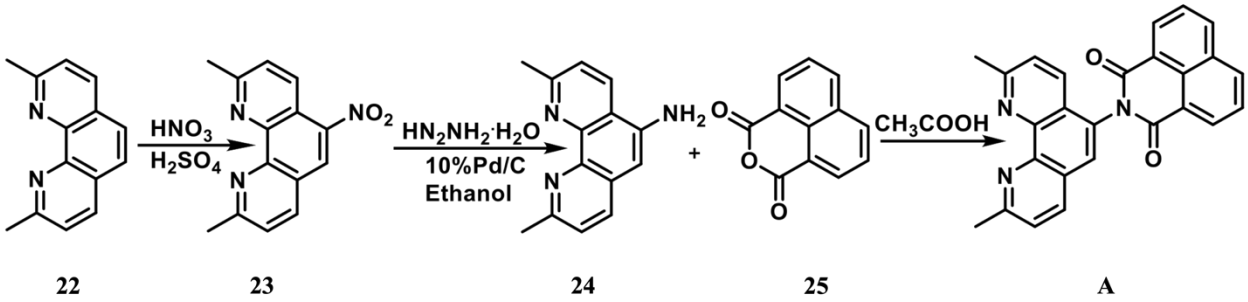

The synthesis of the **A** follows the nitration of 2,9-dimethyl-1,10-phenanthroline (**22**) to 5-nitro-2,9-dimethyl-1,10-phenanthroline (**23**) which was then reduced over 10% Pd/C using hydrazine to 5-amino-2,9-dimethyl-1,10-phenanthroline (**24**). At last, **24** was coupled with 1,8-naphthalic anhydride (**25**) in acetic acid to give the acceptor ligand **A** as a yellow solid in 21% yield to the starting material **22**. Structures of previously reported and known molecules were confirmed by comparison of ^{1}H NMR spectra to literature values.[50]

5-Nitro-2,9-dimethyl-1,10-phenanthroline (**23**).[29] 2,9-Dimethyl-1,10-phenanthroline (**22**, 1000 mg, 4.80 mmol) was dissolved in 20 mL of concentrated sulfuric acid (98%) and heated to 115 ℃ for 15 minutes. Concentrated nitric acid (5.00 mL, 70%) was added to the hot mixture and heating was maintained at 115 ℃ for 3 hours. Then, the hot solution was poured onto ca. 200 g of ice and

a concentrated sodium hydroxide solution (≈ 5.00 N) was added slowly until the precipitate that was the product **23** formed and the color of the solution visibly changed from yellow to green (pH ≈ 8). The resulting mixture was washed with dichloromethane (DCM) three times and dried over sodium sulfate. The solvent was removed by rotary evaporation and dried at 100 ℃ in a vacuum oven overnight to yield **23** (535 mg, 2.11 mmol) as a yellow solid in 44% yield.

^{1}H NMR (300 MHz, $CDCl_3$) δ 8.93(d, 1H), 8.62 (s, 1H), 8.29 (d, 1H), 7.71 (d, 1H), 7.65 (d, 1H), 3.01 (s, 3H), 1.98 (s, 3H).

5-Amino-2,9-dimethyl-1,10-phenanthroline (**24**).[29] To a suspension of **23** (535 mg, 2.11 mmol) in ethanol (EtOH), approximately 180 mg of 10% w/w Pd/C was added under N_2 atmosphere. After 10 minutes, an excess amount of hydrazine monohydrate (2.00 mL, 96.0 mmol) was added, and the reaction was left to stir for 24 hours at 80 ℃. The resulting black suspension was filtered out on a Celite ® pad. The solvent was removed by rotary evaporation; the resulting yellow solid was washed with water three times and re-dissolved in DCM. After drying over sodium sulfate, DCM was removed by rotary evaporation to yield **24** (400 mg, 1.78 mmol) as a yellow solid in 84% yield.

^{1}H NMR (300 MHz, $CDCl_3$) δ 8.16 (d, 1H), 4.87 (d, 1H), 7.49 (d, 1H), 7.39 (d, 1H), 6.90 (s, 1H), 4.18 (s, 2H), 2.91 (s, 3H), 2.87 (s, 3H).

2-(2,9-dimethyl-1,10-phenanthrolin-5-yl)-1H-benzo[de]isoquinoline-1,3(2H)-dione (**A**)[29]. 1,8-naphthalic anhydride **25** (353 mg, 1.78 mmol) and **24** (400 mg, 1.78 mmol) were heated at 120 ℃ to reflux in glacial acetic acid (20 mL) for 24 hours. The solvent was removed using rotary evaporation and the resulting solid was redissolved in DCM and washed with water three times. DCM was removed using rotary evaporation. Before purification, the product was dried at 100 °C

in a vacuum oven overnight. The crude yellow solid was purified using column chromatography on silica (1% of MeOH in DCM) to obtain a 56% yield of yellow solid.

^{1}H NMR (300 MHz, $CDCl_3$) δ 8.65 (m, 2H), 8.37 (m, 2H), 8.34 (d, 1H), 7.86 (m, 4H), 7.53 (d, 1H), 7.42 (d, 1H), 2.99 (s, 3H), 2.96 (s, 3H).

ESI-MS (ESI$^+$): Calcd for $C_{26}H_{17}N_3O_2$: *m/z* =403.13. Found: *m/z* =404.1389.

2.2.2 Synthesis of anchoring ligands

2.2.2.1 Synthesis of An1

Scheme 2-2 General scheme for the synthesis of the anchoring ligand for **An1**

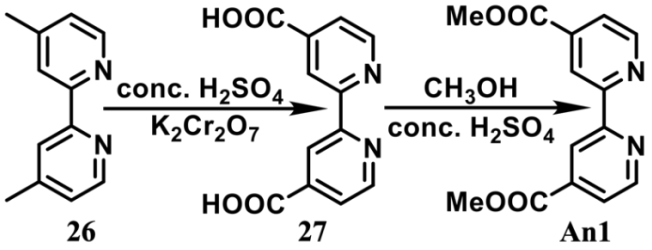

The synthesis was started with the oxidation reaction of the two methyl groups on 4,4'-dimethyl-2,2'-bipyridine (**26**) into carboxylic acid groups by the oxidizing agent potassium dichromate ($K_2Cr_2O_7$) in a strong acidic environment to yield 4,4'-dicarboxylic acid-2,2'-bipyridine (**27**). Since **27** is sparingly soluble, it was necessary to convert the carboxylic groups into the ester groups to make it soluble for further synthesis. With the addition of MeOH and the conc. H_2SO_4 as the catalyst, the anchoring ligand 4,4'-methoxycarbonyl-2,2'-bipyridine (**An1**) was prepared with an overall yield of 67%. Structures of previously reported and known molecules were confirmed by comparison of ^{1}H NMR spectra to literature values.[50]

4,4'-Dicarboxylic acid-2,2'-bipyridine (**27**). First, $K_2Cr_2O_7$ (3.00 g, 3.40 mmol) was dissolved in 20 mL of conc. sulfuric acid (98%) and heated to 80 ℃ for 15 minutes. 4,4'-Dimethyl-2,2'-bipyridine **26** (1.00 g, 5.43 mmol) was added in portions to the hot mixture. The reaction was kept under reflux for 2 hours. There was a clear visible color change from orange to green. The resulting mixture was then poured in 400 mL of water and a white precipitate formed. The precipitates were then filtered out through vacuum filtration and dried at 100 ℃ in a vacuum oven overnight to yield **27** (1.00 g, 4.07 mmol) as a white solid in 75% yield.

^{1}H NMR (300 MHz, DMSO-d_6) δ 8.94(s, 1H), 8.92 (s, 1H), 8.85 (s, 2H), 7.94 (s, 1H), 7.92 (s, H).

4,4'-methoxycarbonyl-2,2'-bipyridine (**An1**).[30] Conc. sulfuric acid (2.00 mL, 98%) was added to 4,4'-dicarboxylic acid-2,2'-bipyridine **27** (1.00 g, 4.07 mmol) in 50 mL of MeOH, and the reaction was kept for 24 hours at 70 ℃. The reaction mixture was then poured into 250 mL of water and the pH was adjusted to 8 with 25% (w/v) sodium hydroxide solution. The white slurry was extracted with DCM three times and DCM was removed by rotary evaporation. The resulting white solid was dried at 80℃ in a vacuum oven overnight to yield **An1** (1.00 g, 3.66 mmol) in 90% yield.

^{1}H NMR (300 MHz, DMSO-d_6) δ 8.96(s, 2H), 8.88 (s, 2H), 7.92(s, 2H), 4.00 (s, 6H).

2.2.2.2 Synthesis of An2

Scheme 2-3 General scheme for the synthesis of the anchoring ligand for **An2**

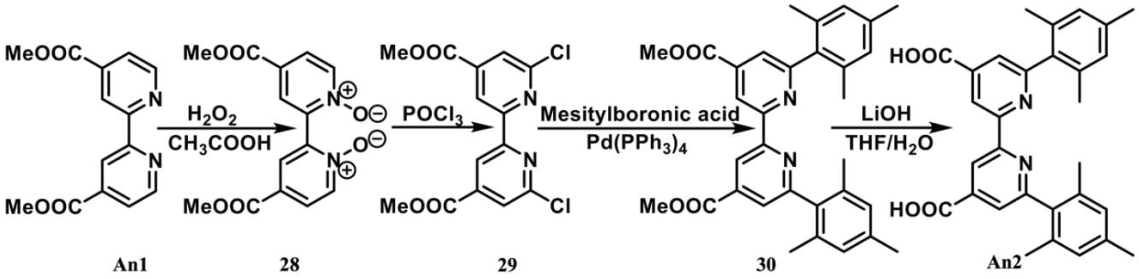

The general synthesis of 6,6'-dimesityl-4,4'-dicarboxylic acid-2,2'-bipyridine (**An2**) was started with 4,4'-methoxycarbonyl-2,2'-bipyridine (**An1**). To ensure there was no addition onto the nitrogen atoms on bipyridine, a protecting group was added to form N-oxy groups with hydrogen peroxide (H_2O_2) on **An1**. Then, a bulky group could be added on positions 6 and 6' of the pyridine rings first by heating **28** with phosphorus(V) oxychloride and isolating the resulting intermediate 6,6'-dichloro-4,4'-methoxycarbonyl-2,2'-bipyridine (**29**). Next, the two mesityl groups replaced the chloride positions on **29** via the Suzuki coupling using mesitylboronic acid with a $Pd(Ph_3)_4$ catalyst to give 6,6'-dimesityl-4,4'-methoxycarbonyl-2,2'-bipyridine (**30**). The last step to form **An2** was to convert the esters into the carboxylic acids as the anchoring group to attach the furthering NiO film on the photocathode. Finally, **An2** formed via the saponification reaction of adding lithium hydroxide (LiOH) with a general yield of 11%. Structures of previously reported and known molecules were confirmed by comparison of ^{1}H NMR spectra to literature values.[50]

1,1'-Dioxy-4,4'-methoxycarbonyl-2,2'-bipyridine (**28**).[31, 32] An excess amount of H_2O_2 (4.00 mL, 30 %) was added into the solution of 4,4'-methoxycarbonyl-2,2'-bipyridine **An1** (1.00 g, 3.66 mmol) in glacial acetic acid (15 mL) and the reaction mixture was heated up to 120 ℃ for 4 hours under reflux. Then, another 10 mL of H_2O_2 was added and the reaction was kept for another 6

hours as remaining conditions. The resulting solution was cooled in the fridge overnight and the precipitated colorless crystals formed, which were separated via vacuum filtration in 66% yield. No NMR result was obtained but further NMR characterizations confirms this compound was synthesized.

6,6'-Dichloro-4,4'-methoxycarbonyl-2,2'-bipyridine (**20**).[31] 1,1'-Dioxy-4,4'-methoxycarbonyl-2,2'-bipyridine **19** (730 mg, 2.42 mmol) was added carefully into an excess amount of phosphorus(V) oxychloride ($POCl_3$) and heated to 80 degrees under reflux with N_2 atmosphere for 6 hours. There was a visible color change for the reaction mixture from colorless to black. The resulting hot solution was quenched on 50 g of ice and followed neutralization for the mixture to pH 8 using dropwise addition of ammonium hydroxide (NH_4OH). The resulting viscous mixture was mixed with the silica gel to remove the black impurities. Then the mixture of product with silica gel was washed with DCM three times by vacuum filtration, and the filtrate was collected. DCM was removed by rotary evaporation and resulted in the gray solid in 36% yield.

^{1}H NMR (300 MHz, $CDCl_3$) δ 8.86 (s, 2H), 7.95 (s, 2H), 4.07 (s, 6H).

6,6'-dimesityl-2,2'-bipyridine-4,4'-dicarboxylate dimethyl ester (**20**).[33] 6,6'-dichloro-4,4'-methoxycarbonyl-2,2'-bipyridine (300 mg, 0.87 mmol), 2,4,6-trimethylphenylboronic acid (295 mg, 1.80 mmol), potassium carbonate (212 mg, 1.53 mmol) and tetrakis(triphenylphosphine)palladium(0) (92.0 mg) were added into toluene for heating under reflux overnight at 110 °C. The reaction was kept under N_2 atmosphere and was covered with aluminum foil to avoid the light. The solvent in the resulting mixture was removed by rotary evaporation and the crude product was purified via column chromatography in DCM. DCM was removed by rotary evaporation and resulted in the white solid in 67%.

^{1}H NMR (300 MHz, $CDCl_3$) δ 8.92 (s, 2H), 7.82(s, 2H), 7.02 (s, 2H), 3.95 (s, 6H), 2.38 (s, 6H), 2.11 (s, 12H).

6,6'-Dimesityl-2,2'-bipyridine-4,4'-dicarboxylic acid (**An2**).[33] 6,6'-dimesityl-2,2'-bipyridine-4,4'-dicarboxylate dimethyl ester (300 mg, 0.58 mmol) and an excess amount of lithium hydroxide (150 mg, 6.26 mmol) was dissolved in the solution of 20 mL of 7:1 THF:water solution. This reaction was kept overnight under reflux at 60 °C. The THF in the resulting reaction mixture was first removed by rotary evaporation and hydrochloric acid (HCl, 37%) was added to make the pH to around 2. The precipitation formed during the addition of HCl, and it was filtered out via vacuum filtration. The yield of the resulting white solid was 70%.

^{1}H NMR (300 MHz, DMSO-d_6) δ 8.73(s, 2H), 7.73 (s, 2H), 7.02 (s, 4H), 2.33 (s, 6H), 2.03 (s, 12H).

ESI-MS (ESI^+): Calcd for $C_{30}H_{28}N_2O_4$: *m/z* =480.20. Found: *m/z* =481.2116.

2.2.3 Synthesis of copper(I) photosensitizers

First of all, two ligands around the copper(I) were synthesized and purified with respective procedures separately (*vide supra*). Next, the HETeroleptic PHENanthroline (HETPHEN) concept was applied in the synthesis to avoid the formation of homoleptic complexes.[34, 35] In the previous studies, Ru polypyridine complexes are both thermodynamically and kinetic stable. However, the diimine (2,2'-bipyridine or 1,10-phenanthroline) ligand sphere around Cu(I) complexes exchange rapidly and makes it difficult to isolate pure heteroleptic complexes with two diimine ligands. To overcome this defect, Schmittel *et al*. created the idea of anchoring one of the diimine ligands with a bulky group on the ortho position of the N atom firstly with the center Cu(I) with equivalent

molar ratio, another ligand with the smaller group will be installed with the equivalent molar ratio later.[35]

Tetrakis(acetonitrile)copper(I) hexafluorophosphate (0.100 mmol) and the bulkier ligand (0.100 mmol) were dissolved in degassed DCM under the N_2 atmosphere. The resulting yellow solution was stirred at room temperature for 20 minutes and the solution of another ligand (0.100 mmol) dissolved in degassed DCM under N_2 was added using a syringe through the septum and resulted in the dark red solution after 20 minutes stirring at room temperature. The DCM was removed by rotary evaporation.

2.2.3.1 Synthesis of WEI1

Scheme 2-4 General scheme for the synthesis of **WEI1**

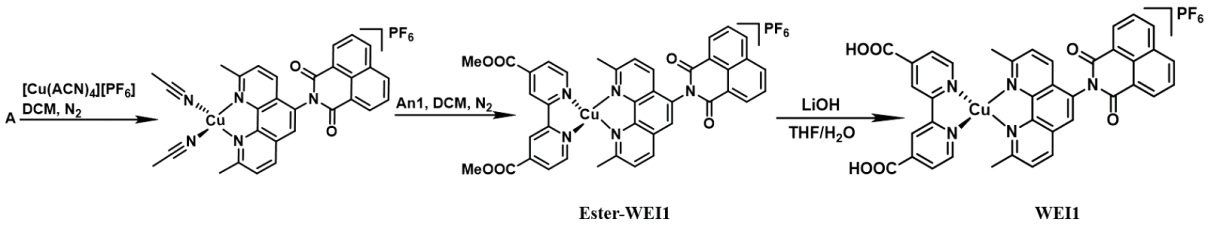

Ester-WEI1 WEI1

In the synthesis of **WEI1**, the first ligand was chosen as **A** and the second ligand was chosen as **An1**. For solubility reasons the ester groups of **An1** were converted into the carboxylic acid groups by saponification post-metalation. The yield of **WEI1** was not determined since the final complex was not isolated, so the following characterizations were carried out on **Ester-WEI1**.

^{1}H NMR (500 MHz, $CDCl_3$) δ 8.78 (m, 6H), 8.53 (d, 1H), 8.40 (d, 2H), 8.23 (d, 1H), 8.14 (s, 1H), 7.82 (m, 6H), 7.74 (d, 2H), 4.00 (s, 3H), 2.62 (s, 3H), 2.51 (s, 3H).

2.2.3.2 Synthesis of WEI2

Scheme 2-5 General scheme for the synthesis of **WEI2**

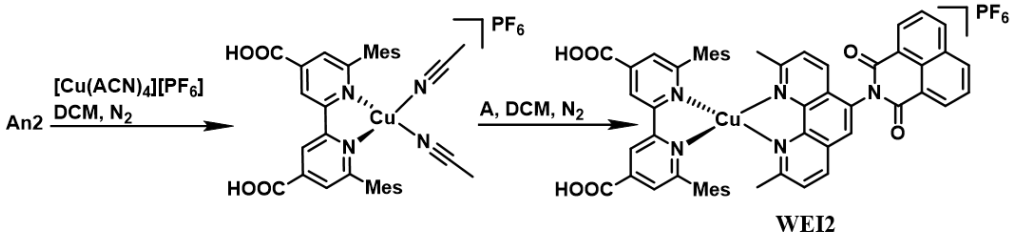

In the synthesis of **WEI2**, the first ligand was chosen as **An2,** and the second ligand was chosen as **A**. The overall yield of this complex was 34% after column chromatography purification and the details will be discussed in the following section.

^{1}H NMR (300 MHz, DMSO-d_6) δ 11.23 (s, 2H), 9.15 (d, 1H), 8.75 (m, 8H), 8.24 (m, 2H), 7.98 (m, 3H), 7.24 (m, 6H), 6.02 (s, 6H), 2.29 (s, 6H), 1.08 (s, 12H).

ESI-MS (ESI$^+$): Calcd for $C_{56}H_{45}CuN_5O_6$ ([M-PF_6]$^+$): *m/z* =946.27. Found: *m/z* =946.2652.

2.2.3.3 Synthesis of WEI3

Scheme 2-6 General scheme for the synthesis of **WEI3**

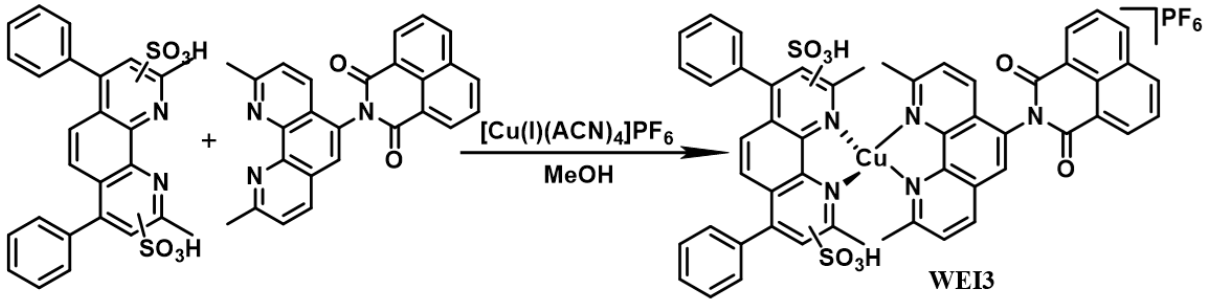

In the complex **WEI3**, the anchoring group attached to the semiconductor surface was changed to sulfonic acid to increase the affinity. The starting material for the anchoring ligand in this

molecule was bathocuproinedisulfonic acid which was obtained from an external supplier. Since the four groups around Cu(I) center are methyl groups, there was no need to apply HETPHEN approach. All the same mole equivalent of each starting material were stirred with MeOH in the reaction flask under the N_2 atmosphere for 30 minutes. MeOH was removed by rotary evaporation and the resulting dark red solid was the desired product with the yield of 69%.

^{1}H NMR (300 MHz, DMSO-d_6) δ 8.31 (m, 2H), 8.52 (m, 6H), 8.48 (s, 1H), 7.98 (m, 12H), 7.67 (m, 2H), 7.56 (m, 2H).

ESI-MS (ESI$^+$): Calcd for $C_{52}H_{37}CuN_5O_8S_2$ ([M-PF_6]$^+$): *m/z* =986.14. Found: *m/z* =986.1378.

^{13}C NMR (300 MHz, DMSO-d_6) δ 164.73, 161.18, 159.20, 158.82, 157.98, 149.29, 149.00, 148.88, 143.62, 143.12, 142.61, 138.21, 136.33, 136.29, 135.87, 135.37, 132.93, 132.11, 131.84, 131.47, 130.20, 129.76, 128.97, 128.93, 128.03, 127.80, 127.11, 126.97, 126.82, 126.60, 126.50, 126.02, 125.30, 123.99, 123.17, 119.51, 49.05, 26.09, 25.99, 25.95, 25.88.

2.2.4 Column chromatography purification for the synthesized molecules

Herein, we used the column chromatography technique to purify some of the synthesized molecule. The glass column was filled up with sand on the bottom, silica gel was used as the stationary phase, and v/v DCM:MeOH 99:1 as the mobile phase. The mixture of silica gel and the mobile phase was pre-made in the beaker, and then was poured into the column. The concentrated solution containing the target molecule was added on the top of the column using the pipette and then flashed with the mobile phase. Each eluted fraction was monitored by thin-layer chromatography (TLC) of tracking the movement of the point on the TLC plate under the hand

UV light. The solvent in each fraction was then evaporated by pressure and the structure was determined by NMR.

2.3 Synthesis of cobaloxime hydrogen evolving catalyst

Scheme 2-7 General scheme for the synthesis of chloro(pyridine)cobaloxime

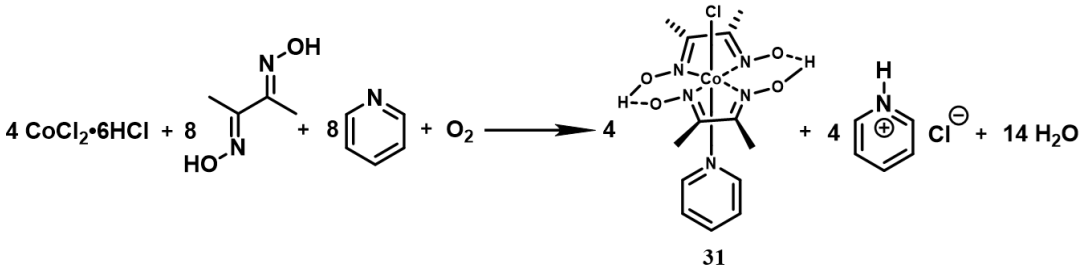

Chloro(pyridine)cobaloxime (**31**).[38] Cobalt chloride hexahydrate (500 mg, 2.10 mmol) and dimethylglyoxime (dmg, 475 mg, 4.10 mmol) were first added in a 2-neck round bottom flask containing 95% EtOH with stirring under the room temperature and N_2 atmosphere for 20 minutes. Then, pyridine (320 mg, 4.05 mmol) was added to the reaction mixture for another 20 minutes. Water (5.00 mL) was added into the resulting reaction mixture and was kept under the air for 24 hours. The resulting yellow precipitation was collected by vacuum filtration with the yield of 60%.

2.4 Fabrication of NiO|C-A1 photocathode

Scheme 2-8 General schematic illustration for the photocathode assembly

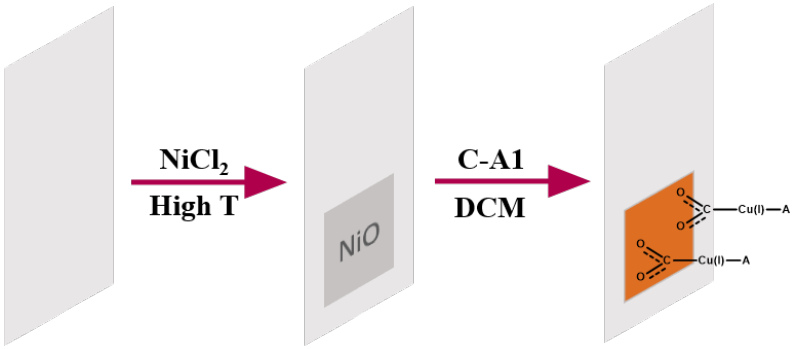

Scheme 2-8 shows the general procedure of the **NiO|C-A1** fabrication. Firstly, the p-type semiconductor material NiO was deposited on the fluorine-tin oxide (FTO) glass and then the dye molecules were attached on the NiO film.

2.4.1 Preparation of NiO film on the FTO glass

The procedure of making the NiO film was adapted from a previously reported procedure.[39] The pre-cut FTO glass pieces with the sizes around 2cm×3cm were sonicated in the following sequence of methanol, ethanol, and distilled water for 10 minutes each. Then, those pieces were dried and kept at 100 °C. At the same time, the $NiCl_2$-co-polymer gel was prepared as follows. $NiCl_2$ (1.00 g, 7.69 mmol) and 1.0 g of triblock co-polymer poly(ethylene glycol)-block-poly(propylene glycol)-block-poly(ethylene glycol) (PEG-PPG-PEG) were sonicated in a v/v H_2O: MeOH 4:6 solution of for 5 minutes in a centrifuge tube. The resulting mixture was left at room temperature for three days to observe two separate layers, and the upper supernatant layer was collected for future use. Next, one drop of $NiCl_2$-co-polymer gel was applied on the conductive side of FTO glass, and the doctor blade technique was used to make the gel drop into a thin film in an area of 1 cm × 1 cm (as defined through the application of tape). The film was dried in an 80 °C oven for 10 minutes and followed by placing it into the 550 °C furnace for 40 minutes for calcination of the organic polymer. This process was repeated 3×. At last, a gray film was observed on the FTO glass, and all the fabricated films were stored at 90 °C for future use. The pyrolytic decomposition of $NiCl_2$-co-polymer gel precursor to form a NiO film is given in the **Equation 2-1**.[54]

$$NiCl_2 \cdot 6H_2O \xrightarrow{heat} NiO + 2HCl\uparrow + 5H_2O\uparrow \quad (2\text{-}1)$$

2.4.2 Loading the molecules on the NiO films

Solutions containing the prepared dye molecules with anchoring groups were prepared in DCM with a concentration of 0.1 mM in a vial. One of the NiO films was placed in the solution with stirring for 48 hours after which there was a physical color change on the NiO films. The resulting photoelectrode was stored in the dark**.**

Chapter 3 Results and Discussion

3.1 Structural characterization

3.1.1 Structural characterization of Ester-WEI1

New ligands and complexes reported in this work were characterized using standard spectroscopic techniques. ^{1}H NMR was used as the first tool to determine the proposed structure of these new chemical species. Owing to the difficulty of preparing and isolating the carboxylic acid derivative, **WEI1**, the following is a comment on the structural character of **Ester-WEI1**, the ester protected derivative. Post isolation and purification, the ^{1}H NMR spectrum of **A** (**Figure A3**) shows resonances at δ 2.99 ppm and 2.96 ppm which correspond to the two methyl groups on 2,9-dimethyl-1,10-phenanthroline (dmp). Furthermore, the resonances between δ 7.53 ppm and 8.65 ppm correspond to an approximate integration of 11, matching well to the total number of hydrogens expected in the aromatic region of this molecule. Similarly, the ester of the anchoring ligand 4,4'-methoxycarbonyl-2,2'-bipyridine (**An1**) used in the preparation of **WEI1**, shows comparable positions of the peaks of methyl ester protons and those on the aromatic region match the theoretical results well including the integrations of the peaks (**Figure A5**).[30]

After complexation, the ^{1}H NMR spectrum of **Ester-WEI1** in **Figure 3-1** shows resonances at δ 2.54 ppm and 2.62 ppm corresponding to the methyl groups on dmp that are now shifted downfield as compared to the free ligand. The peak at δ 4.12 ppm is tentatively assigned to the methyl protons on the methyl ester, although the integration results in an incorrect number of protons. The rest of the peaks correspond to the hydrogens on the aromatic systems, as compared to the free ligands.

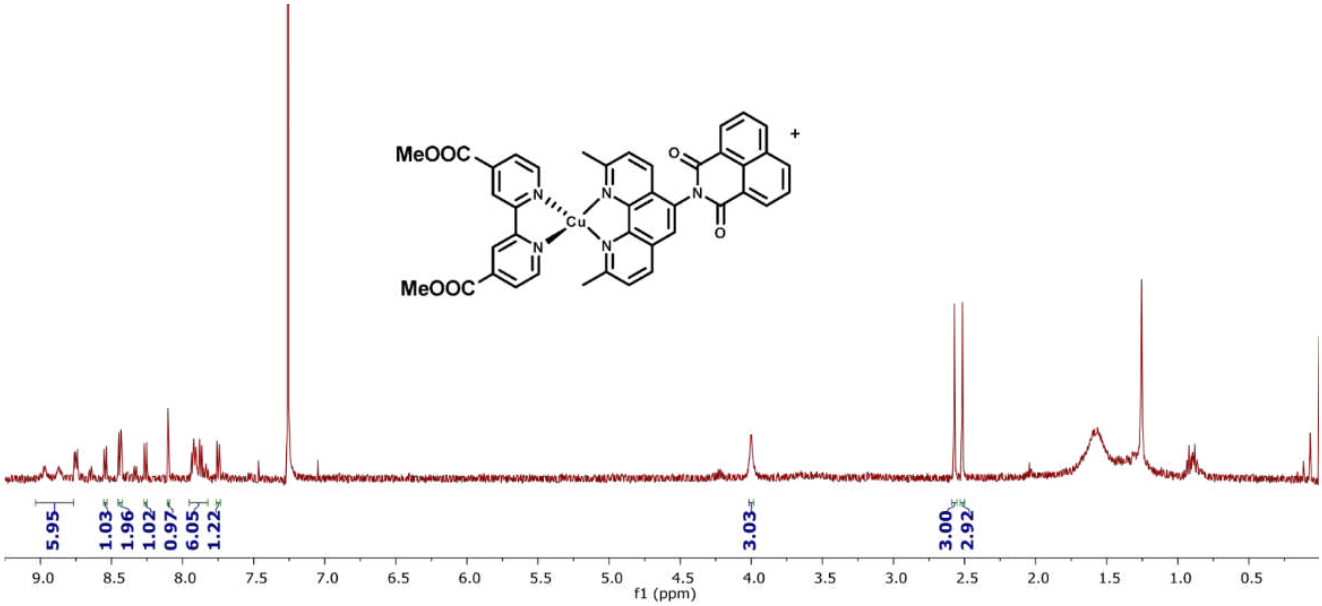

Figure 3-1. ^{1}H NMR spectrum of **Ester-WEI1** in $CDCl_3$ (500 MHz)

Figure 3-2 shows the ATR-IR spectrum of **Ester-WEI1**. The bands at 1700 cm^{-1} and 1750 cm^{-1} are tentatively assigned to carbonyl (C=O) stretching modes on the methyl ester and within the NMI moiety, respectively. Another band at 1200 cm^{-1} corresponds to the single bond connection of C-O on ester. Based on the peaks at δ 2.54 ppm and 2.62 ppm in the ^{1}H NMR spectrum and these important IR connections, it illustrates that the two ligands are bound to the Cu(I) center. All the results about the signals on NMR and IR spectra are concluded from the literature.[50]

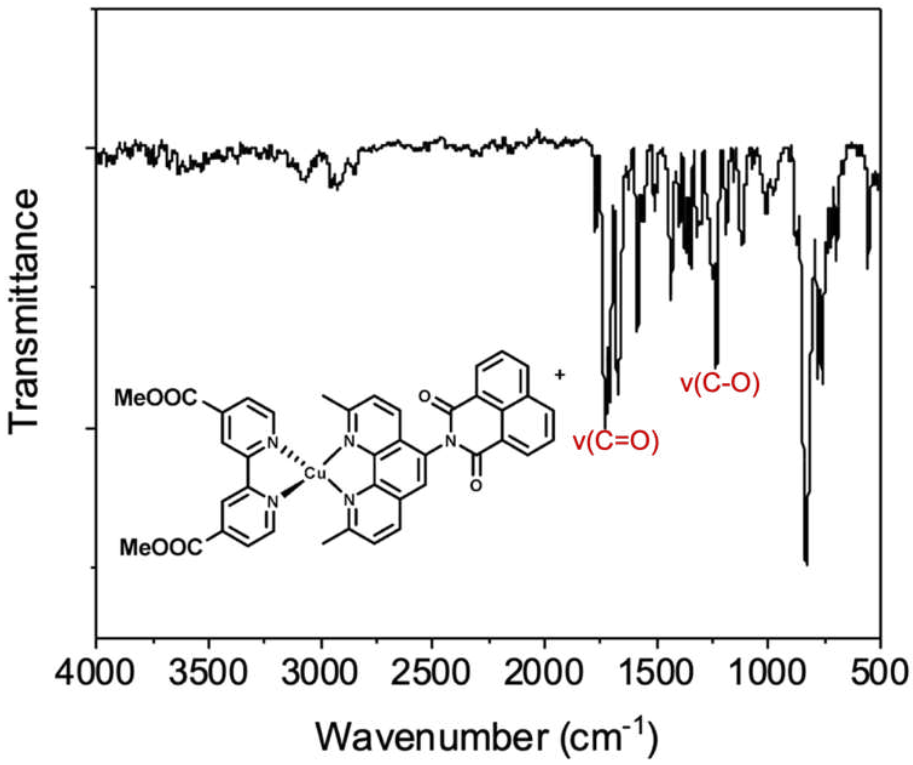

Figure 3-2. ATR-IR spectrum of **Ester-WEI1**

By comparing the ^{1}H NMR spectrum of **WEI1** and the ^{1}H NMR spectrum of another well-studied Cu(I) complex with a similar dmp-NMI-based ligand, the position of the peaks is qualitatively similar in the non-aromatic region between δ 2.5-2.75 ppm, and for aromatic protons between δ 7.30-8.85 ppm.[29] It is still possible that the isolated product is a mixture of heteroleptic and homoleptic complexes and important future investigations include obtaining mass spectrometry (MS) to confirm the identity of this compound.

3.1.2 Structural characterization of WEI2

As in **Section 3.1.1**, the structure of the ligands and **WEI1** were primarily characterized using ^{1}H NMR, together with mass spectrometry. The ^{1}H NMR of the anchoring ligand 6,6'-dimesityl-

2,2'-bipyridine-4,4'-dicarboxylic acid (**An2**) including the peaks on both aromatic and non-aromatic regions perfectly match the expectations.[33] Based on the ^{1}H NMR spectrum (**Figure 3-3**) of **WEI2** after complexation and purification, both the integrations and the peak positions are somewhat hard to distinguish. From MS analysis, it is clear that this procedure yields a mixture of products containing the homoleptic Cu(I) complex with two acceptor ligands **A** (**Figure A13**). The peak at 869.19 m/z corresponds to the exact mass of the homoleptic molecule. To solve this problem, purification needs to be done. Unfortunately, the current traditional silica column did not work for this complex, probably due to its high affinity to the stationary phase and its large molecular mass. Despite the product mixture, it is still possible to use this sample as a photosensitizer anchored to a SC film as the photoelectrode.

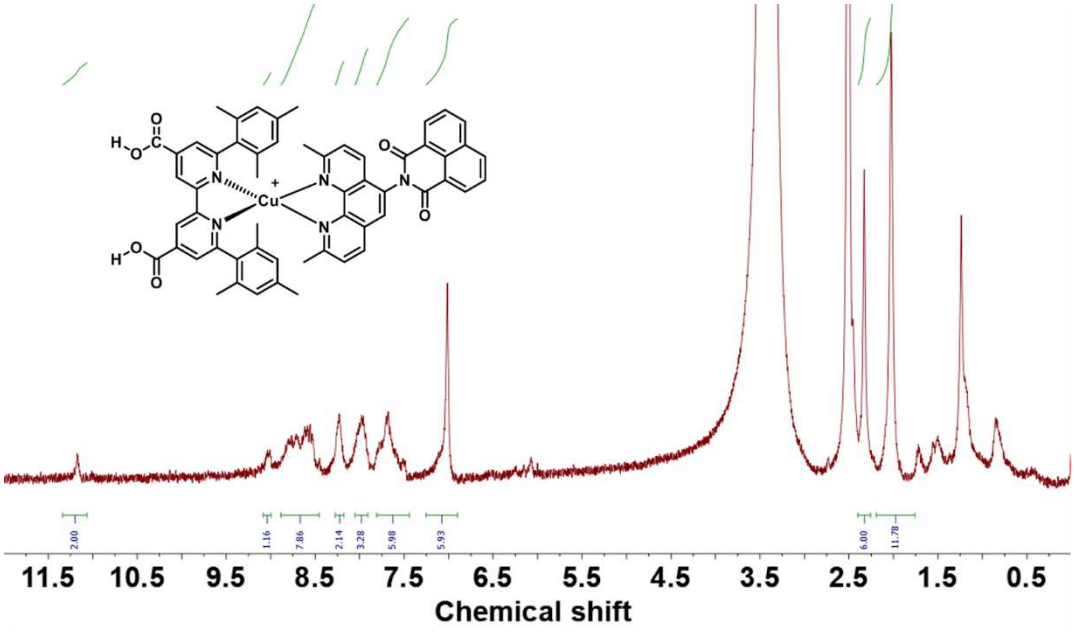

Figure 3-3. ^{1}H NMR spectrum of **WEI2** in DMSO-d_6 (300 MHz)

3.1.3 Structural characterizations on WEI3

The ^{1}H NMR spectrum of the bathocuproinedisulfonic acid ligand shows a peak at δ 2.78 ppm which corresponds to the protons of the two methyl groups on the structure (**Figure A10**). Furthermore, the peaks between δ 7.48 ppm and 7.91 ppm correspond to the expected hydrogens in the aromatic region. Since the bathocuproinedisulfonic acid obtained from the supplier was a mixture, meaning the sulfonic acid groups may be located on any number of positions on the whole structure. Therefore, we can only observe the overall integrations on the aromatic region corresponding well to the ligand structure. In the ^{1}H NMR spectrum of **WEI3** (**Figure 3-4**) the approximate integrations for those peaks between δ 7.40 ppm and 9.80 ppm is 23, which matches well to the total numbers of protons in the aromatic region of this molecule, and the protons from the four methyl groups are found at δ 2.55 ppm and 3.23 ppm. The ^{13}C NMR spectrum, the total number of carbons was determined to be 41.

The ^{1}H correlation spectroscopy (COSY) illustrates which ^{1}H signals are coupling to each other (**Figure A12**). Both x and y axes are the same 1D ^{1}H NMR spectra. By drawing a line through the general diagonal trend of the signals which represent the same protons correlate to themselves and those can be disregarded. In non-aromatic region, all the protons do not couple to the protons on neighboring carbons. This investigation meets the expectation since there is no proton on the neighbor carbon of the four methyl groups. In the aromatic region, there are strong correlation signals at the interceptions of δ 8.85 ppm and 8.30 ppm with 8.02 ppm, respectively. There are also the correlations between some protons at the interceptions of δ 7.50 ppm with 8.00 ppm. However, it is hard to assign these signals for two reasons: 1. This complex contains complicated aromatic systems. 2. On the anchoring ligand, the positions of sulfonate group are uncertain increasing the difficulty to identify the equivalent protons. From the MS of **WEI3**, and there is a

peak corresponding to the theoretical exact mass of the heteroleptic complex at 986.14 m/z (**Figure A14**).

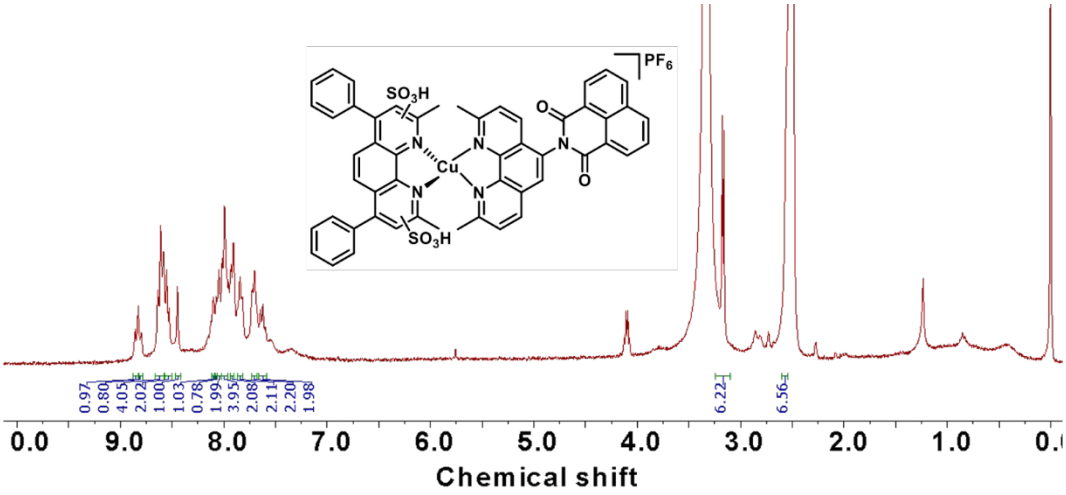

Figure 3-4 ^{1}H NMR spectrum of **WEI3** in DMSO-d_6 (300 MHz)

3.1.4 Structural characterizations on HEC

To study the ability of **WEI1**-**WEI3** to act as photosensitizers for proton reduction (both hetero- or homogenously), the previously reported champion molecular cobaloxime proton reduction catalyst **31** was synthesized.[38] This compound was synthesized by heating up a mixture of $CoCl_2$, dimethylglyoxime (dmg), and pyridine in MeOH in air and characterized by ATR-IR. As prepared, the Co(III) center is paramagnetic due to the d^6 system ([Ar]$4s^0 3d^6$ electron configuration) in octahedral geometry with 2 paired electrons and 4 unpaired. The unpaired electrons make NMR measurements difficult with the signals that might be very wide, and invalid integrations.[52] As a result the ^{1}H NMR of HEC was not measured. Instead, the ATR-IR spectrum in **Figure 3-5** illustrates some important information about bonding in the proposed structure. The stretching mode at 1495 cm^{-1} and the bending mode at 545 cm^{-1} correspond to the single bonds of Co with N and that with Cl, respectively. The stretching mode at 1250 cm^{-1} corresponds to the N-O bond.[50]

These connections preliminary proved that the expected bonds are formed, and the HEC was synthesized successfully. It is possible that ^{59}Co NMR could be used to detect the presence of cobalt in the complex.[53]

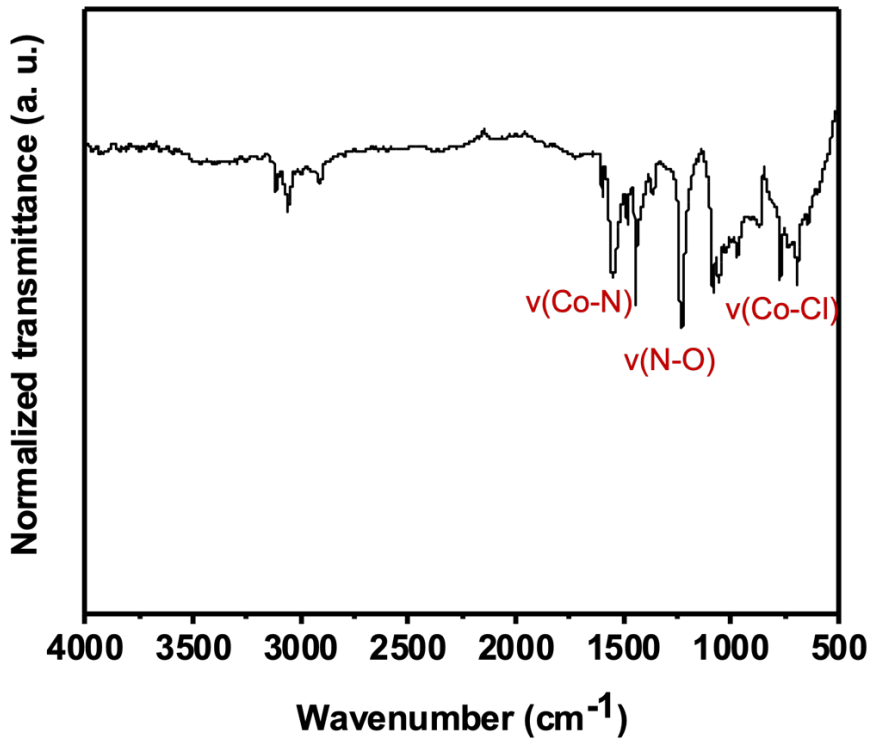

Figure 3-5. ATR-IR spectrum of **HEC**

3.2 Characterization of the NiO|C-A1 photoelectrode

To fabricate a photocathode and generate photocurrent, a nanostructured semiconductor (SC) film of NiO was deposited onto fluorine-doped tin oxide (FTO) on glass. Molecules with a carboxylic acid group (-COOH) or sulfonic acid group (-SO_3H) can be anchored to a SC surface through chemisorption. Chemisorption is a strong and specific type of adsorption that involves the formation of chemical bonds between the adsorbate (the molecule with the carboxylic/sulfonic

acid group) and the surface of the SC. The oxygen atoms in the carboxylic/sulfonic acid group can form coordination bonds with metal atoms on the SC surface.[56] where, a NiO film was soaked the in a 1 mM DCM Cu(I) complex solution with stirring for 48 hours.

Figure 3-6 shows the characterization of the fabricated photocathode of **WEI3** on NiO film. The PXRD patterns of NiO with (space group of $Fm\bar{3}m$) exhibit the simulated standard peaks at 2θ values of 37°, 43°, 63°, 75° and 79° which are assigned to (111), (200), (220), (311), and (110) planes, respectively (**Figure 3-6** a). From the PXRD of the NiO film on FTO a diagnostic reflection at $2\theta = 43°$ corresponding to the (200) plane of NiO is observed amongst the reflections attributed purely to FTO. Further analysis by SEM shows the NiO nanoparticles, and the energy-dispersive X-ray spectroscopy (EDS) combined with EDS provides the chemical composition of the NiO|FTO (**Table 3-1**). The result confirms the presence of Ni on the FTO glass with an atomic concentration of 27.79% and a weight concentration of 23.93%. There was an unexpected presence of phosphorus on the film might be as the contamination, but it did not affect the further characterizations on the photoelectrode.

Table 3-1. Elemental composition analysis by EDS

Element Name	Atomic Conc.	Weight Conc.
Oxygen	51.44%	23.93%
Nickel	27.79%	47.42%
Fluorine	13.59%	7.51%
Tin	5.77%	19.90%
Phosphorus	0.99%	0.89%

In IR spectra (ATR-IR for **WEI3** and DRIFTS for **NiO|WEI3**), modes associated with O-H bonds at the range of 3100-3750 cm^{-1} that is due to the by-product $Ni(OH)_2$ formed during heating up the $NiCl_2$ precursor co-polymer gel (**Equation 3-1**).[54]

$$NiCl_2 + 2H_2O \xrightarrow{heat} 2HCl\uparrow + Ni(OH)_2 \quad (3\text{-}1)$$

From the similar work of pyrolysis of $Ni(OH)_2$ as the precursor of Ismail *et al.,* the FTIR spectrum of NiO thin film synthesized at 400 °C there are bands at 611.43, 875.65, 1422, 1745, and 3776 cm^{-1} represent to the Ni-O interaction.[55] However, the range of DRIFTS measurement of **NiO|WEI3** was only above 700 cm^{-1}, and the results below that wavenumber are not able to prove. For the rest of the assigned signals, the small bands at around 850, 1325, 1750, and 3750 cm^{-1} in **Figure 3-6** c), all correspond to Ismail *et al.*'s work, but the band at 850 cm^{-1} seems more like to be the Ni-O interaction since those are two strong oscillators bound together.[50] Besides, there are common peaks in both IR spectra which prove that **WEI3** was successfully anchored on the NiO surface.[50] In **Figure 3-6** d), the UV-Vis spectra of both **WEI3** and **WEI3** on NiO film illustrates there is a weak peak at 470 nm that represents the ^{1}MLCT on the photoelectrode.

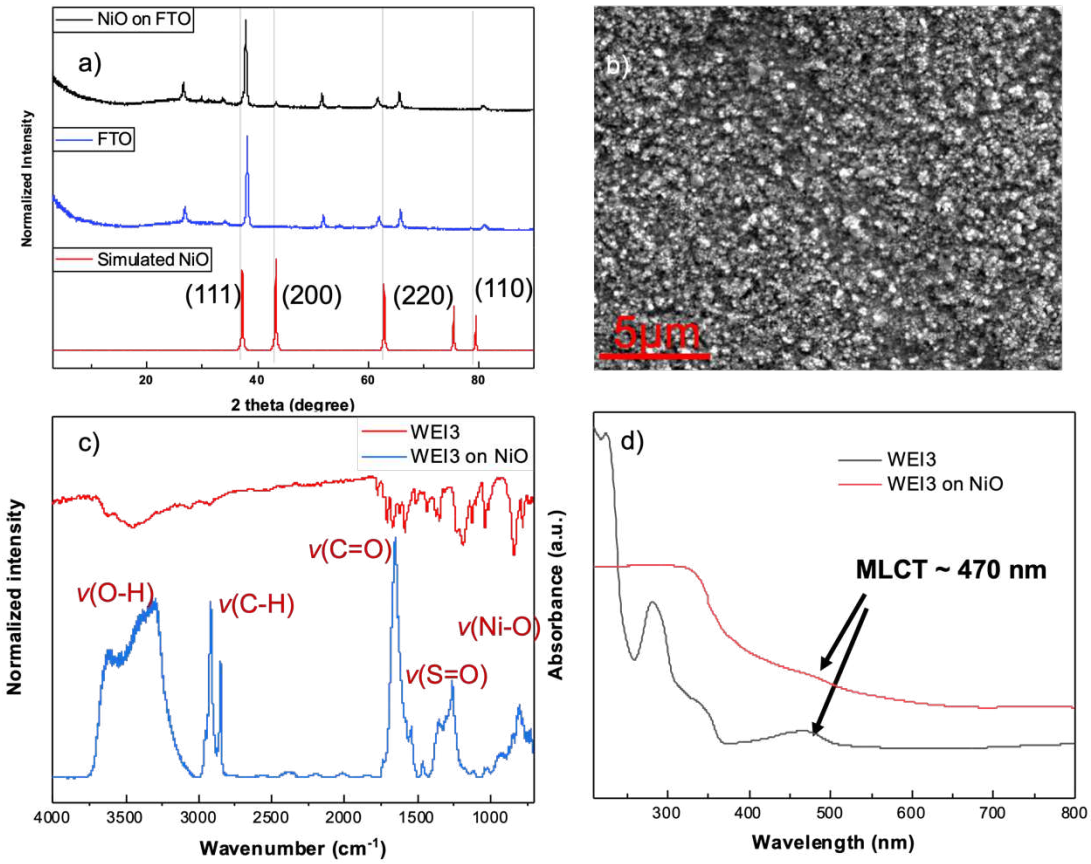

Figure 3-6. a) PXRD patterns of clean FTO glass (blue) and NiO film on the FTO glass (black), the simulated NiO pattern (red, ICSD: 3295872) is used as comparison. b) SEM image of the NiO film on the FTO glass. c) IR spectrum of **WEI3** (red) and DRIFTS of the functionalized NiO film (blue). d) UV-vis spectroscopy of **WEI3** (black) and the functionalized NiO film (red).

3.3 UV-Vis spectroscopy

In the UV-Vis results of the synthesized Cu(I) complexes, all three Cu(I) complexes have the expected metal-to-ligand charge transfer (MLCT) transition at around 470 nm. These positions of the MLCT are similar to the MLCT signal with the A-Cu-dmp complex which is shown in **Figure 3-7** c). For comparison, there is no MLCT band for the single **A** ligand since it did not attach to

the metal atom. Additionally, the MLCT band may contain singlet MLCT (^{1}MLCT) and/or weak triplet MLCT (^{3}MLCT) signal. The lower intensity and broadness of triplet MLCT peaks are primarily due to the spin selection rules and the probability of electron transitions between the ground state and excited triplet states. In UV-Vis spectroscopy, which involves the absorption of photons, transitions that involve a change in electron spin are usually less possible than those that maintain the same electron spin. As a result, the transition probability for ^{3}MLCT is lower compared to ^{1}MLCT, and the ^{3}MLCT peaks are weaker.[50, 58] However, identifying ^{3}MLCT peaks may require more sensitive experimental techniques or additional spectroscopic methods, such as time-resolved UV-Vis spectroscopy, which can capture transient species with short lifetimes like some triplet states. [57, 58]

Back to the experimental UV-Vis spectra, we can observe two significant bands other than the MLCT on both complexes and the acceptor ligand. The intense band at around 280 nm is assigned to the intraligand (IL) $\pi \rightarrow \pi^*$ transition of phenanthroline or bipyridine moiety, and another band at around 320 nm is assigned as IL $n \rightarrow \pi^*$ transition. This type of transition is commonly observed in molecules containing heteroatoms like O, N and S in the ligands, where the lone pair of electrons in the heteroatom's non-bonding orbital interacts with the adjacent π antibonding orbital.[50, 57]

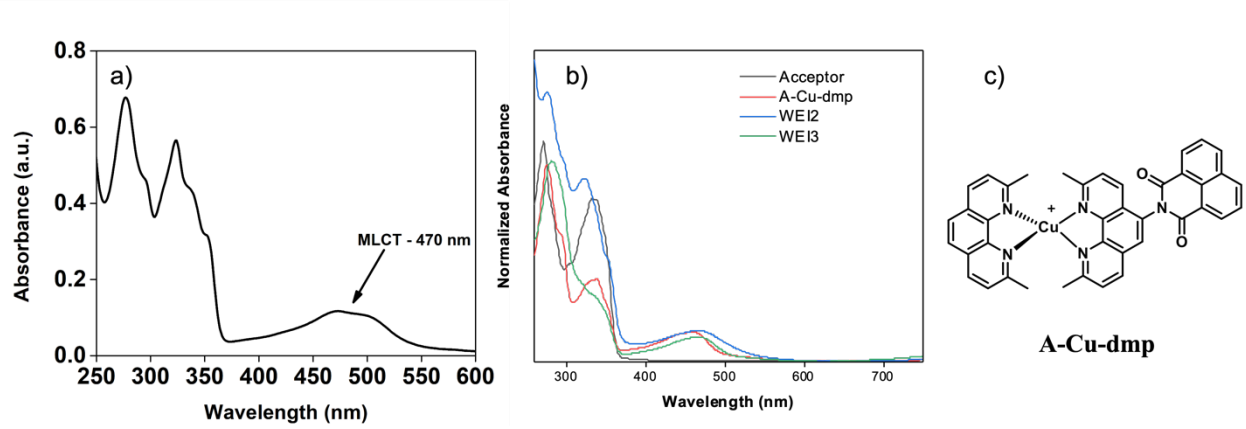

Figure 3-7. UV-vis spectra of a) **Ester-WEI1** and b) **A-Cu-dmp**, **WEI2** and **WEI3** compared with the acceptor only (all with concentration of 1mM of complexes in DCM and were filled in the cuvettes) and c) the complex of **A-Cu-dmp**.

3.4 Electrochemistry

To probe the ground-state electrochemical redox properties of the molecular photosensitizers **Ester-WEI1**, **WEI2** and **WEI3**, cyclic voltammetry (CV) was used, while to probe the photocurrent capabilities of the photoelectrodes, chronoamperometry (CA) was used. **Figure 3-8** provides the CV information of current Cu(I) complexes and where the Cu(I)/(II) redox couple appears at around 0.6V/0.5 V vs. Ag/AgCl but depends on the ligands of them attach. The presence of the anchoring ligand in these Cu(I) complexes does not provide an additional wave. However, the oxidation potential (E_{ox}) appears on two complexes connected with the bipyridine (**Ester-WEI1** and **WEI2)** is at ca. E_{ox} = 0.9 V, but this redox process is not reversible since no reduction potential (E_{red}) was observed. The reduction peaks of the NMI moiety in **Ester-WEI1** and **WEI3** are both observed at E_{red} = -1.25 V, which are more cathodic than the reduction peak in **WEI2** with E_{red} = -0.81 V. To compare with the single NMI moiety and the complex **A-Cu-dmp** (E_{red} = -1.08V), these peaks either shift cathodic or anodic position.[29, 59] Moreover, the Gibbs free energy between photoinduced electron transfer (ΔG_{ET}^{o}) is determined from the CV data. The excited state

of excited-state oxidation potential of these Cu(I) complexes can be estimated from the **Equation 3-2**, where E_{00} is zero-zero energy of the ^{3}MLCT. Since the MLCT for these complexes is at 470 nm, E_{00} can be calculated as 2.14 eV. Then, the value of ΔG_{ET}^{o} can be calculated based on **Equation 3-3**.[60, 61] the results of **Ester-WEI1** and **WEI3** are listed in **Table 3-2** as 0.01 eV and -0.29 eV, respectively.

$$E(Cu^{I/II*}) = E(Cu^{I/II}) - E_{00},\ E_{00} = hc/\lambda \quad (3\text{-}2)$$

$$\Delta G_{ET}^{o} = E(Cu^{I/II*}) - E_{pc}(A^{0/-I}) \quad (3\text{-}3)$$

Table 3-2. Oxidation and reduction potentials of **A**, **A-Cu-dmp**, **Ester-WEI1, WEI2 and WEI3**

Compound	E_{pc} (V) ($A^{0/-I}$)	E_{pa} (V) ($Cu^{I/II}$)	ΔG_{ET}^{o}(eV)
A	-0.952	-	**-**
A-Cu-dmp	-0.882	0.948	-
Ester-WEI1	-1.052	1.098	0.01
WEI2	-0.612	-	-
WEI3	-1.052	0.798	-0.29

These values are obtained from CV chromatogram, which were recorded in 0.1 M $TBAPF_6$ in ACN/DMF at υ = 100 mV s^{-1} with a 2 mm Pt button as the WE, Pt wire as the CE, and an Ag/AgCl wire as the RE. Potentials are referenced vs the Ag/AgCl redox couple converted to NHE. by adding +0.198 V.[62] Abbreviation used here: E_{pc} = potential at the peak cathodic current, E_{pa} = potential at the peak anodic current, and ΔG_{ET}^{o} = Gibbs free energy between photoinduced electron transfer.

To probe photocurrent generation at the photocathodes, chopped light chronoamperometry measurements were used. As compared to an unfunctionalized NiO film, films functionalized with **WEI2** or **WEI3** exhibit negative photocurrent when irradiated with white light. This experiment was carried out in 0.1 M $TBAPF_6$ in DMF solution with three-electrode system. This transient photocurrent was generated once the chromophore absorbs the light, and this photocurrent can be kept during the light-on period. **WEI3** functionalized films were shown to generate a higher photocurrent than those with **WEI2** where photocurrent densities are stable at around -2.8 $\mu A/cm^2$ (the photocurrent density reaches up to -6 $\mu A/cm^2$). However, by the comparison of the work in our group which was published for oxidation of water, the photocurrent density of **WEI3** is lightly lower than ca. 4 $\mu A/cm^2$ from the photoanode of the finished work.[29] However, in the second generation of the photoanode fabricated from Cu(I) triad, the photocurrent density could reach up to 20 A/cm^2 and that could be stabilized in the following chopped light activity.[59] From those work, we can continue adding the **HEC** during the CA experiment to observe if there is an increasing of the photocurrent in the future.

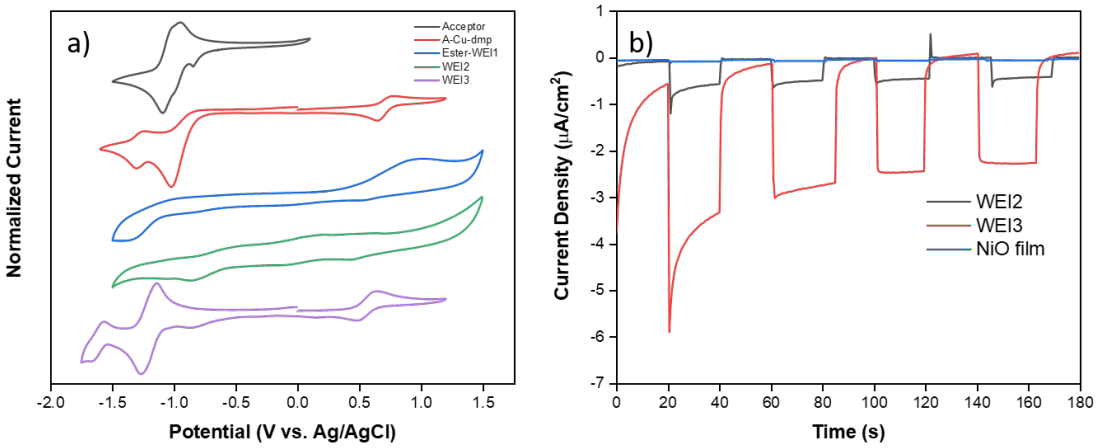

Figure 3-8. a) Cyclic voltammetry (CV) of **Ester-WEI1** (blue), **WEI2** (green), and **WEI3** (purple) compared with A and the model complex **A-Cu-dmp** which were recorded in 0.1 M $TBAPF_6$ in

ACN/DMF at scanning rate of 100 mV/s with a 3 mm Pt button as the WE, Pt wire as the CE, and an Ag/AgCl wire as the RE. b) Chronoamperometry (CA) of the photoelectrodes of **WEI2** (black), **WEI3** (red) and the blank NiO film (blue). 0.1 M $TBAPF_6$ in DMF was using as the electrolyte solution, the scanning period was 180s. In the apparatus, the fabricated photocathode anchored with **WEI2** and **WEI3** as the WE, Pt wire as the CE, and an Ag/AgCl wire as the RE.

3.5 Hydrogen evolution characterization

Prior to using the photoelectrodes as catalysts for proton reduction, **WEI3** was tested as a photosensitizer in a homogenous solution with the cobaloxime HEC. These experiments were carried out to establish where these molecular systems could be used to photocatalytically generate H_2. Comparing the chromatogram result to the calibration curve in **Figure A15** with the standard gas sample, the peak at 1.24 minutes represents hydrogen elution. **Table 3-3** lists the peak areas of the 3 mL of 0.2 mM of corresponding complexes with 2 mL of 0.2 mM of **HEC** and/without 2 mL of 10% v/v sacrificial electron donor (TEA) in DMF at pH = 5 (based on pH paper) under the visible white light since the MLCT of these two complexes are at 470 nm which is in the visible range. Based on the results, the peak areas existed even at the start of light irradiation since the natural light in the laboratory environment could also drive proton reduction. To ignore the original H_2 in the reaction vails, it is still clear that **WEI3** performs better than **WEI2** after three hours with 24974.24 μV•s. Even though **WEI2** contains some homoleptic complex product as the impurity, H_2 was still generated with a peak area of 2414.13 μV•s. The reaction was slow and with a low efficiency without TEA with the peak area increased from 454.76 μV•s to 4255.54 μV•s after 3 hours. Compared to trials with TEA, it confirms that the electron transfer plays a crucial role in proton reduction.

Table 3-3. Hydrogen peak areas of the synthesized Cu(I) complexes generated

Time (hour)	**WEI2**+TEA (μV•s)	**WEI3**+TEA (μV•s)	**WEI3** (μV•s)
0	2865.07	4895.64	454.76
1	-	-	1430.25
2	4003.95	18679.73	3487.41
3	5279.20	29869.88	4255.54

3.6 Computational analysis of the Cu(I) complexes

Density functional theory (DFT) calculations were performed on **WEI1**, **WEI2** and **WEI3**, which gives the visible localization of the frontier molecular orbitals in **Figure 3-9** for **WEI3**, and **Figure S26** for **WEI1** and **WEI2**. In **WEI3**, the lowest unoccupied molecular orbital (LUMO) is delocalized over the bathocuproine ligand except the two phenyl rings attached, and the highest occupied molecular orbital (HOMO) is delocalized over the bathocuproine ligand and Cu(I) center and on four carbon atoms of the dmp moiety on the **A** ligand. This is surprising as we anticipated that the position of LUMO should be located on the acceptor ligand. The same results were obtained in **WEI1** and **WEI2** (**Figure S26**). We can consider that the bathocuproine ligand is a better electron transfer acceptor (in the ground state) than the NMI moiety.[29] It is possible that this observation is a result of the incorporation of the sulfonate and carboxylate groups into the geometry optimized structure: their electron withdrawing effect may influence the position of the LUMO, and it is also possible that this effect will be mitigated when these groups are attached to a semiconductor surface.

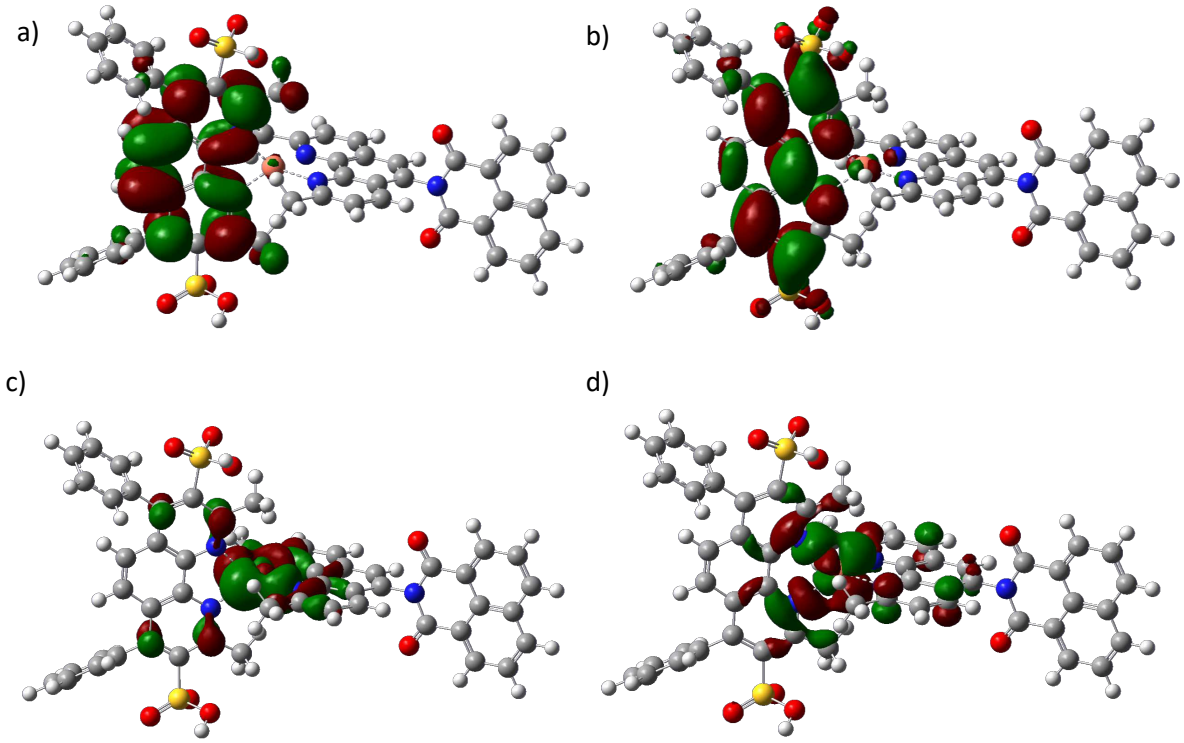

Figure 3-9. Graphical representations of a) LUMO +1, b) LUMO, c) HOMO, and d) HOMO-1 of **WEI3**. Method: DFT B3LYP 6-31G*(+, d). Abbreviations used in this figure: HOMO = highest occupied molecular orbital, and LUMO = lowest unoccupied molecular orbital.

Chapter 4 Conclusion and Outlook

4.1 Summary

In conclusion, this thesis focused on the design, synthesis, and characterization of three Cu(I) dye-sensitized photosensitizers (**Ester-WEI1**, **WEI2** and **WEI3**) for proton reduction. The structures of these photosensitizers were carefully characterized, and their UV-vis properties revealed efficient metal-to-ligand charge transfer (MLCT) absorption at 470 nm. Electrochemistry experiments, including cyclic voltammetry (CV) and chronoamperometry (CA), were conducted to investigate the redox behavior of the complexes.

The results from CV analysis demonstrated the presence of distinctive peaks, indicating the ability of the photosensitizers to undergo redox processes during light-induced electron transfer. However, only the **WEI2** and **WEI3** exhibited pronounced current responses in CA experiments, indicating their capability to generate the negative photocurrent.

Moreover, the hydrogen evolution experiments, carried out using **WEI2** and **WEI3**, yielded promising results as hydrogen gas generation was successfully achieved. This outcome underscores the potential of these Cu(I) complexes as efficient catalysts for proton reduction, showcasing their applicability in the development of renewable and sustainable hydrogen production systems.

Overall, this study contributes valuable insights into the design and application of Cu(I) photosensitizers for proton reduction, opening new avenues for advancing renewable energy technologies and addressing the challenges of sustainable hydrogen production. At the time of writing, this represents the first project in the current research group to explore the photosensitizer for proton reduction, the findings presented in this thesis lay the groundwork for further research

and optimization of these photosensitizers to enhance their performance and ultimately contribute to a greener and more sustainable future.

4.2 Future work

In the future, it is worth to optimize the structures of the photosensitizers. To enhance the catalytic efficiency and stability of the Cu(I) complexes, further investigations into the structure-activity relationship could be pursued. This might involve fine-tuning the ligand architecture or modifying the metal center based on insights gained from computational studies and advanced spectroscopic techniques. Synthesizing and characterizing different ligands with acceptor functionalities or trying to add the donors could lead to enhanced light absorption, redox properties, and proton reduction capabilities.

In pursuit of advancing the application of Cu(I) dye-sensitized photosensitizers for proton reduction, one of the prominent future plans is to augment the photocurrent density of the photocathode. By optimizing the photosensitizers design and exploring innovative ligand architectures, the aim is to enhance light harvesting and electron transfer efficiency, thereby maximizing the catalytic performance. Additionally, the quantification of the hydrogen produced by the photosensitizers is crucial for precisely assessing their efficiency. Moreover, to translate the research findings into practical hydrogen production systems, investigations into the application of the Cu(I) complexes in dye-sensitized photoelectrochemical cells (DS-PEC) will be undertaken. This entails studying the hydrogen production on the photocathode surface under controlled conditions, bringing us closer to realizing the potential of these photosensitizers for sustainable and efficient hydrogen generation.

References

1. International Environmental Agency, *World Energy Outlook 2022*, **2022**, 239.
2. Retrieved from https://ourworldindata.org/grapher/years-of-fossil-fuel-reserves-left. (Accessed from February 23, 2023)
3. Hayat, M. B.; Ali, D.; Monyake, K. C.;Alagha, L. and Ahmed, N. Solar energy—A look into power generation, challenges, and a solar-powered future.*Int. J Energy Res*, **2018**, 42 (12), 3798-3816.
4. O'Regan, B. and Gratzel, M.A. Low-cost, High-efficiency Solar Cell based on dye-sensitized colloidal TiO_2 films, *Nature*, **1991**, 353 (6346), 737-740.
5. Aung, L. L.; Tertre, E.; Worasith, N.; Suksabye, P.; Thiravetyan, P. The Capacity of Activated Kaolins to Remove Colour Pigments from Rice Bran Oil: The Effects of Acid Concentration and Pre-Heating Prior to Activation. *Clay Minerals.* **2014**, 49 (4), 513–526.
6. Kim, D.; Sakimoto, K. K.; Hong, D.; and Yang, P. Artificial Photosynthesis for Sustainable Fuel and Chemical Production. *Chem. Int. Ed*. **2015**, 54, 3259 – 3266.
7. Alstrum-Acevedo, J. H.; Brennaman, M. K.;and Meyer, T. J. Chemical Approaches to Artificial Photosynthesis. 2 *Inorg. Chem.* **2005**, 44(20), 6802-6827.
8. Subramni, V.; Basile, A. and Veziroglu, T. *Comp of Hydro Energy*. 1st Ed. **2015**, 289-317.
9. Ju, H.; Lin, J.; Tian T.; Xie, D. and Xu, R. NADPH Homeostasis in Cancer: Functions, Mechanisms and Therapeutic Implications. *Sig Transduct Target Ther.* **2020**, 5, 231.
10. Fassioli, F.; Dinshaw, R.; Arpin, P. C.; Scholes, G. D. Photosynthetic Light Harvesting: Excitons and Coherence. *J. R. Soc. Interface* **2014**, *11* (92), 20130901.
11. Grimm, B. *Chlorophylls and bacteriochlorophylls biochemistry, biophysics, functions and applications*; Springer: Dordrecht, **2006**; pp 5–6.
12. Klumpp, T.; Linsenmann, M.; Larson, S. L.; Limoges, B. R.; Bürssner, D.; Krissinel, E. B.; Elliott, C. M.; Steiner, U. E. Spin Chemical Control of Photoinduced Electron-Transfer Processes in Ruthenium(II)-Trisbipyridine-Based Supramolecular Triads. *J. Am.n Chem. Soc.* **1999**, *121* (5), 1076–1087.
13. Yu, Z.; Li, F.; Sun, L. Recent Advances in Dye-Sensitized Photoelectrochemical Cells for Solar Hydrogen Production Based on Molecular Components. *Energy Environ. Sci.* **2015**, *8* (3), 760–775.
14. Young, K. J.; Martini, L. A.; Milot, R. L.; Snoeberger, R. C.; Batista, V. S.; Schmuttenmaer, C. A.; Crabtree, R. H.; Brudvig, G. W. Light-Driven Water Oxidation for Solar Fuels. *Coord. Chem. Rev.* **2012**, *256* (21–22), 2503–2520.
15. Zhang, S.; Ye, H.; Hua, J.; Tian, H. Recent Advances in Dye-Sensitized Photoelectrochemical Cells for Water Splitting. *Energy Chem* **2019**, *1* (3), 100015.
16. Banerjee, A.; Yuhas, B. D.; Margulies, E. A.; Zhang, Y.; Shim, Y.; Wasielewski, M. R.; Kanatzidis, M. G. Photochemical Nitrogen Conversion to Ammonia in Ambient Conditions with FeMoS-Chalcogels. *J. Am. Chem. Soc.* **2015**, *137* (5), 2030–2034.
17. Berardi, S.; Drouet, S.; Francàs, L.; Gimbert-Suriñach, C.; Guttentag, M.; Richmond, C.; Stoll, T.; Llobet, A. Molecular Artificial Photosynthesis. *Chem. Soc. Rev.* **2014**, *43* (22), 7501–7519.

18. Dupuis, A.-C. Proton Exchange Membranes for Fuel Cells Operated at Medium Temperatures: Materials and Experimental Techniques. *Prog. Mater. Sci.* **2011**, *56* (3), 289–327.
19. Yang, Z.; Gao, S.; Li, W.; Vlasko-Vlasov, V.; Welp, U.; Kwok, W.-K.; Xu, T. Three-Dimensional Photonic Crystal Fluorinated Tin Oxide (FTO) Electrodes: Synthesis and Optical and Electrical Properties. *ACS Appl. Mater. Interfaces* **2011**, *3* (4), 1101–1108.
20. Miessler, G. L.; Fischer, P. J.; Tarr, D. A. *Inorg. Chem*; Pearson: Boston, **2022**; pp 230–233.
21. Sherman, B. D.; Bergkamp, J. J.; Brown, C. L.; Moore, A. L.; Gust, D.; Moore, T. A. A Tandem Dye-Sensitized Photoelectrochemical Cell for Light Driven Hydrogen Production. *Energy Environ. Sic.* **2016**, *9* (5), 1812–1817.
22. Smestad, G. P.; Steinfeld, A. Review: Photochemical and Thermochemical Production of Solar Fuels from H_2O and CO_2 Using Metal Oxide Catalysts. *Ind. Eng. Chem. Res.* **2012**, *51* (37), 11828–11840.
23. Hagfeldt, A.; Boschloo, G.; Sun, L.; Kloo, L.; Pettersson, H. Dye-Sensitized Solar Cells. *Chem. Rev.* **2010**, *110* (11), 6595–6663.
24. Reynal, A.; Palomares, E. Ruthenium Polypyridyl Sensitisers in Dye Solar Cells Based on Mesoporous TiO_2. *Eur. J. Inor. Chem.* **2011**, *2011* (29), 4509–4526.
25. Mishra, A.; Fischer, M. K. R.; Bäuerle, P. Metal-Free Organic Dyes for Dye-Sensitized Solar Cells: From Structure: Property Relationships to Design Rules. *Angew. Chem. Int. Ed.* **2009**, *48* (14), 2474–2499.
26. Housecroft, C. E.; Constable, E. C. The Emergence of Copper(I)-Based Dye Sensitized Solar Cells. *Chem. Soc. Rev.* **2015**, *44* (23), 8386–8398.
27. Fujishima, A.; Honda, K. Electrochemical Photolysis of Water at a Semiconductor Electrode. *Nature* **1972**, *238*(5358), 37–38.
28. Eckenhoff, W. T.; Eisenberg, R. Molecular Systems for Light Driven Hydrogen Production. *Dalton Trans.* **2012**, *41*(42), 13004.
29. Singh, Z.; Donnarumma, P. R. and Majewski, M. Molecular Copper(I)-Copper(II) Photosensitizer-Catalyst Photoelectrode for Water Oxidation. *Inorg. Chem.* **2020**, 59, 12994-12999.
30. Miyoshi, D.; Karimata, H.; Wang, Z.-M.; Koumoto, K.; Sugimoto, N. Artificial G-Wire Switch with 2,2‘-Bipyridine Units Responsive to Divalent Metal Ions. *J. Am. Chem. Soc.* **2007**, *129* (18), 5919–5925.
31. Barolo, C.; Nazeeruddin, Md. K.; Fantacci, S.; Di Censo, D.; Comte, P.; Liska, P.; Viscardi, G.; Quagliotto, P.; De Angelis, F.; Ito, S.; Grätzel, M. Synthesis, Characterization, and DFT-TDDFT Computational Study of a Ruthenium Complex Containing a Functionalized Tetradentate Ligand. *Inorg. Chem.* **2006**, *45* (12), 4642–4653.
32. Kanno, H.; Yamamoto, J.; Murahashi,S.; Utsuno. S and Fujita. J. Isomerization and Racemization of the Tris(4,4’-dimethyl-2,2’-bipyridine N, N’-dioxide)chromium(III) Complex. *Bull. Chem. Soc. Jpn.* **1991**, 64 (10) 2936-2941.
32. Cadge, J. A.; Bower, J. F.; and Ruseell, C. A. *Ang. Chem. Inter. Ed*, **2021**, 60, 47, 24976-24983.

33. Sandroni, M.; Favereau, L.; Planchat, A.; Akdas-Kilig, H.; Szuwarski, N.; Pellegrin, Y.; Blart, E.; Le Bozec, H.; Boujtita, M.; Odobel, F. Heteroleptic Copper(I)–Polypyridine Complexes as Efficient Sensitizers for Dye Sensitized Solar Cells. *J. Mater. Chem. A* **2014**, *2* (26), 9944–9947.
34. Sandroni, M.; Pellegrin, Y.; Odobel, F. Heteroleptic Bis-Diimine Copper(I) Complexes for Applications in Solar Energy Conversion. *Comptes. Rendus. Chimie.* **2016**, *19* (1–2), 79–93.
35. Schmittel, M.; Ganz, A. Stable mixed phenanthroline copper(i) complexes. Key building blocks for supramolecular coordination chemistry. *Chem. Commun*. **1997**, 11, 999.
36. Bartelmess, J.; Francis, A. J.; El Roz, K. A.; Castellano, F. N.; Weare, W. W.; Sommer, R. D. Light-Driven Hydrogen Evolution by BODIPY-Sensitized Cobaloxime Catalysts. *Inorg. Chem.* **2014**, *53* (9), 4527–4534.
37. Meher, S. K.; Justin, P.; Ranga Rao, G. Microwave-Mediated Synthesis for Improved Morphology and Pseudocapacitance Performance of Nickel Oxide. *ACS Appl. Mater. Interfaces* **2011**, *3* (6), 2063–2073.
38. Toscano, P. J.; Swider, T. F.; Marzilli, L. G.; Bresciani-Pahor, N.; Randaccio, L. Organocobalt B12 Models. an Assessment of the CIS Effect Using Bis(Glyoximato) as a Sterically Minimal Equatorial Atom Set. Structures of Trans-Bis(Glyoximato)Methyl(l)Cobalt(Iii) with L = Triphenylphosphine and Trimethyl Phosphite. *Inorg. Chem.* **1983**, *22* (23), 3416–3421.
39. Kamire, R. J.; Majewski, M. B.; Hoffeditz, W. L.; Phelan, B. T.; Farha, O. K.; Hupp, J. T. and Wasielewski, M. R. Photodriven hydrogen evolution by molecular catalysts using Al2O3-protected perylene-3,4-dicarboximide on NIO electrodes. *Chemi. Sci.* **2017**, *8*, 541–549.
40. Elgrishi, N.; Rountree, K. J.; McCarthy, B. D.; Rountree, E. S.; Eisenhart, T. T.; Dempsey, J. L. A Practical Beginner's Guide to Cyclic Voltammetry. *J. Chem. Educ.* **2018**, *95* (2), 197–206.
41. Jennings, W.; Mittlefehldt, E.; Stremple, P. Analytical Gas Chromatography, *Elsevier Science*. **1997**.
42. Dang Quang, L. N.; Kaliamurthy, A. K.; Hao, N. H. Co-Sensitization of Metal Based N719 and Metal Free D35 Dyes: An Effective Strategy to Improve the Performance of DSSC. *Optical Mater.* **2021**, *111*, 110589.
43. Wang, J.; Zhao, Z.; Zhou, S.; Zhang, X.; Bo, H. The Antitumor Effect and Toxicity of a Ruthenium(II) Complex in Vivo. *Inorganic Chemistry Communications* **2018**, *87*, 49–52.
44. Wenger, O. S. Is Iron the New Ruthenium? *Chem. Eur. J.* **2019**, *25* (24), 6043–6052.
45. Kalyanasundaram, K. Photophysics, photochemistry and solar energy conversion with tris(bipyridyl)ruthenium(II) and its analogues. *Coord. Chem. Rev*. **1982**, *46*, 259-244.
46. Rosko, M. C.; Wells, K. A.; Hauke, C. E.; Castellano, F. N. Next Generation Cuprous Phenanthroline MLCT Photosensitizer Featuring Cyclohexyl Substituents. *Inorg. Chem.* **2021**, *60* (12), 8394–8403.
47. Lazorski, M. S.; Gest, R. H.; Elliott, C. M. Photoinduced Multistep Charge Separation in a Heteroleptic Cu(I) Bis(Phenanthroline)-Based Donor–Chromophore–Acceptor Triad. *J. Am. Chem. Soc.* **2012**, *134* (42), 17466–17469.

48. Nguyen, P. T.; Lam, B. X. T.; Andersen, A. R.; Hansen, P. E.; Lund, T. Photovoltaic Performance and Characteristics of Dye-Sensitized Solar Cells Prepared with the N719 Thermal Degradation Products [Ru(LH)$_2$(NCS)(4-*Tert*-butylpyridine)][N(Bu)$_4$] and [Ru(LH)$_2$(NCS)(1-methylbenzimidazole)][N(Bu)$_4$]. *Eur. J. Inorg. Chem.* **2011**, *2011* (16), 2533–2539.
49. Khnayzer, R. S.; McCusker, C. E.; Olaiya, B. S.; Castellano, F. N. Robust Cuprous Phenanthroline Sensitizer for Solar Hydrogen Photocatalysis. *J. Am. Chem. Soc.* **2013**, *135* (38), 14068–14070.
50. Pavia, D. L.; Lampman, G. M.; Kriz, G. S.; Vyvyan, J. A. *Introduction to spectroscopy*; Cengage Learning, **2015**.
51. Chowdhury, D. R.; Spiccia, L.; Amritphale, S. S.; Paul, A.; Singh, A. A Robust Iron Oxyhydroxide Water Oxidation Catalyst Operating under near Neutral and Alkaline Conditions. *J. Mater. Chem. A* **2016**, *4* (10), 3655–3660.
52. Schwarzhans, K. E. NMR Spectroscopy of Paramagnetic Complexes. *Angew. Chem. Int. Ed. Engl.* **1970**, *9* (12), 946–953.
53. Medek, A.; Frydman, V.; Frydman, L. Solid and Liquid Phase ^{59}Co NMR Studies of Cobalamins and Their Derivatives. *Proc. Natl. Acad. Sci. U.S.A.* **1997**, *94* (26), 14237–14242.
54. Ukoba, K. O.; Eloka-Eboka, A. C.; Inambao, F. L. Review of Nanostructured NiO Thin Film Deposition Using the Spray Pyrolysis Technique. *Renew. and Sust. Energy Rev.* **2018**, *82*, 2900–2915.
55. Ismail, R. A.; Ghafori, S.; Kadhim, G. A. Preparation and Characterization of Nanostructured Nickel Oxide Thin Films by Spray Pyrolysis. *Appl. Nanosci.* **2013**, *3* (6), 509–514.
56. Pecher, L.; Tonner, R. Precursor States of Organic Adsorbates on Semiconductor Surfaces Are Chemisorbed and Immobile. *Chem. Phys. Chem* **2017**, *18* (1), 34–38.
57. Ko, C.-C.; Kwok, W.-M.; Yam, V. W.-W.; Phillips, D. L. Triplet MLCT Photosensitization of the Ring-Closing Reaction of Diarylethenes by Design and Synthesis of a Photochromic Rhenium(i) Complex of a Diarylethene-Containing 1,10-Phenanthroline Ligand. *Chem. Euro. J.* **2006**, *12* (22), 5840–5848.
58. Wiegmann, B.; Jones, P. G.; Wagenblast, G.; Lennartz, C.; Münster, I.; Metz, S.; Kowalsky, W.; Johannes, H.-H. A New Framework of a Heteroleptic Iridium(Iii)–Carbene Complex as a Triplet Emitting Material. *Organometallics* **2012**, *31* (15), 5223–5226.
59. Franco, F.; Cometto, C.; Garino, C.; Minero, C.; Sordello, F.; Nervi, C.; Gobetto, R. Photo- and Electrocatalytic Reduction of CO$_2$ by [Re(CO)$_3$ {α,A′-Diimine-(4-piperidinyl-1,8-naphthalimide)}Cl] Complexes. *Eur. J. Inorg. Chem.* **2015**, *2015* (2), 296–304.
60. Singh, Z.; Kamal, S.; Majewski, M. B. Copper(I) Donor–Chromophore–Acceptor Assembly for Light-Driven Oxidation on a Zinc Oxide Nanowire Electrode. *J. Phys. Chem. C* **2022**, *126* (39), 16732–16743.
61. Torres, T.; Gouloumis, A.; Sanchez-Garcia, D.; Jayawickramarajah, J.; Seitz, W.; Guldi, D. M.; Sessler, J. L. Photophysical Characterization of a Cytidine–Guanosine Tethered Phthalocyanine–Fullerene Dyad. *Chem. Commun.* **2007**, No. 3, 292–294.

62. Pavlishchuk, V. V.; Addison, A. W. Conversion Constants for Redox Potentials Measured versus Different Reference Electrodes in Acetonitrile Solutions at 25°C. *Inorg. Chim Acta* **2000**, *298* (1), 97–102.

Appendix

1. NMR Spectra

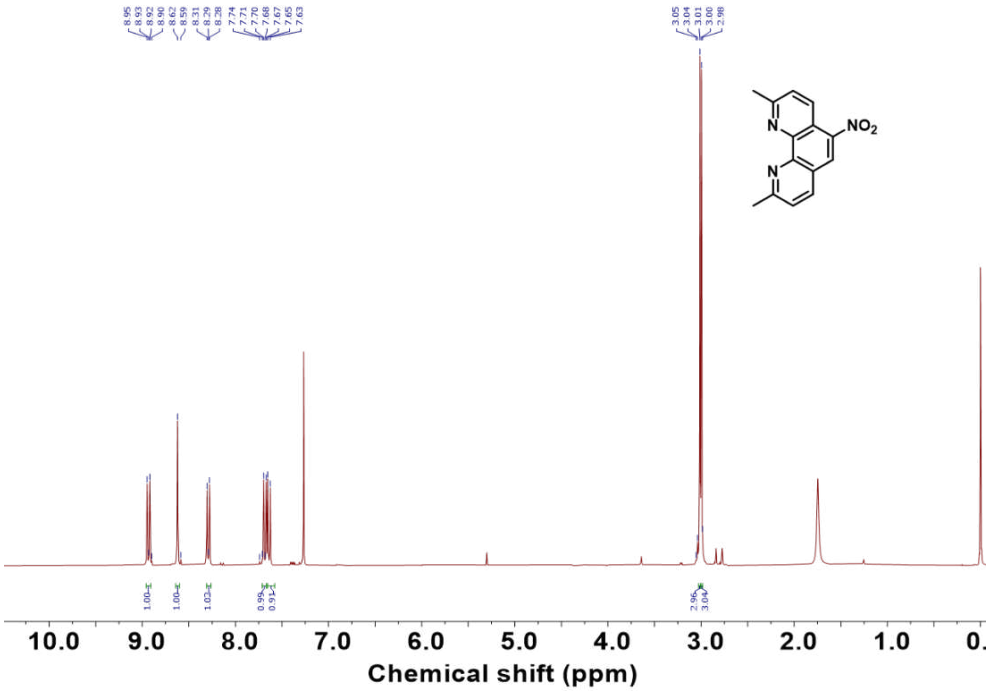

Figure A1. ^{1}H spectrum of **23** in $CDCl_3$ (300 MHz)

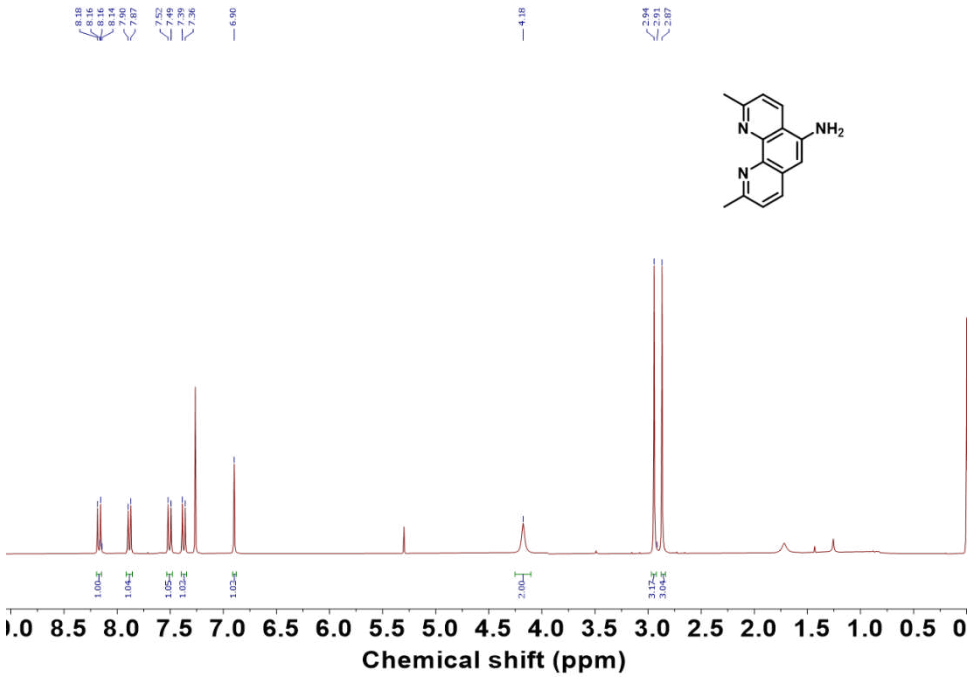

Figure A2. ^{1}H spectrum of **24** in $CDCl_3$ (300 MHz)

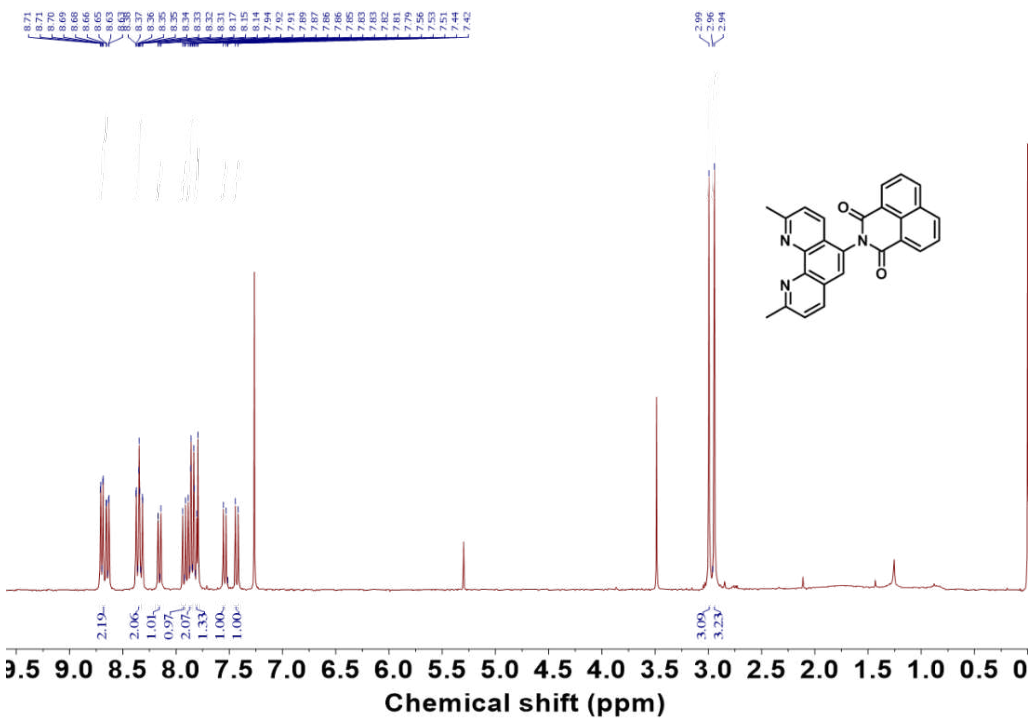

Figure A3. ^{1}H spectrum of **A** in $CDCl_3$ (300 MHz)

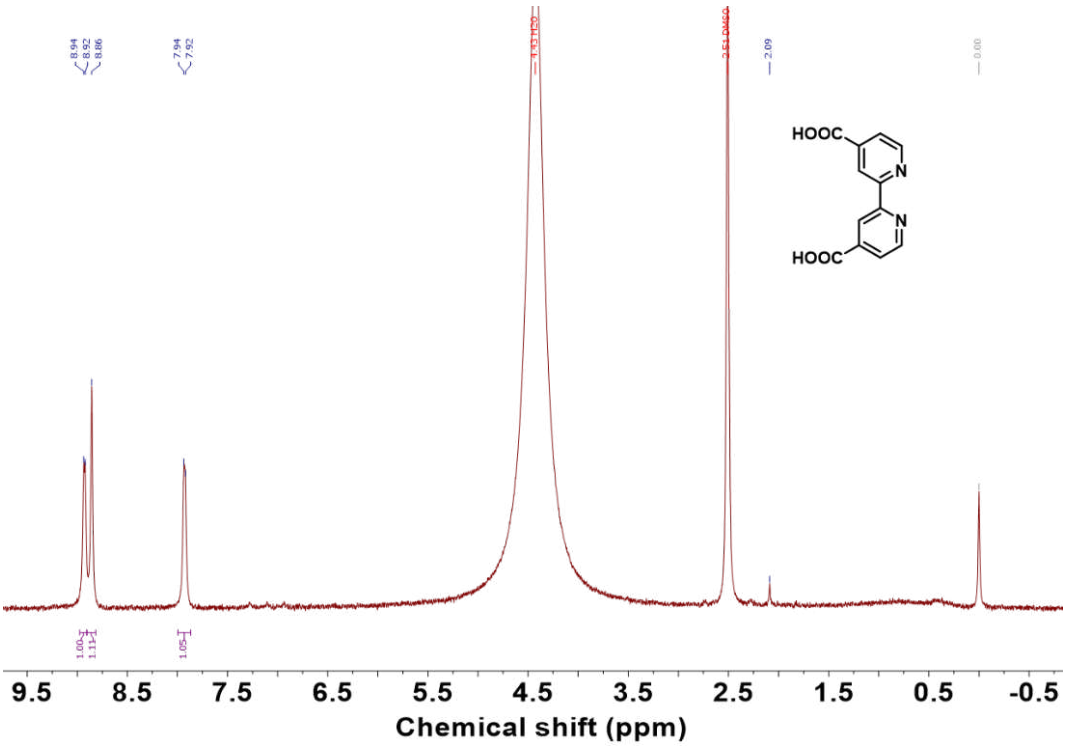

Figure A4. ^{1}H spectrum of **27** in DMSO-d_6 (300 MHz)

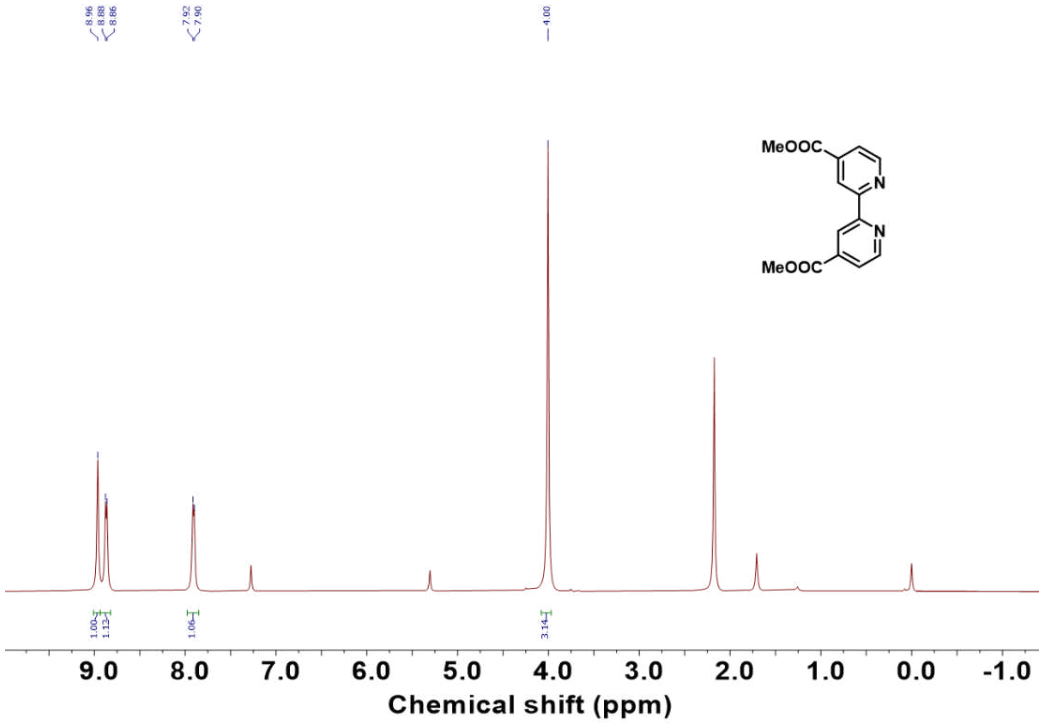

Figure A5. ^{1}H NMR spectrum of **An1** in DMSO-d_6 (300 MHz)

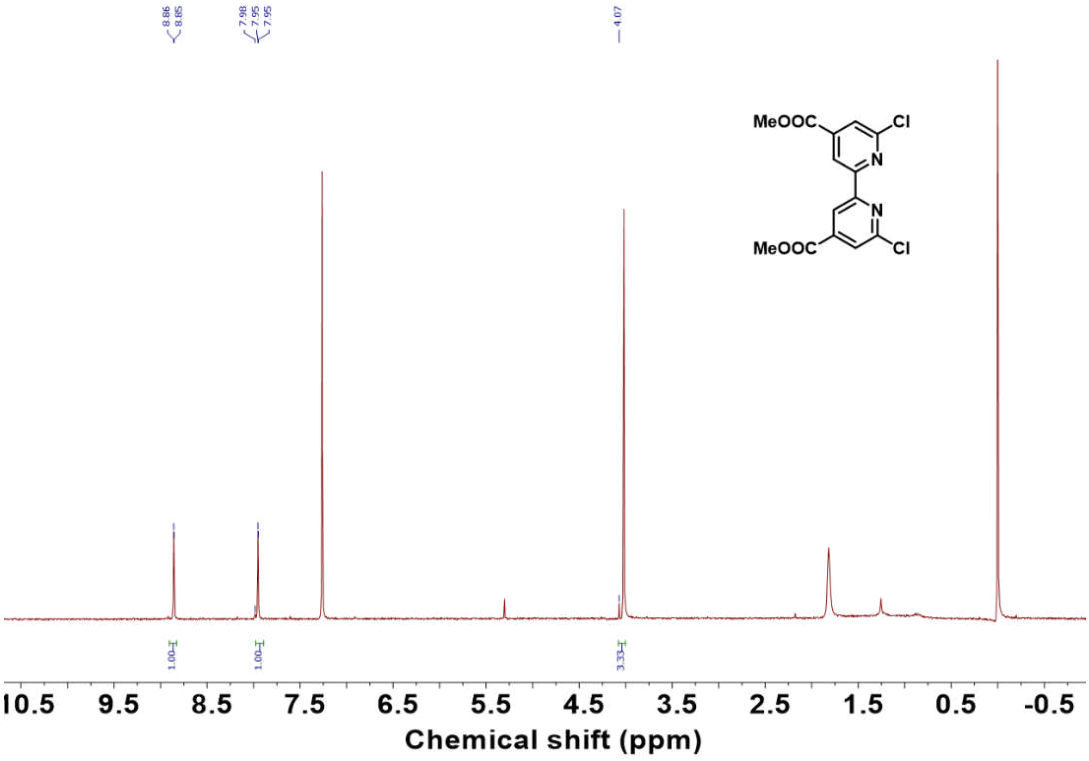

Figure A6. ^{1}H spectrum of **29** in $CDCl_3$ (300 MHz)

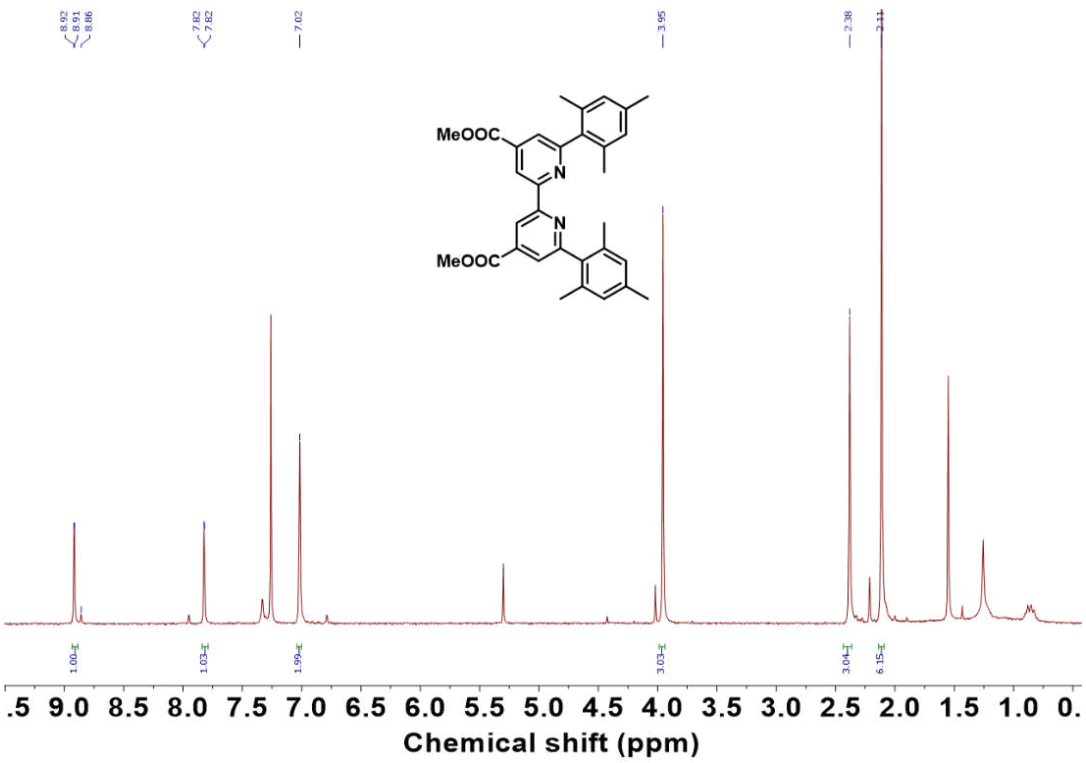

Figure A7. ^{1}H spectrum of **30** in $CDCl_3$ (300 MHz)

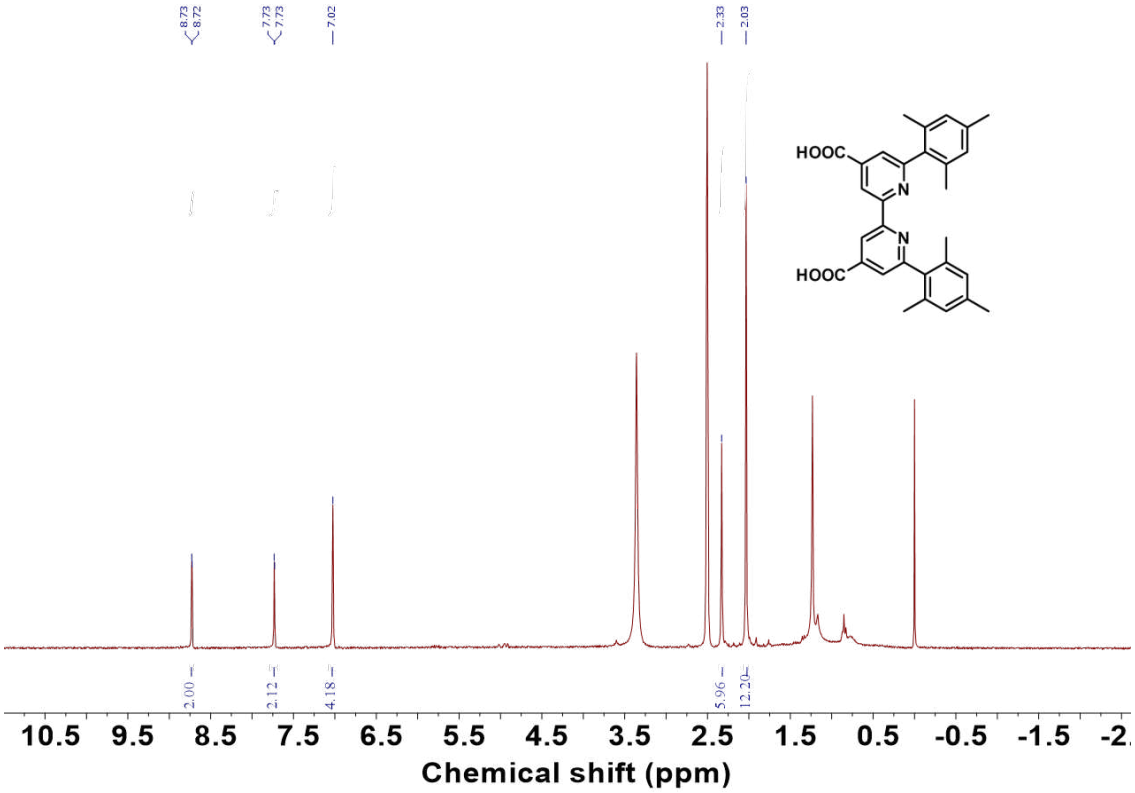

Figure A8. ^{1}H NMR spectrum of **An2** in DMSO-d_6

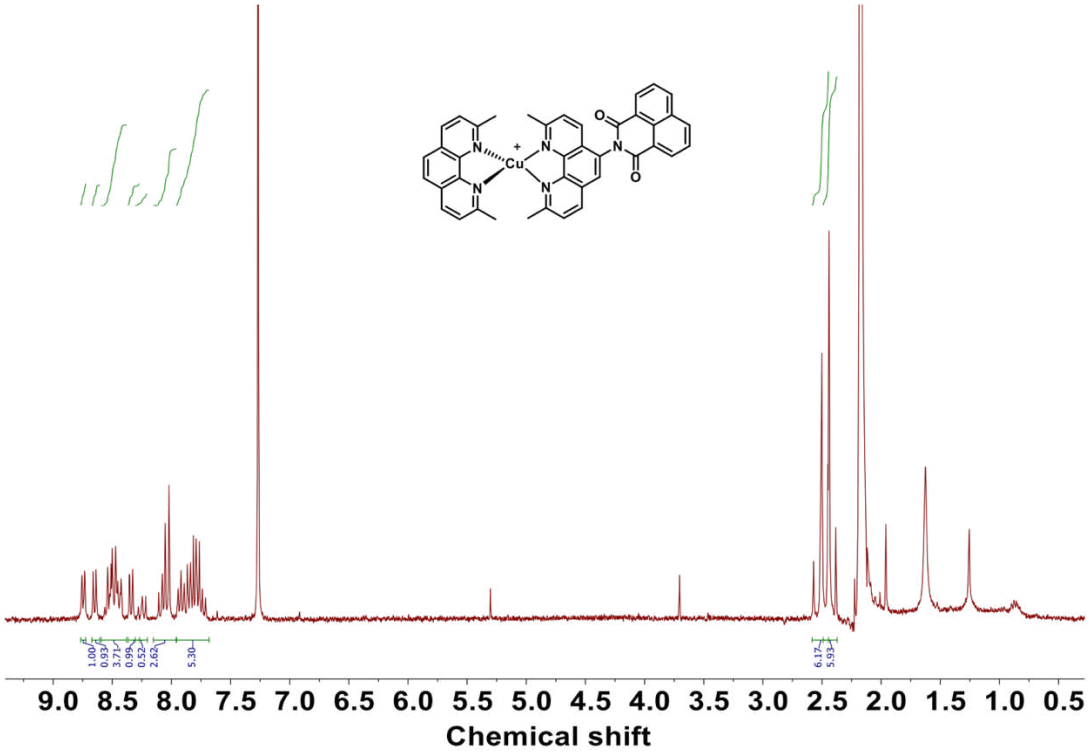

Figure A9. ^{1}H spectrum of **A-Cu-dmp** in $CDCl_3$ (300 MHz)

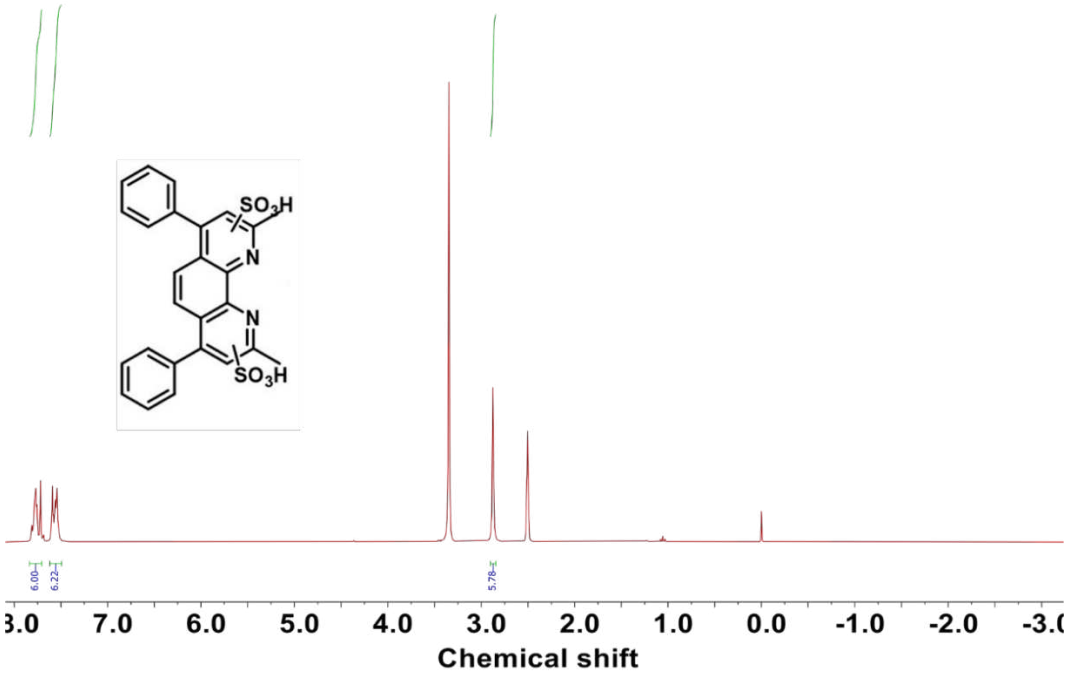

Figure A10. ^{1}H NMR spectrum of **bathocuproine disulfonic** in DMSO-d_6 (300 MHz)

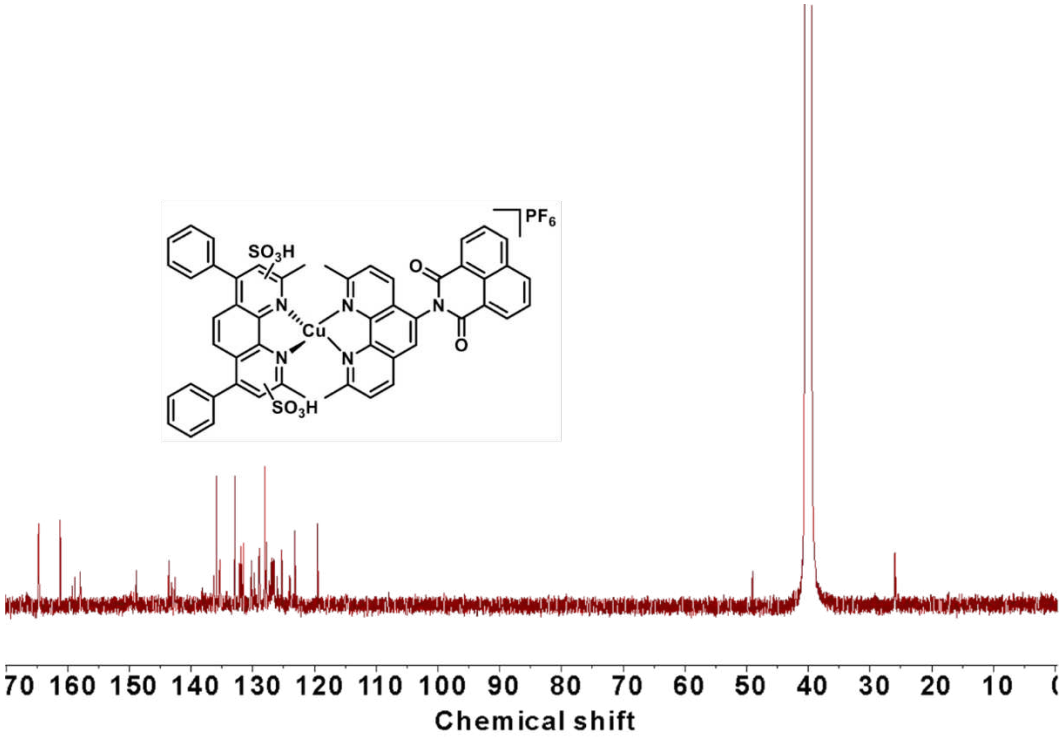

Figure A11. ^{13}C NMR spectrum of **WEI3** in DMSO-d_6 (500 MHz)

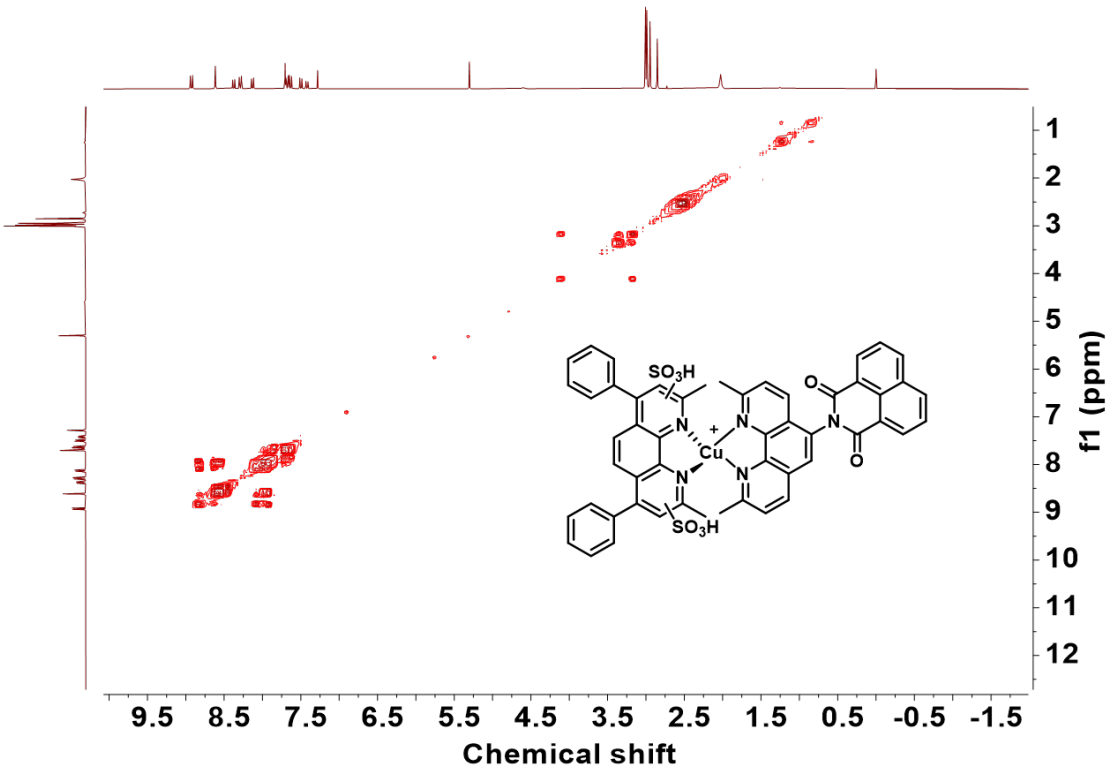

Figure A12. 2D ^{1}H NMR (COSY) spectrum of **WEI3** in DMSO-d_6 (500 MHz)

2. Mass spectroscopies

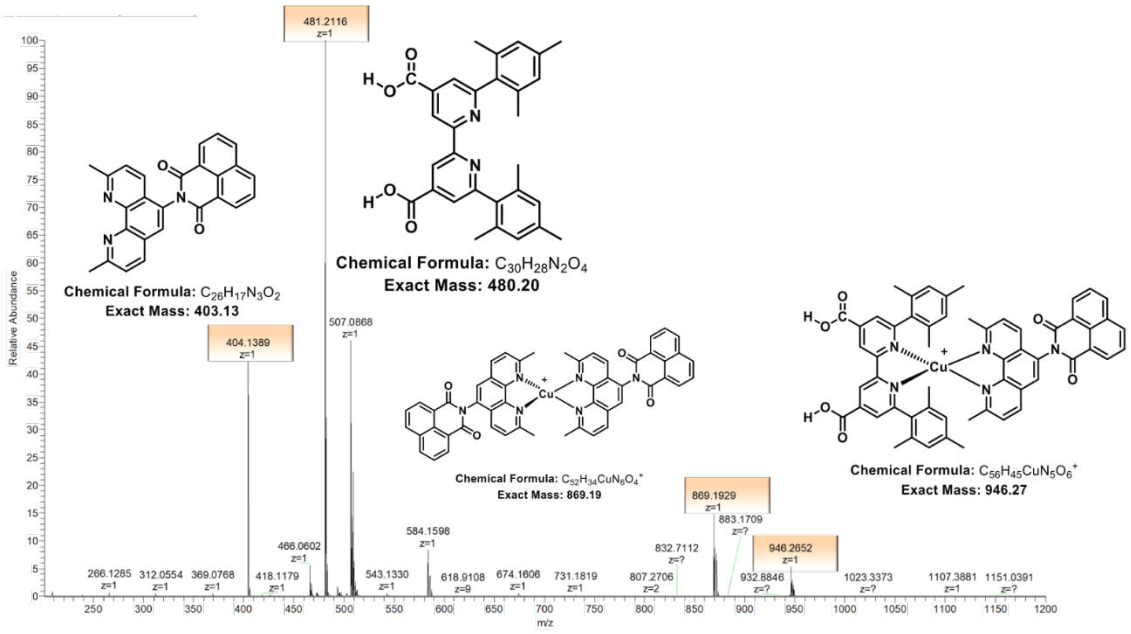

Figure A13. Mass spectrometry of **WEI2**

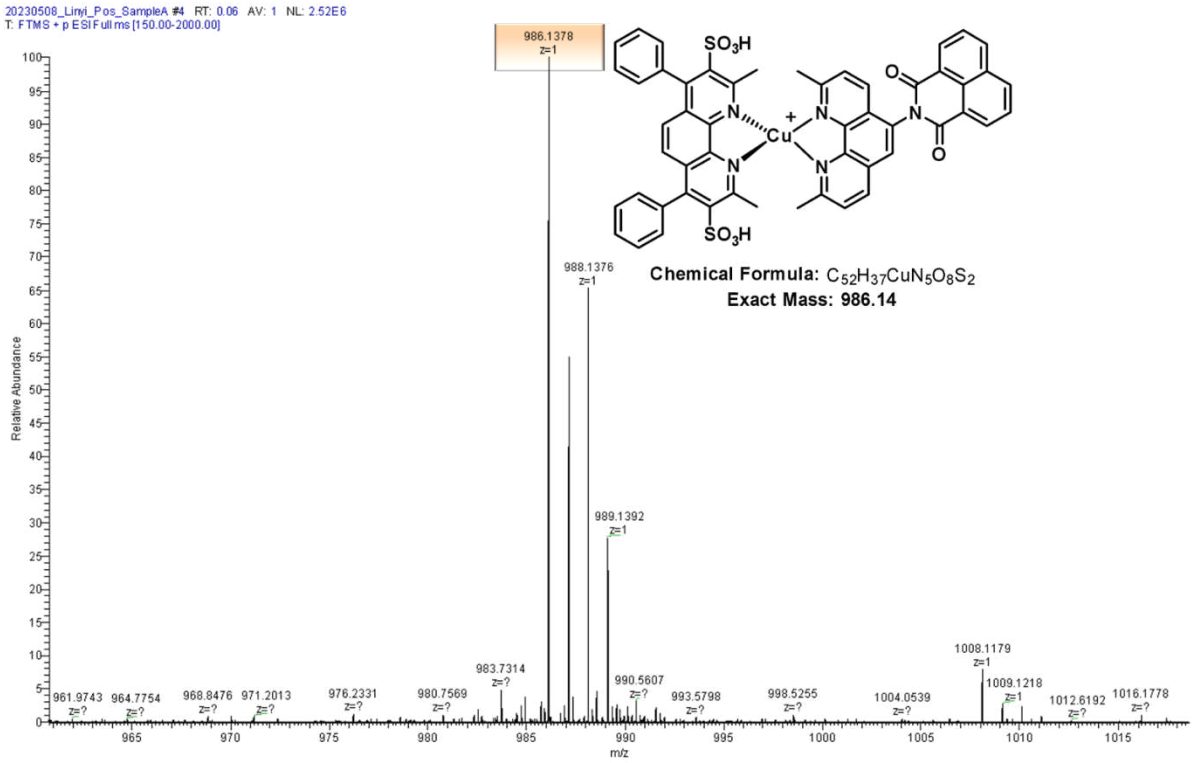

Figure A14. Mass spectrometry of **WEI3**

3. Gas chromatography documents

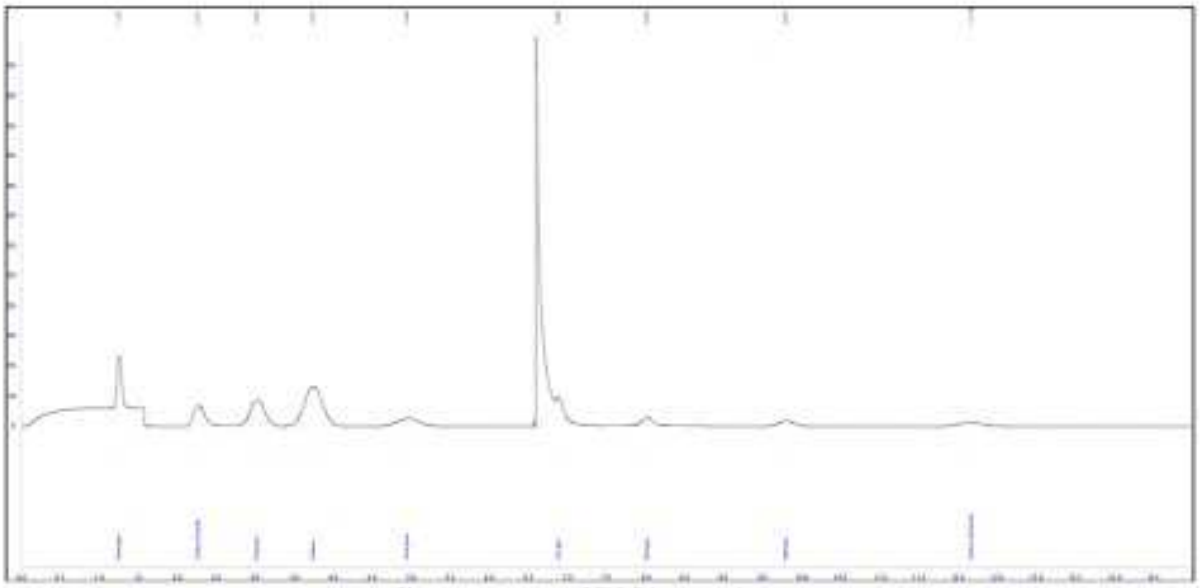

Figure A15. Test chromatograms for calibration gas

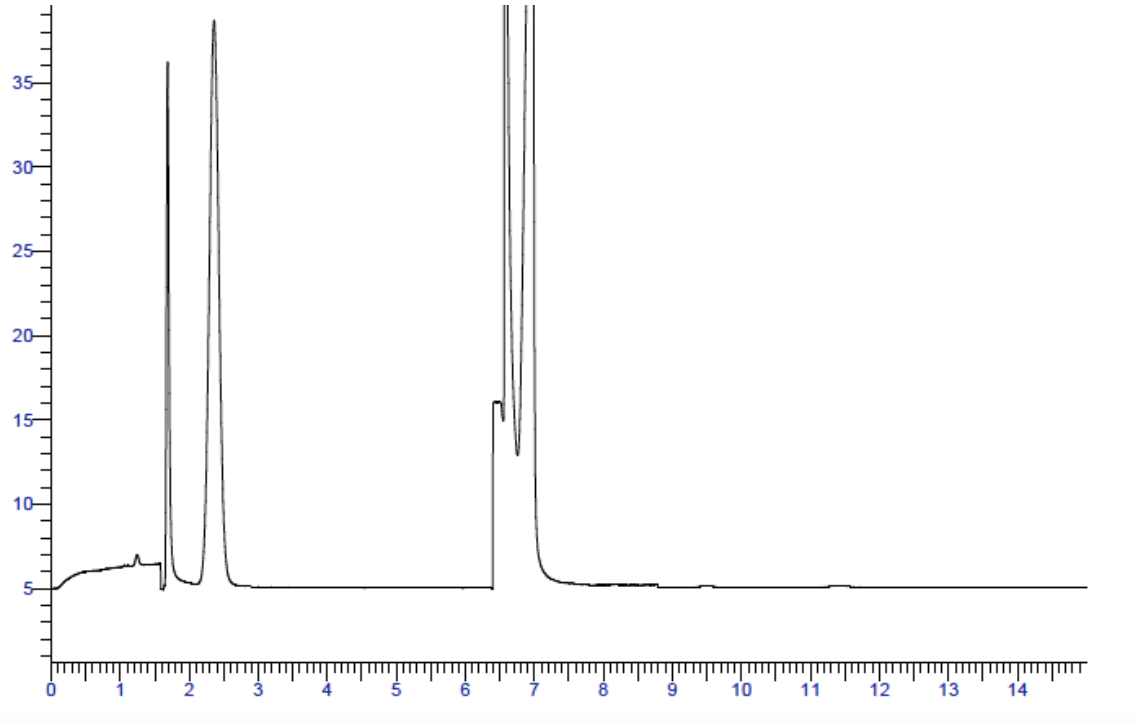

Figure A16. GC chromatogram of zero measurement of **WEI2** (X-axis: time/s, Y-axis: voltage/mV)

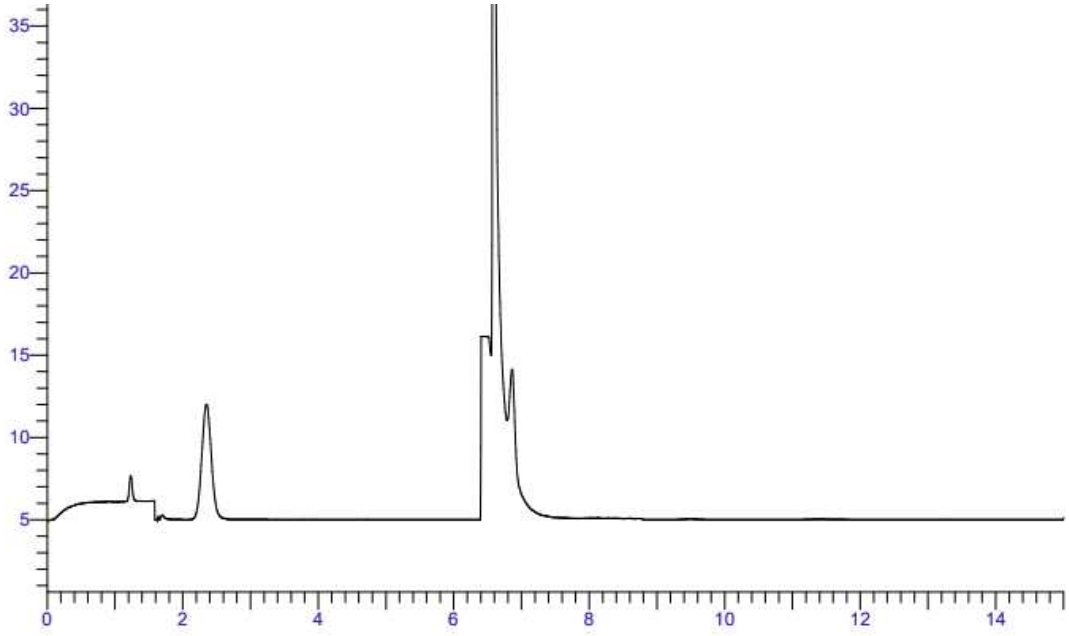

Figure A17. GC chromatogram of zero measurement of **WEI3** with TEA (X-axis: time/s, Y-axis: voltage/mV)

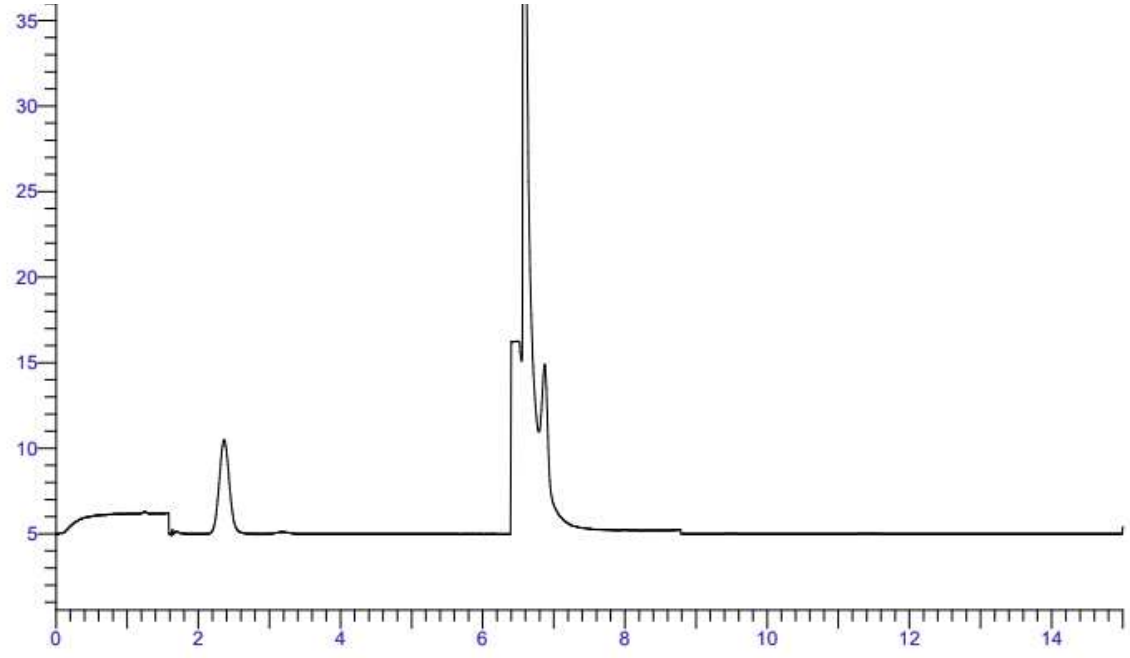

Figure A18. GC chromatogram of zero measurement of **WEI3** without TEA (X-axis: time/s, Y-axis: voltage/mV)

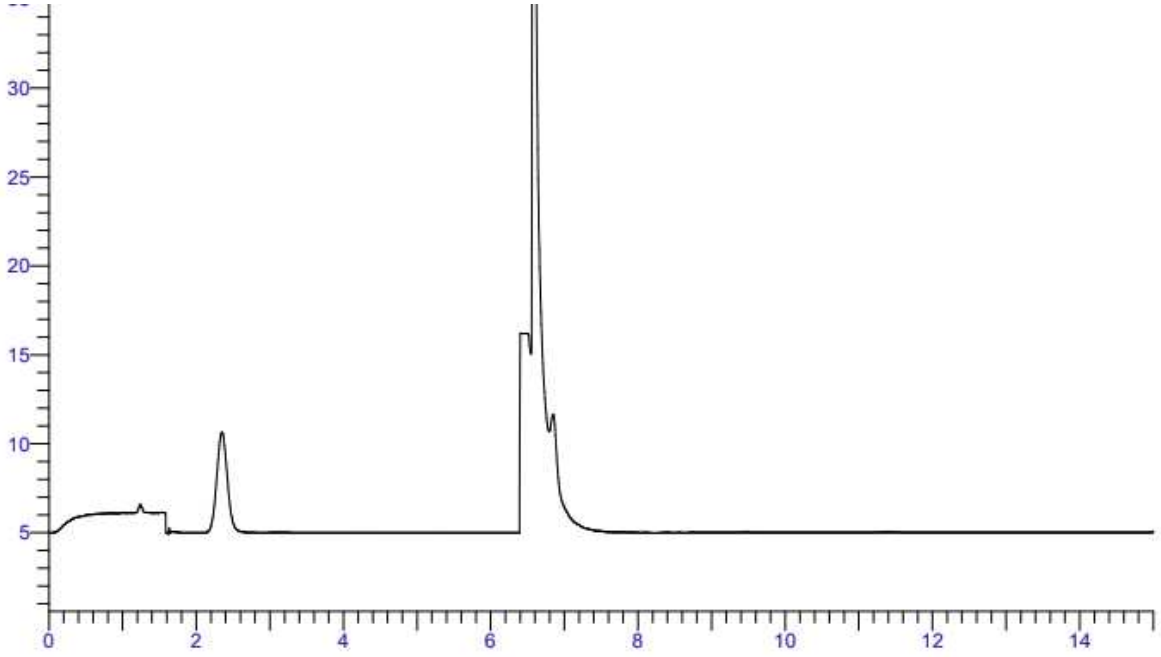

Figure A19. GC chromatogram of zero measurement of **WEI3** after 1 hour photoirradiation without TEA (X-axis: time/s, Y-axis: voltage/mV)

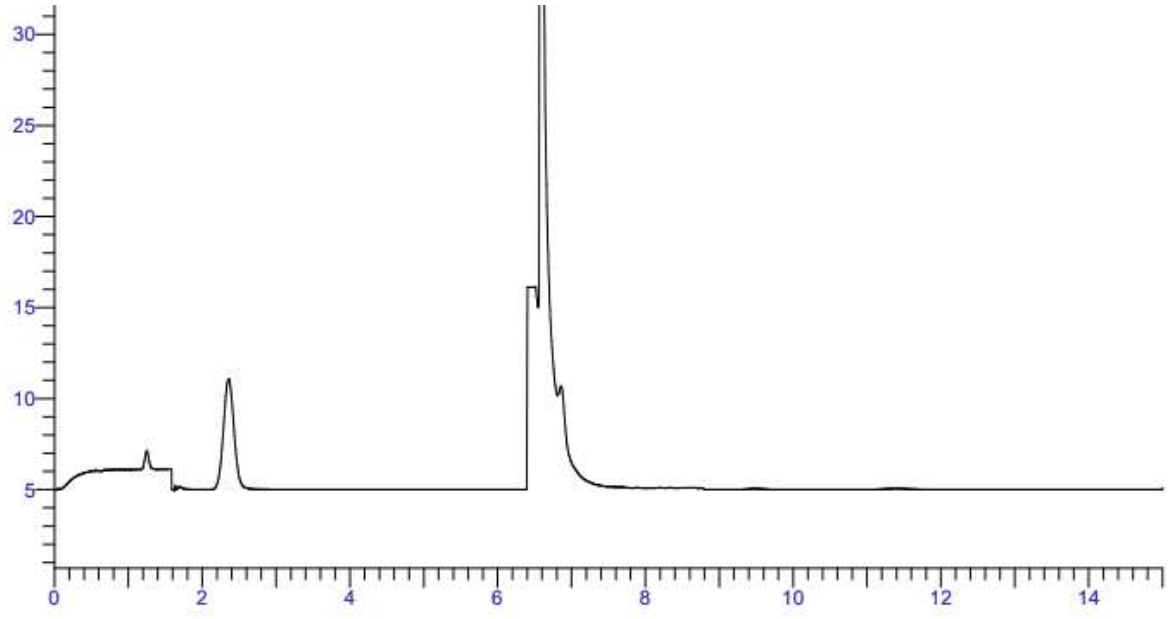

Figure A20. GC chromatogram of zero measurement of **WEI2** after 2 hours photoirradiation (X-axis: time/s, Y-axis: voltage/mV)

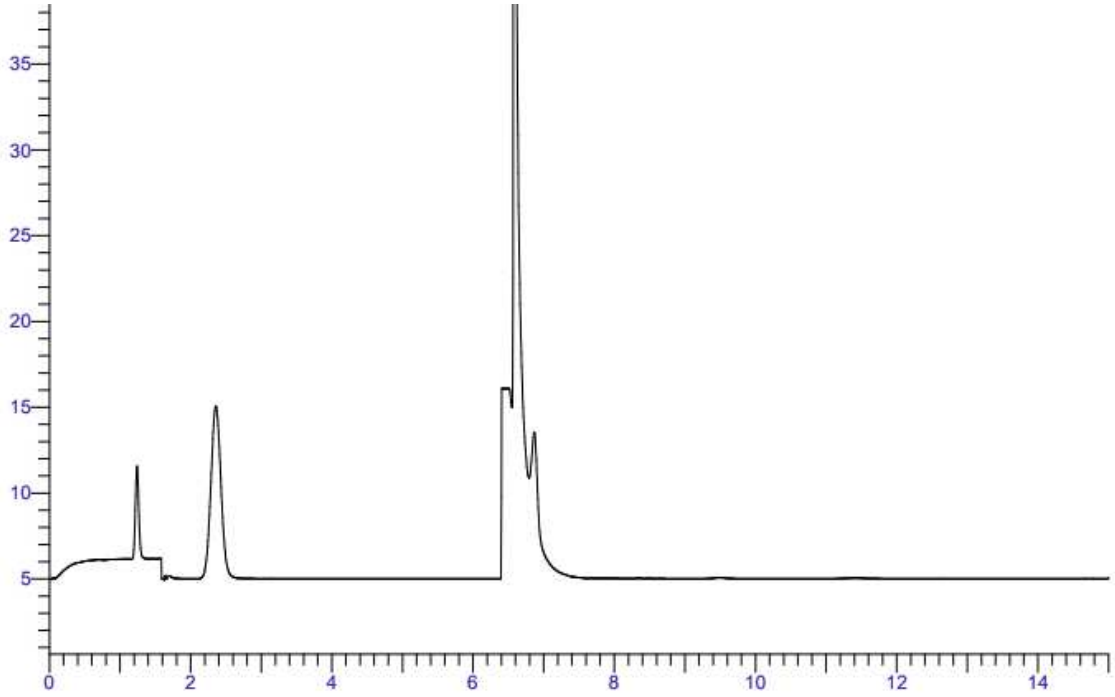

Figure A21. GC chromatogram of zero measurement of **WEI3** after 2 hours photoirradiation with TEA (X-axis: time/s, Y-axis: voltage/mV)

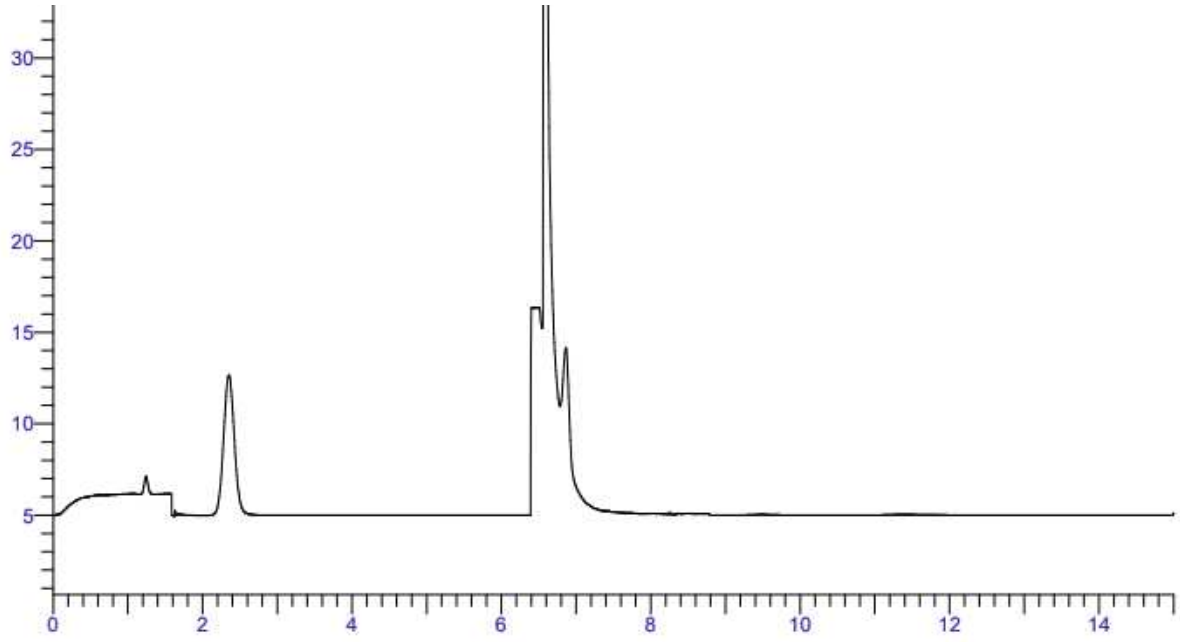

Figure A22. GC chromatogram of zero measurement of **WEI3** after 2 hours photoirradiation without TEA (X-axis: time/s,Y-axis: voltage/mV)

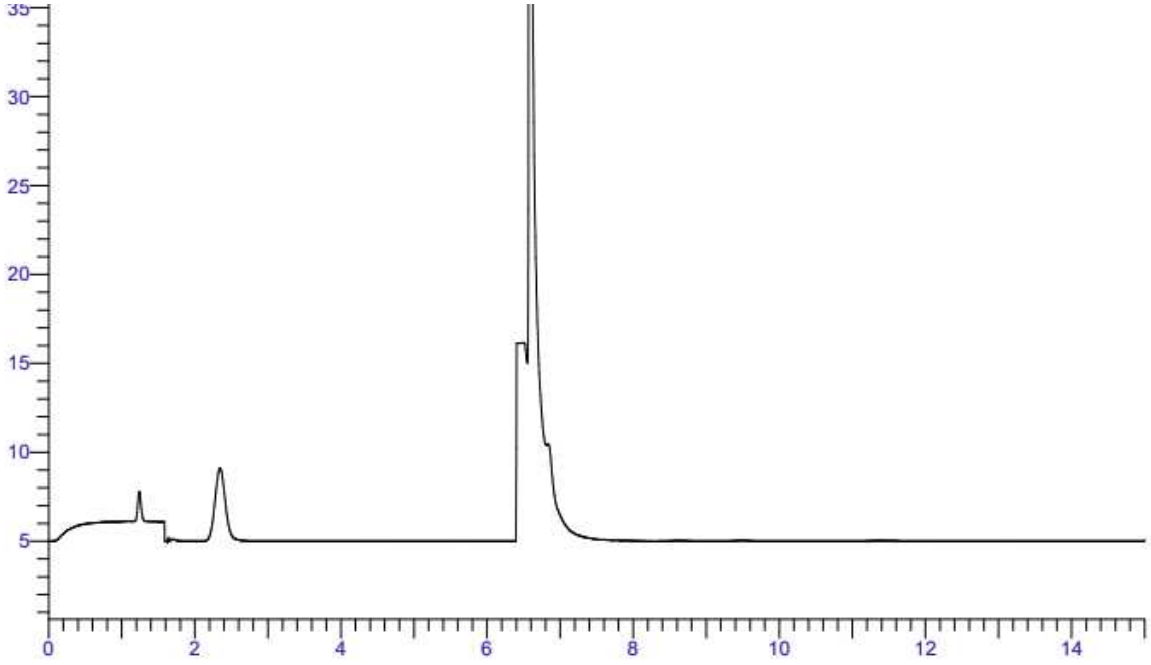

Figure A23. GC chromatogram of zero measurement of **WEI2** after 3 hours photoirradiation (X-axis: time/s, Y-axis: voltage/mV)

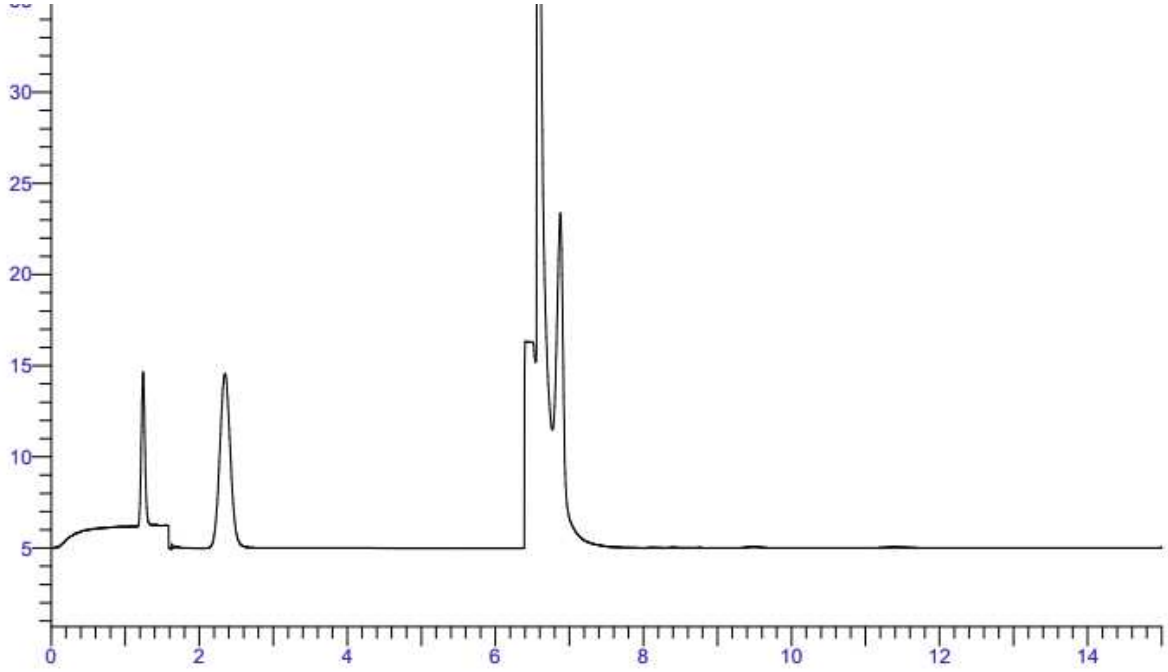

Figure A24. GC chromatogram of zero measurement of **WEI3** after 3 hours photoirradiation with TEA (X-axis: time/s, Y-axis: voltage/mV)

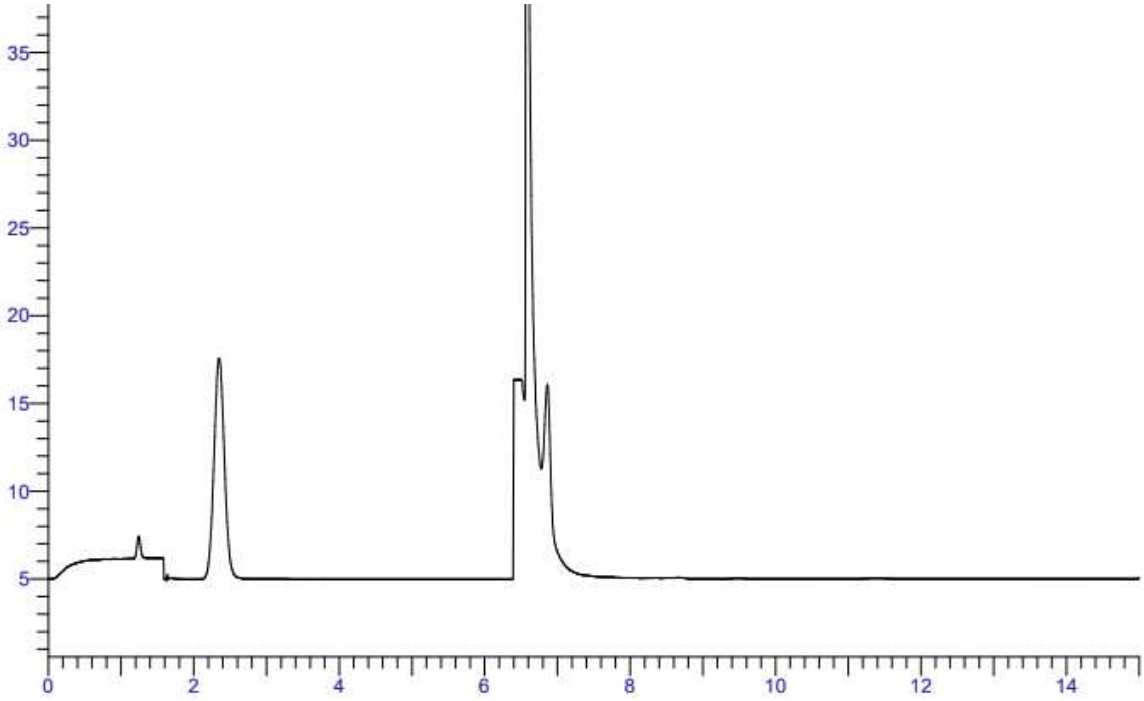

Figure A25. GC chromatogram of zero measurement of **WEI3** after 3 hours photoirradiation without TEA (X-axis: time/s, Y-axis: voltage/mV)

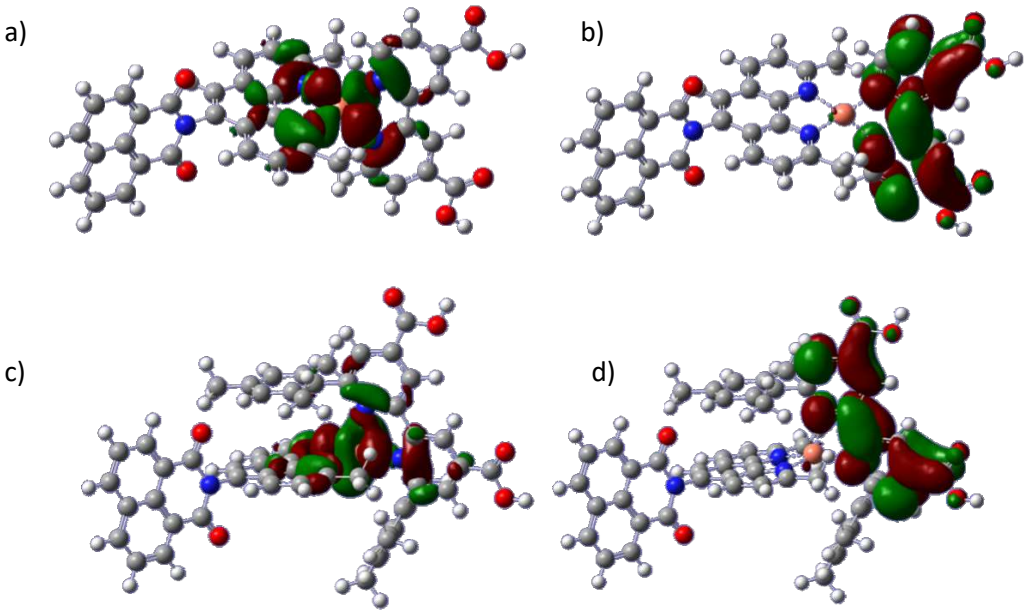

Figure A26. Graphical representations of a) HOMO and b) LUMO of **WEI1**, and c) HOMO and d) LUMO of **WEI2**.